A NUMERICAL STUDY OF INTERFACIAL INSTABILITIES IN SHOCKED
MATERIALS WITH SURFACE TENSION

by

Pedram Bigdelou

A dissertation submitted to the faculty of
The University of North Carolina at Charlotte
in partial fulfillment of the requirements
for the degree of Doctor of Philosophy in
Mechanical Engineering

Charlotte

2020

Approved by:

_____
Dr. Praveen Ramaprabhu

_____
Dr. Harish Cherukuri

_____
Dr. Shaozhong Deng

_____
Dr. Yuri Godin

ABSTRACT

PEDRAM BIGDELOU. A Numerical Study of Interfacial Instabilities in Shocked Materials with Surface Tension. (Under the direction of DR. PRAVEEN RAMAPRABHU)

Shock-driven multi-material flows occur in several applications including shock wave lithotripsy, underwater explosions, droplet combustion, propeller cavitation and ejection of material from surfaces subject to blast loading. Such flows are highly compressible due to the presence of strong shocks, yet are influenced to a significant extent by surface tension forces at the interface separating two or more materials. In particular, surface tension can impact the evolution of the interface, by stabilizing hydrodynamic instabilities occurring at the interface. The presence of surface tension can also influence aspects of the late-time interface breakup process, and determine the size distribution, transport, subsequent breakup and phase change of droplets. The modeling of such flows requires the development and application of specialized numerical methods, capable of handling the multi-physics nature of the flow dynamics. In this work, we report on the development and validation of novel numerical methods for shock-driven multi-material flows with surface tension. The numerical methods have been implemented in IMPACT, a Computational Fluid Dynamics software, with a wide array of physics capabilities including compressible flows with multiple equations of state, surface tension, and phase change.

IMPACT solves the Euler equations using a finite volume approach, and exploits the Roe Riemann solver to obtain intecell fluxes. A fifth-order WENO reconstruction for spatial discretization is coupled with a third-order TVD Runge-Kutta scheme for time

discretization. The Level Set method is implemented in IMPACT to track the interface between materials and to obtain interface curvature required for surface tension calculations. Interfacial boundary conditions are applied to the cells bordering the material interface using the Ghost Fluid Method (GFM). In the presence of surface tension, the GFM is modified to account for the pressure jump across the curved interface stemming from surface tension effects. The GFM and its variants have been used extensively in the numerical treatment of shocked, multi-material flows, but are susceptible to overheating errors near the interface as well as spurious numerical reflections. To address these issues, we have developed a novel, highly accurate variation of the GFM called the Efficient GFM (EGFM) which removes overheating errors at the interfaces and numerical reflections, resulting in numerical solutions that are in agreement with analytical solutions. When compared with the original GFM approach and its subsequent variants, the EGFM scheme proposed here is robust, and has been demonstrated in this dissertation to accurately simulate a wide range of Riemann problems and shock-interface problems.

ACKNOWLEDGMENTS

TABLE OF CONTENTS

LIST OF TABLES

LIST OF FIGURES

CHAPTER 1: INTRODUCTION

Shock-driven multi-phase flows are of great significance to various engineering problems, such as chemically reacting flows [1-3] (for example combustion [4-6]), cavitation [7], shock wave therapy and lithotripsy [8, 9], and material ejection [10-12]. In such flows, the evolution of an interface separating disparate materials is central to determining the flow characteristics and ultimately the performance of the engineering system. Often, surface tension is present at the interface and can fundamentally alter the dynamics of the underlying instability evolution. Such flow problems require specialized numerical methods capable of capturing the compressible flow properties with fidelity, while accurately tracking the interface evolution through the complex topological changes. In this dissertation, we describe the development and implementation of numerical methods that address the above objectives.

Depending on the problem at hand, the material interface may be susceptible to hydrodynamic instabilities including the shear-driven Kelvin-Helmholtz instability (KHI), gravity-driven Rayleigh-Taylor instability [13, 14] (RTI), and the shock-driven Richtmyer-Meshkov instability [15, 16] (RMI). Specific to shocked interfaces is the RMI which is triggered when a shock wave traverses the initially corrugated interface between materials of mismatched impedances. Initial perturbations at the interface will then grow under the influence of baroclinic vorticity deposited by the shock-interface interaction, although the perturbation growth rate will depend on the initial density contrast across the interface, the strength of the shock, and the amplitude of the perturbations [15]. RMI growth rates are also influenced by the physical properties of the materials involved such as the fluid

viscosity [17], yield strength [18], as well as surface tension [19]. Additional details regarding RMI are provided in Chapter 4.

While the role of viscosity and material strength on hydrodynamic instabilities has been studied through modeling, simulations, and experiments, the effect of surface tension on RMI growth rate has received comparatively little attention. Surface tension effects on shocked interfaces have been studied theoretically [19], numerically [20], and experimentally [21]. These studies have shown that surface tension acts to stabilize RTI/RMI instabilities for interfaces with small perturbations [19], while governing the process of interface breakup at larger amplitude cases [20, 21]. When surface tension stabilizes instability growth at a shocked interface, the result is oscillatory behavior about the mean interface. The latter scenario (larger amplitudes) involving droplet breakup can occur when RMI is triggered by a shock wave processing a spherical droplet, while the resulting breakup in to smaller, detached daughter droplets is governed by surface tension. This is observed for example in fuel atomization in supersonic combustion ramjets [22], where the fuel stream is first impinged by a shock wave to form a primary atomization, followed by surface tension-mediated secondary atomization, eventually resulting in the formation of fuel droplets from elongated fuel strands [20]. Note that surface tension plays a more pronounced role at smaller scales, and can thus significantly impact secondary atomization [22, 23]. This makes experimental studies of droplet formation challenging, due to the prohibitive requirements placed on diagnostics necessary to resolve small-scale breakup. Numerical approaches offer a viable alternative to investigate fundamental aspects of the effect of surface tension on compressible multi-medium flows.

The above discussion is summarized in figure 1.1, where a schematic shows a classification of such problems based on the flow Mach number ($Ma = u/a$) and the Weber number ($We = \rho u^2 l / \sigma$), as well as common engineering applications in the regime of high compressibility/high surface tension. Numerical codes capable of handling surface tension operate in the incompressible regime, while compressible flow codes developed for high-speed flows in gases do not typically include surface tension effects. To address this gap in capabilities, a new software application called IMPACT has been developed and described in this dissertation. IMPACT is a shock physics code with multi-medium and multi-phase capabilities, while surface tension is modeled using the Level Set [24, 25] (LS) and Ghost Fluid Methods [26] (GFM). We have developed new numerical methods that make IMPACT highly accurate for problems that feature sharp interfaces and discontinuities. These developments are reported in detail in this dissertation.
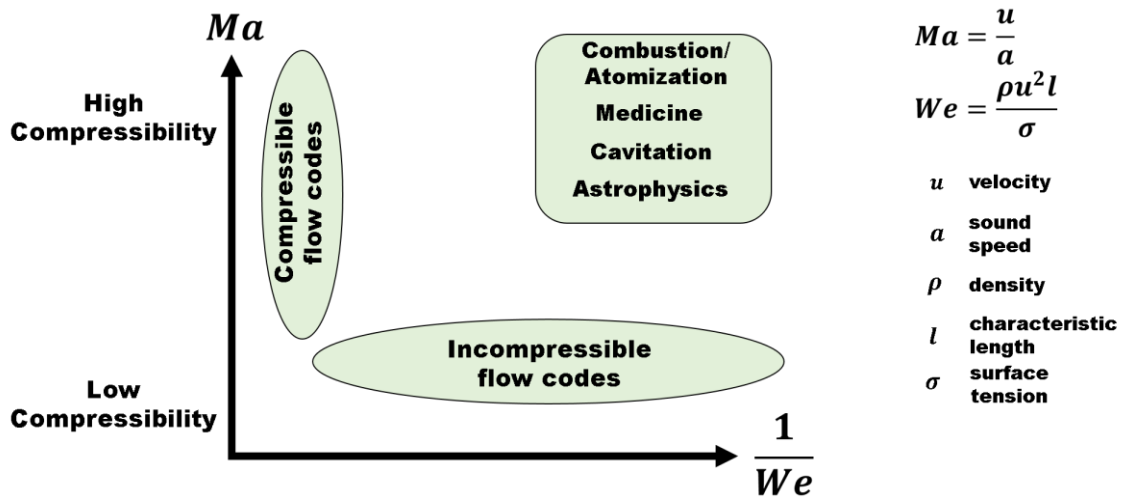
Figure 1.1. Schematic of regimes of interest in multi-phase problems with surface tension as observed in engineering applications.

Specific to IMPACT is the fully compressible approach of the code toward liquids and solids. In the problems mentioned above, the flow behavior is compressible, so that the density of the materials changes in response to pressure variations, and the resulting flow properties are poorly understood and require the application of specialized simulation tools. Furthermore, surface tension in multi-phase flows has been conventionally handled by treating one [27] or both [28] fluids as an incompressible liquid. However, this approach is inadequate in describing the complex physics that can occur when a shock wave is present in the flow. This occurs for instance in underwater explosions [29-31], where the presence of detonations/shocks creates acoustic waves in the liquid that cannot be ignored. Similarly, when a solid surface [32-34] is subjected to shocks, explosives, or ballistic loading, shocks can result within the solid material. The high-strain loading can melt the material, causing it to 'flow' like a liquid, or to 'flow with strength' if the loading is below melt conditions. This can occur, for instance when a water turbine blade or a pump works under the cavitation condition [18] or the shell of an armored tank is under attack from explosive loading. When an underwater explosion occurs near a solid structure, the solid material usually undergoes a plastic deformation, while the liquid evolves under the cavitating condition [18], giving rise to a complex solid-liquid-gas flow with varying densities, temperatures, and material properties. These dynamics are also important to astrophysical applications such as supernovae explosions. In supernovae detonations, exploding shock waves within the stellar core drive finger-like 'ejecta' structures to form, resulting in the ejection of heavier elements through space which 'seed' the formation of future solar systems and planets.

IMPACT employs a novel variation of the widely-used GFM to simulate compressible flows with surface tension. One of the aspects of IMPACT which make it a unique simulation tool for such flows is the introduction of the Efficient GFM (EGFM) for the treatment of 'overheating' at material interfaces. Overheating [26, 35] is a technical term for spurious over- and under-shoots in the temperature and density of materials at and near interfaces, stemming from implementation of the GFM to capture interfacial boundary conditions and remains a persistent numerical issue associated with the GFM. In Chapter 3, we will review different versions of the GFM and their approaches to addressing overheating. These approaches, however, are able to only *alleviate* [32, 36-39] overheating and cannot eliminate it from the numerical solution. In particular, the practical GFM [39] (PGFM) proposes a novel algorithm to reduce the overheating errors to a large extent, but still suffers from this numerical issue in different compressible multi-medium problems. The proposed EGFM is based on a lemma [40] (called the 'GFM Theorem' in this dissertation) and combined with the approach of the PGFM [39] to address overheating, results in complete elimination of overheating for compressible multi-medium flows. This is the central novelty of the work presented in this dissertation.

The rest of the dissertation is organized as follows: Chapter 2 is focused on the numerical methods implemented in IMPACT. Chapter 3 is focused on the GFM where the fundamentals of the approach and the methodology are presented, followed by a discussion of the variants of the GFM which are based on multi-medium Riemann solvers at the interface. Subsequently, the EGFM is introduced along with an explanation of the overheating treatment proposed through the EGFM approach. Chapter 4 includes a detailed presentation of our validation efforts for IMPACT including 1D single- and multi-medium

Riemann problems and various shock-interface interactions, results from different versions of the GFM, demonstration of overheating removal through the EGFM implementation; 2D problems include air bubble explosion, shock-bubble interactions, and shock-cavity interactions. In addition, results from several RMI cases with and without surface tension are presented. Finally, Chapter 5 includes a summary and conclusions of the dissertation.

CHAPTER 2: NUMERICAL METHODS

In this chapter, we describe the numerical methods used in IMPACT, a multi-material, shock physics code developed to investigate shocked multi-phase flows. IMPACT solves the Euler equations, while the interface boundary conditions are enforced through the GFM. Multiple variations of GFM are available in IMPACT, including a novel approach that will be discussed in Chapter 3. The use of the level set approach ensures accurate tracking of the material interface without recourse to explicit 'interface surgical' approaches. IMPACT also provides the capability to handle a wide range of materials with different equation of state (EOS) behaviors and transport properties. Advection is handled with a fifth order WENO method, while time-stepping is performed to third order using a TVD-RK approach.

2.1 Euler equations and Riemann problem

The governing equations for compressible flows are the Euler equations, which are given below in conservation form for a 1D problem:

$$
\begin{cases}
\dfrac{\partial \rho}{\partial t} + \dfrac{\partial (\rho u)}{\partial x} = 0, \\
\dfrac{\partial (\rho u)}{\partial t} + \dfrac{\partial}{\partial x}(\rho u^2 + p) = 0, \\
\dfrac{\partial (\rho E)}{\partial t} + \dfrac{\partial}{\partial x}[u(\rho E + p)] = 0.
\end{cases}
\tag{2.1}
$$

In vector form, these equations can be expressed as

$$
U_t + F(U)_x = 0
\tag{2.2}
$$

where U and F represent the vector of conserved variables and the vector of fluxes, respectively:

$$U = \begin{bmatrix} \rho \\ \rho u \\ \rho E \end{bmatrix} = \begin{bmatrix} u_1 \\ u_2 \\ u_3 \end{bmatrix}, \quad F(U) = \begin{bmatrix} \rho u \\ \rho u^2 + p \\ u(\rho E + p) \end{bmatrix} = \begin{bmatrix} f_1 \\ f_2 \\ f_3 \end{bmatrix}.$$

For flows with discontinuous initial conditions, a Riemann problem may be defined by applying the initial conditions

$$U(x,0) = \begin{cases} U_L, & x < x_0 \\ U_R, & x \geq x_0 \end{cases} \tag{2.3}$$

to the Euler equations. In eq. (2.3), U_L and U_R represent the states of matter to the left and to the right of the initial discontinuity located at x_0. In order to obtain the solution to the Riemann problem (denoted by $RP(U_L, U_R)$), the Jacobian matrix $A(U)$ associated with the system given in eq. (2.2) must be first determined:

$$\frac{\partial U}{\partial t} + \frac{\partial F}{\partial U} \frac{\partial U}{\partial x} = \frac{\partial U}{\partial t} + A(U) \frac{\partial U}{\partial x} = 0. \tag{2.4}$$

Here $A(U)$ is given by:

$$A(U) = \begin{bmatrix} \dfrac{\partial f_1}{\partial u_1} & \dfrac{\partial f_1}{\partial u_2} & \dfrac{\partial f_1}{\partial u_3} \\ \dfrac{\partial f_2}{\partial u_1} & \dfrac{\partial f_2}{\partial u_2} & \dfrac{\partial f_2}{\partial u_3} \\ \dfrac{\partial f_3}{\partial u_1} & \dfrac{\partial f_3}{\partial u_2} & \dfrac{\partial f_3}{\partial u_3} \end{bmatrix}. \tag{2.5}$$

The eigenvalues of the Jacobian matrix $A(U)$ are determined as:

$$\lambda_1 = u - a, \qquad \lambda_2 = u, \qquad \lambda_3 = u + a,$$

while the eigenvectors are

$$K^{(1)} = \begin{bmatrix} 1 \\ u - a \\ H - ua \end{bmatrix}, \qquad K^{(2)} = \begin{bmatrix} 1 \\ u \\ H - \frac{1}{2}u^2 \end{bmatrix}, \qquad K^{(3)} = \begin{bmatrix} 1 \\ u + a \\ H + ua \end{bmatrix}$$

where $H = E + p/\rho$ is the enthalpy, and a is the speed of sound given by:

$$a = \sqrt{\frac{\gamma(p + p_\infty)}{\rho}}. \qquad\qquad (2.6)$$

The solution to the above Riemann problem will consist of three waves, each of which corresponds to one of the eigenvalues and is depicted in $x - t$ plane as shown in figure 2.1. While the middle wave ($\lambda_2 = u$) is always a contact discontinuity, the outer waves can be rarefactions or shocks. In the example given in figure 2.1, U_{*L} and U_{*R} are the non-trivial solutions obtained from the initial conditions in eq. (2.3).
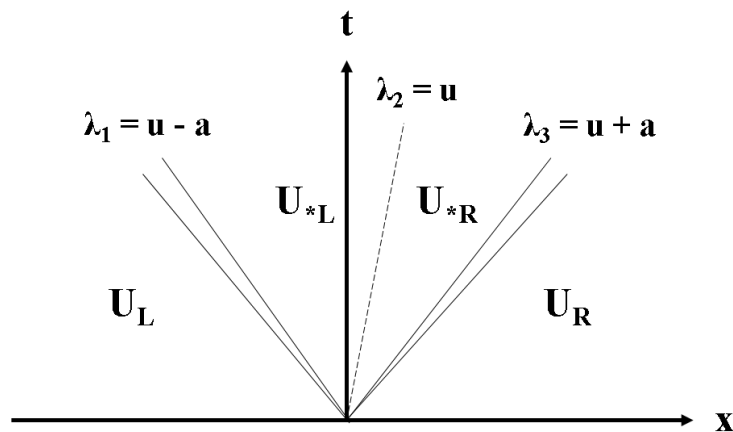
Figure 2.1. Example of the solution to the Riemann problem in $x - t$ plane. Figure is based on figure 3.1 from [41].

2.2 Godunov method

Since the Riemann problem involves discontinuities in the initial conditions and allows discontinuous solutions (contact surface and shock waves), solutions based on integral approaches such as finite volume techniques are preferred. The method of Godunov [42] provides such a scheme that is first order, and is applied to the cells shown in figure 2.2 as given below:

$$U_i^{n+1} = U_i^n + \frac{\Delta t}{\Delta x}\left[F_{i-\frac{1}{2}} - F_{i+\frac{1}{2}}\right]. \tag{2.7}$$

In eq. (2.7), U_i^n (U_i^{n+1}) is the cell average value in cell i at time step n ($n+1$), Δx is the cell size, Δt is the time step size derived from a CFL condition, and $F_{i-\frac{1}{2}}$ and $F_{i+\frac{1}{2}}$ are the average fluxes at the left and right boundaries of the cell i, respectively. The Godunov method has been implemented in IMPACT, while our implementation has been validated for multiple test cases. In the next section, numerical methods to calculate the cell fluxes are discussed.
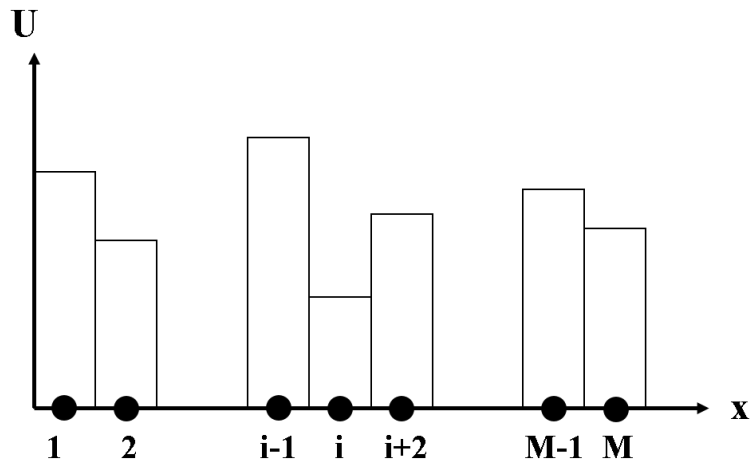
Figure 2.2. Discretized domain for the finite volume approach. Figure is based on figure 6.1 from [41].

2.3 Roe Riemann solver

The Roe Riemann solver [43] has been implemented in IMPACT to compute the cell fluxes in eq. (2.7), and was chosen due to its accuracy and robustness. The Roe solver relies on linearization of eq. (2.4) for the initial condition given by eq. (2.3). Thus, this method seeks an average state between U_L and U_R to linearize the Euler equations:

$$\frac{\partial U}{\partial t} + \hat{A}\frac{\partial U}{\partial x} = 0 \qquad (2.8)$$

where the linearized Jacobian matrix is a function of the initial condition: $\hat{A} = \hat{A}(U_L, U_R)$.

Roe averages are then defined as follows:

$$\begin{cases} \hat{\rho} = \sqrt{\rho_L \rho_R}, \\ \hat{u} = \dfrac{\sqrt{\rho_L} u_L + \sqrt{\rho_R} u_R}{\sqrt{\rho_L} + \sqrt{\rho_R}}, \\ \hat{H} = \dfrac{\sqrt{\rho_L} H_L + \sqrt{\rho_R} H_R}{\sqrt{\rho_L} + \sqrt{\rho_R}}. \end{cases} \qquad (2.9)$$

The eigenvalues of $\hat{A}$ are obtained as

$$\hat{\lambda}_1 = \hat{u} - \hat{a}, \qquad \hat{\lambda}_2 = \hat{u}, \qquad \hat{\lambda}_3 = \hat{u} + \hat{a}, \qquad (2.10)$$

while the eigenvectors are

$$\hat{K}^{(1)} = \begin{bmatrix} 1 \\ \hat{u} - \hat{a} \\ \hat{H} - \hat{u}\hat{a} \end{bmatrix}, \qquad \hat{K}^{(2)} = \begin{bmatrix} 1 \\ \hat{u} \\ \hat{H} - \frac{1}{2}\hat{u}^2 \end{bmatrix}, \qquad \hat{K}^{(3)} = \begin{bmatrix} 1 \\ \hat{u} + \hat{a} \\ \hat{H} + \hat{u}\hat{a} \end{bmatrix} \qquad (2.11)$$

where $\hat{a} = \sqrt{(\gamma - 1)\left(\hat{H} - \frac{1}{2}\hat{u}^2\right)}$ is the average speed of sound. The corresponding Roe solution is shown in figure 2.3. Note that owing to the linearization, the solution contains only discontinuities, while rarefactions are replaced by shock-like waves. In the system shown in figure 2.3, the following relations hold:

$$U_{*L} = U_L + \hat{\alpha}_1 \hat{K}^{(1)}, \qquad (2.12)$$

$$U_{*R} = U_{*L} + \hat{\alpha}_2 \hat{K}^{(2)}, \qquad (2.13)$$

$$U_R = U_{*R} + \hat{\alpha}_3 \hat{K}^{(3)} \qquad (2.14)$$

where $\hat{\alpha}_1$, $\hat{\alpha}_2$, and $\hat{\alpha}_3$ are wave strengths obtained from:
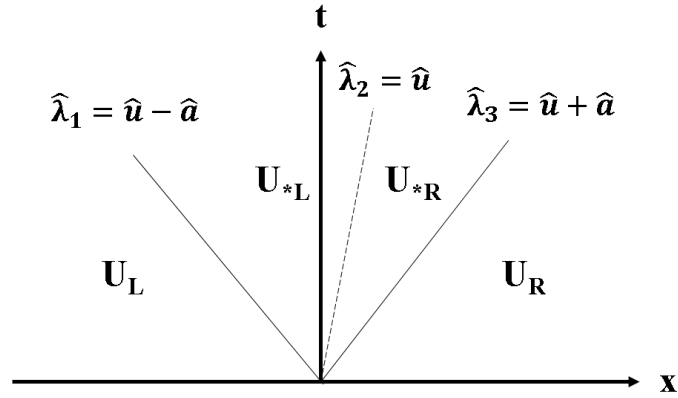
Figure 2.3. The Riemann solution obtained from the Roe method.

$$\begin{cases} \hat{\alpha}_1 = \dfrac{p_R - p_L - \hat{\rho}\hat{a}(u_R - u_L)}{2\hat{a}^2}, \\ \hat{\alpha}_2 = \rho_R - \rho_L - \dfrac{p_R - p_L}{\hat{a}^2}, \\ \hat{\alpha}_3 = \dfrac{p_R - p_L + \hat{\rho}\hat{a}(u_R - u_L)}{2\hat{a}^2}. \end{cases} \qquad (2.15)$$

The above algorithm is used to find $F_{i+\frac{1}{2}}$: A Riemann problem is defined between cells 'i'

and '$i + 1$' ($RP(U_i, U_{i+1})$). Roe averages, eigenvalues, eigenvectors, and wave strengths

are calculated, and the intercell flux at '$i + \frac{1}{2}$' is found using:

$$F_{i+\frac{1}{2}} = \frac{1}{2}(F_L + F_R) - \frac{1}{2}\left[\hat{\alpha}_1|\hat{\lambda}_1|\hat{K}^{(1)} + \hat{\alpha}_2|\hat{\lambda}_2|\hat{K}^{(2)} + \hat{\alpha}_3|\hat{\lambda}_3|\hat{K}^{(3)}\right] \qquad (2.16)$$

where $F_L = F(U_L)$ and $F_R = F(U_R)$. This procedure is applied to all intercells in the

domain, and eq. (2.7) is then used to update the solution to the next time step.

Finally, the rarefaction waves in the solution must be treated separately. Since the Roe

solver linearizes the Euler equations, a linear system is solved resulting in a solution that

can only contain shock waves (no rarefactions). It has been shown that when there exists a

sonic rarefaction in the solution, the shock representation of the rarefaction wave is not

accurate and the flux has to be modified through an entropy fix. This treatment is referred to as the Harten-Hyman [44] entropy fix and has been used in the current work.

2.4 Weighted Essentially Non-Oscillatory reconstruction

We have implemented higher-order numerical schemes in IMPACT, to avoid the highly diffusive treatment of discontinuities observed in the Godunov method. High-order methods provide a more accurate solution to the Riemann problem by utilizing various reconstruction schemes to assign a pair of "equivalent" values to each intercell at which the Riemann solution (Roe solution in the current work) is to be obtained. For example, for the intercell '$i + \frac{1}{2}$', $RP\left(U_{i+\frac{1}{2},L}^{eq}, U_{i+\frac{1}{2},R}^{eq}\right)$ is solved instead of $RP(U_i, U_{i+1})$.

Weighted essentially non-oscillatory (WENO) [45, 46] reconstruction is a high-order approach for problems involving shocks and discontinuities. In the WENO approach, the stencils of points or cells formed to reconstruct polynomials are assigned different weights depending on the presence of discontinuities and sharp gradients. In this approach, the highest weights are allocated to smooth stencils, whereas weights for stencils with shocks and contact surfaces are negligible. This approach ensures a high order of accuracy globally. Additional details are given in [47], including a review of WENO schemes for convection-dominated problems.

In the present work, a fifth-order WENO scheme, hereinafter referred as WENO5, is adopted for flux reconstruction. Thus, to obtain the equivalent values for the left and right boundaries of cell 'i' in figure 2.4 ($U_{i-\frac{1}{2},R}^{eq}$ and $U_{i+\frac{1}{2},L}^{eq}$, respectively), WENO5 requires information from two cells on either side of the cell and introduces three different stencils to reconstruct the required polynomials as follows:
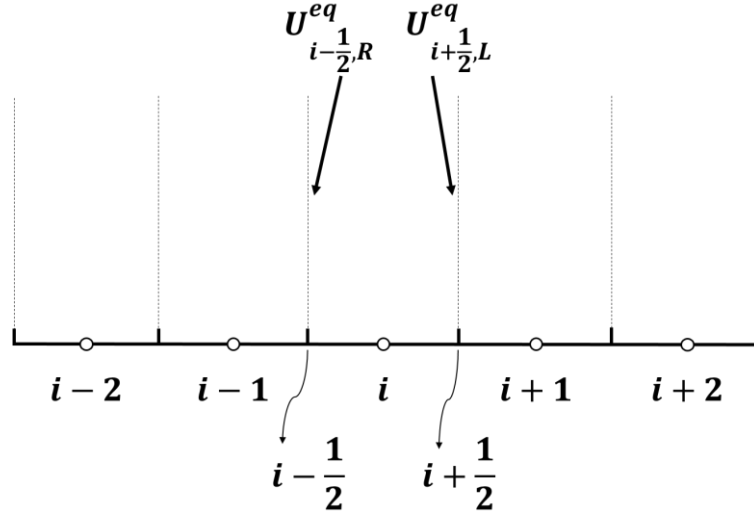
Figure 2.4. Required cells for WENO5 reconstruction.

$$S_0 = \{U_i, U_{i+1}, U_{i+2}\}, \quad S_1 = \{U_{i-1}, U_i, U_{i+1}\}, \quad S_2 = \{U_{i-2}, U_{i-1}, U_i\}.$$

For each stencil, the Lagrange method of interpolation is utilized to find reconstructed

values at the intercells '$i + \frac{1}{2}$' and '$i - \frac{1}{2}$', respectively:

$$U^{(0)}_{i+\frac{1}{2}} = \frac{1}{3}U_i + \frac{5}{6}U_{i+1} - \frac{1}{6}U_{i+2},$$

$$U^{(1)}_{i+\frac{1}{2}} = -\frac{1}{6}U_{i-1} + \frac{5}{6}U_i + \frac{1}{3}U_{i+1}, \qquad (2.17)$$

$$U^{(2)}_{i+\frac{1}{2}} = \frac{1}{3}U_{i-2} - \frac{7}{6}U_{i-1} + \frac{11}{6}U_i,$$

$$U^{(0)}_{i-\frac{1}{2}} = \frac{11}{6}U_i - \frac{7}{6}U_{i+1} + \frac{1}{3}U_{i+2},$$

$$U^{(1)}_{i-\frac{1}{2}} = \frac{1}{3}U_{i-1} + \frac{5}{6}U_i - \frac{1}{6}U_{i+1}, \qquad (2.18)$$

$$U^{(2)}_{i-\frac{1}{2}} = -\frac{1}{6}U_{i-2} + \frac{5}{6}U_{i-1} + \frac{1}{3}U_i.$$

For each stencil, smoothness of data is computed to determine the magnitude of weights that is to be assigned. *Smoothness indicators* are computed using

$$\beta_0 = \frac{13}{12}(U_i - 2U_{i+1} + U_{i+2})^2 + \frac{1}{4}(3U_i - 4U_{i+1} + U_{i+2})^2,$$

$$\beta_1 = \frac{13}{12}(U_{i-1} - 2U_i + U_{i+1})^2 + \frac{1}{4}(U_{i-1} - U_{i+1})^2, \qquad (2.19)$$

$$\beta_2 = \frac{13}{12}(U_{i-2} - 2U_{i-1} + U_i)^2 + \frac{1}{4}(U_{i-2} - 4U_{i-1} + 3U_i)^2.$$

Subsequently, the weights for the intercells '$i + \frac{1}{2}$' and '$i - \frac{1}{2}$' are found using:

$$\omega_r = \frac{\alpha_r}{\alpha_0 + \alpha_1 + \alpha_2}, \qquad \widetilde{\omega}_r = \frac{\widetilde{\alpha}_r}{\widetilde{\alpha}_0 + \widetilde{\alpha}_1 + \widetilde{\alpha}_2}, \qquad r = 0,1,2 \qquad (2.20)$$

with α_r and $\widetilde{\alpha}_r$ taken as

$$\alpha_r = \frac{d_r}{(\beta_r + 10^{-6})^2}, \qquad \widetilde{\alpha}_r = \frac{\widetilde{d}_r}{(\beta_r + 10^{-6})^2}, \qquad r = 0,1,2 \qquad (2.21)$$

and $d_0 = 0.3$, $d_1 = 0.6$, $d_2 = 0.1$, $\widetilde{d}_0 = 0.1$, $\widetilde{d}_1 = 0.6$, $\widetilde{d}_2 = 0.3$. Finally, the reconstructed values obtained in eqs. (2.17) and (2.18) are combined with the weights in eq. (2.20) to compute the equivalent values:

$$U^{eq}_{i+\frac{1}{2},L} = \omega_0 U^{(0)}_{i+\frac{1}{2}} + \omega_1 U^{(1)}_{i+\frac{1}{2}} + \omega_2 U^{(2)}_{i+\frac{1}{2}}, \qquad (2.22)$$

$$U^{eq}_{i-\frac{1}{2},R} = \widetilde{\omega}_0 U^{(0)}_{i-\frac{1}{2}} + \widetilde{\omega}_1 U^{(1)}_{i-\frac{1}{2}} + \widetilde{\omega}_2 U^{(2)}_{i-\frac{1}{2}}. \qquad (2.23)$$

From the equivalent values computed for each cell, the corresponding Riemann problems are formed and solved. The above implementation of WENO is referred as component-wise, since the reconstruction procedure is applied to each component of U using the same approach.

2.5 Extension to 2D problems

The extension of the numerical methods discussed above to 2D problems is presented in this section. The Euler equations for conservation of mass, momentum, and energy are given in 2D according to:

$$
\begin{cases}
\dfrac{\partial \rho}{\partial t} + \dfrac{\partial (\rho u)}{\partial x} + \dfrac{\partial (\rho v)}{\partial y} = 0, \\[2mm]
\dfrac{\partial (\rho u)}{\partial t} + \dfrac{\partial}{\partial x}(\rho u^2 + p) + \dfrac{\partial}{\partial y}(\rho uv) = 0, \\[2mm]
\dfrac{\partial (\rho v)}{\partial t} + \dfrac{\partial}{\partial x}(\rho uv) + \dfrac{\partial}{\partial y}(\rho v^2 + p) = 0, \\[2mm]
\dfrac{\partial (\rho E)}{\partial t} + \dfrac{\partial}{\partial x}[u(\rho E + p)] + \dfrac{\partial}{\partial y}[v(\rho E + p)] = 0.
\end{cases}
\tag{2.24}
$$

In vector form, the equations are given as

$$
U_t + F(U)_x + G(U)_y = 0
\tag{2.25}
$$

where U, $F(U)$, and $G(U)$ represent the vector of conserved variables, and the vector of fluxes in the x-, and y-directions, respectively:

$$
U = \begin{bmatrix} \rho \\ \rho u \\ \rho v \\ \rho E \end{bmatrix} = \begin{bmatrix} u_1 \\ u_2 \\ u_3 \\ u_4 \end{bmatrix}, \quad
F(U) = \begin{bmatrix} \rho u \\ \rho u^2 + p \\ \rho uv \\ u(\rho E + p) \end{bmatrix} = \begin{bmatrix} f_1 \\ f_2 \\ f_3 \\ f_4 \end{bmatrix}, \quad
G(U) = \begin{bmatrix} \rho v \\ \rho uv \\ \rho v^2 + p \\ v(\rho E + p) \end{bmatrix} = \begin{bmatrix} g_1 \\ g_2 \\ g_3 \\ g_4 \end{bmatrix}.
$$

To find the eigenstructure associated with the 2D Euler equations, the Jacobian matrices of eq. (2.25) are first determined according to

$$
\frac{\partial U}{\partial t} + \frac{\partial F}{\partial U}\frac{\partial U}{\partial x} + \frac{\partial G}{\partial U}\frac{\partial U}{\partial y} = \frac{\partial U}{\partial t} + A(U)\frac{\partial U}{\partial x} + B(U)\frac{\partial U}{\partial y} = 0
\tag{2.26}
$$

where $A(U)$ is given by

$$A(U) = \begin{bmatrix} \dfrac{\partial f_1}{\partial u_1} & \dfrac{\partial f_1}{\partial u_2} & \dfrac{\partial f_1}{\partial u_3} & \dfrac{\partial f_1}{\partial u_4} \\ \dfrac{\partial f_2}{\partial u_1} & \dfrac{\partial f_2}{\partial u_2} & \dfrac{\partial f_2}{\partial u_3} & \dfrac{\partial f_2}{\partial u_4} \\ \dfrac{\partial f_3}{\partial u_1} & \dfrac{\partial f_3}{\partial u_2} & \dfrac{\partial f_3}{\partial u_3} & \dfrac{\partial f_3}{\partial u_4} \\ \dfrac{\partial f_4}{\partial u_1} & \dfrac{\partial f_4}{\partial u_2} & \dfrac{\partial f_4}{\partial u_3} & \dfrac{\partial f_4}{\partial u_4} \end{bmatrix} \tag{2.27}$$

with eigenvalues and eigenvectors given by

$$\lambda_1 = u - a, \qquad \lambda_2 = \lambda_3 = u, \qquad \lambda_4 = u + a,$$

$$K^{(1)} = \begin{bmatrix} 1 \\ u - a \\ v \\ H - ua \end{bmatrix}, \qquad K^{(2)} = \begin{bmatrix} 1 \\ u \\ v \\ \frac{1}{2}(u^2 + v^2) \end{bmatrix}, \qquad K^{(3)} = \begin{bmatrix} 0 \\ 0 \\ 1 \\ v \end{bmatrix}, \qquad K^{(4)} = \begin{bmatrix} 1 \\ u + a \\ v \\ H + ua \end{bmatrix},$$

while $B(U)$ is given by

$$B(U) = \begin{bmatrix} \dfrac{\partial g_1}{\partial u_1} & \dfrac{\partial g_1}{\partial u_2} & \dfrac{\partial g_1}{\partial u_3} & \dfrac{\partial g_1}{\partial u_4} \\ \dfrac{\partial g_2}{\partial u_1} & \dfrac{\partial g_2}{\partial u_2} & \dfrac{\partial g_2}{\partial u_3} & \dfrac{\partial g_2}{\partial u_4} \\ \dfrac{\partial g_3}{\partial u_1} & \dfrac{\partial g_3}{\partial u_2} & \dfrac{\partial g_3}{\partial u_3} & \dfrac{\partial g_3}{\partial u_4} \\ \dfrac{\partial g_4}{\partial u_1} & \dfrac{\partial g_4}{\partial u_2} & \dfrac{\partial g_4}{\partial u_3} & \dfrac{\partial g_4}{\partial u_4} \end{bmatrix} \tag{2.28}$$

with eigenvalues and eigenvectors given by

$$\lambda_1 = v - a, \qquad \lambda_2 = \lambda_3 = v, \qquad \lambda_4 = v + a,$$

$$K^{(1)} = \begin{bmatrix} 1 \\ u \\ v - a \\ H - va \end{bmatrix}, \qquad K^{(2)} = \begin{bmatrix} 1 \\ u \\ v \\ \frac{1}{2}(u^2 + v^2) \end{bmatrix}, \qquad K^{(3)} = \begin{bmatrix} 0 \\ 1 \\ 0 \\ u \end{bmatrix}, \qquad K^{(4)} = \begin{bmatrix} 1 \\ u \\ v + a \\ H + va \end{bmatrix}.$$

The extension of the Godunov method to 2D problems is straightforward and given by

$$U_{i,j}^{n+1} = U_{i,j}^n + \frac{\Delta t}{\Delta x}\left[F_{i-\frac{1}{2},j} - F_{i+\frac{1}{2},j}\right] + \frac{\Delta t}{\Delta y}\left[G_{i,j-\frac{1}{2}} - G_{i,j+\frac{1}{2}}\right] \qquad (2.29)$$

where fluxes are as depicted in figure 2.5.
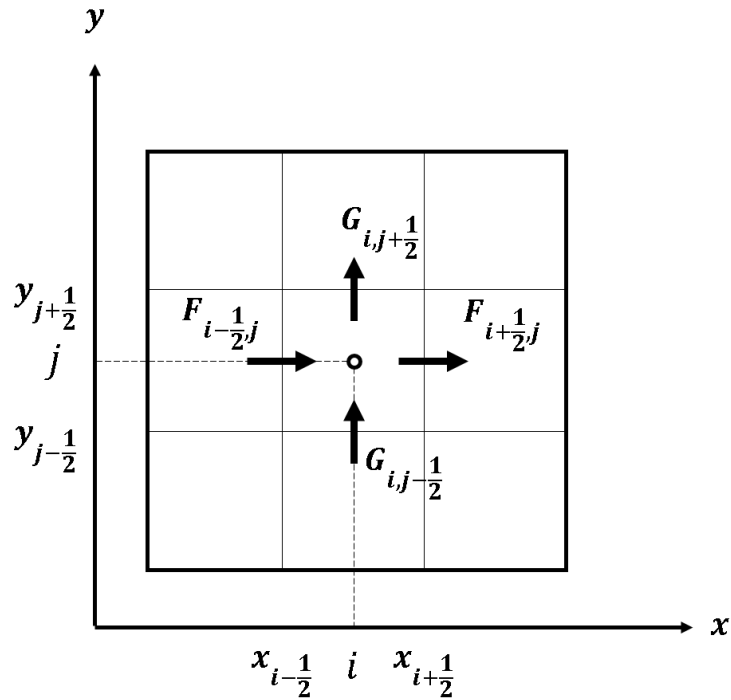
Figure 2.5. Fluxes on the boundaries of cell '(i,j)'.

Similar to the 1D case, a Riemann problem can be defined along each direction, and solved at each intercell to obtain fluxes. For example, for fluxes in the x direction ($F_{i+\frac{1}{2},j}$), the corresponding Riemann problem is

$$\begin{cases} U_t + F(U)_x = 0, \\ U(x,0) = \begin{cases} U_{i,j}^n, & x < x_{i+\frac{1}{2}} \\ U_{i+1,j}^n, & x \geq x_{i+\frac{1}{2}} \end{cases}, \end{cases} \qquad (2.30)$$

and for fluxes in the y direction ($G_{i,j+\frac{1}{2}}$), the Riemann problem is

$$\begin{cases} U_t + G(U)_y = 0, \\ U(y,0) = \begin{cases} U_{i,j}^n, & y < y_{j+\frac{1}{2}} \\ U_{i,j+1}^n, & y \geq y_{j+\frac{1}{2}} \end{cases} \end{cases} \qquad (2.31)$$

The Riemann problems given in eqs. (2.30) and (2.31) are solved using an extension of the

Roe solver [43] presented for the 1D case. To find $F_{i+\frac{1}{2},j}$, the eigenvalues and eigenvectors

associated with $\hat{A}$ and the wave strengths are calculated as follows:

$$\hat{\lambda}_1 = \hat{u} - \hat{a}, \qquad \hat{\lambda}_2 = \hat{\lambda}_3 = \hat{u}, \qquad \hat{\lambda}_4 = \hat{u} + \hat{a}, \qquad (2.32)$$

$$\widehat{K}^{(1)} = \begin{bmatrix} 1 \\ \hat{u} - \hat{a} \\ \hat{v} \\ \widehat{H} - \hat{u}\hat{a} \end{bmatrix}, \widehat{K}^{(2)} = \begin{bmatrix} 1 \\ \hat{u} \\ \hat{v} \\ \frac{1}{2}(\hat{u}^2 + \hat{v}^2) \end{bmatrix}, \widehat{K}^{(3)} = \begin{bmatrix} 0 \\ 0 \\ 1 \\ \hat{v} \end{bmatrix}, \widehat{K}^{(4)} = \begin{bmatrix} 1 \\ \hat{u} + \hat{a} \\ \hat{v} \\ \widehat{H} + \hat{u}\hat{a} \end{bmatrix}, \qquad (2.33)$$

$$\begin{cases} \hat{\alpha}_1 = \dfrac{p_R - p_L - \hat{\rho}\hat{a}(u_R - u_L)}{2\hat{a}^2}, \\ \hat{\alpha}_2 = \rho_R - \rho_L - \dfrac{p_R - p_L}{\hat{a}^2}, \\ \hat{\alpha}_3 = \hat{\rho}(v_R - v_L), \\ \hat{\alpha}_4 = \dfrac{p_R - p_L + \hat{\rho}\hat{a}(u_R - u_L)}{2\hat{a}^2}, \end{cases} \qquad (2.34)$$

where $\hat{a} = \sqrt{(\gamma - 1)\left(\widehat{H} - \frac{1}{2}(\hat{u}^2 + \hat{v}^2)\right)}$ is the speed of sound, and the indices 'L' and 'R'

refer to the cells '(i,j)' and '$(i+1,j)$', respectively. The Roe flux is then computed using

$$F_{i+\frac{1}{2},j} = \frac{1}{2}(F_L + F_R) - \frac{1}{2}\left[\hat{\alpha}_1|\hat{\lambda}_1|\widehat{K}^{(1)} + \hat{\alpha}_2|\hat{\lambda}_2|\widehat{K}^{(2)} + \hat{\alpha}_3|\hat{\lambda}_3|\widehat{K}^{(3)} + \hat{\alpha}_4|\hat{\lambda}_4|\widehat{K}^{(4)}\right]. \quad (2.35)$$

To find $G_{i,j+\frac{1}{2}}$, the eigenvalues and eigenvectors associated with $\hat{B}$ and the wave strengths

are calculated as follows:

$$\hat{\lambda}_1 = \hat{v} - \hat{a}, \qquad \hat{\lambda}_2 = \hat{\lambda}_3 = \hat{v}, \qquad \hat{\lambda}_4 = \hat{v} + \hat{a}, \qquad (2.36)$$

$$\widehat{K}^{(1)} = \begin{bmatrix} 1 \\ \hat{u} \\ \hat{v} - \hat{a} \\ \hat{H} - \hat{v}\hat{a} \end{bmatrix}, \widehat{K}^{(2)} = \begin{bmatrix} 1 \\ \hat{u} \\ \hat{v} \\ \frac{1}{2}(\hat{u}^2 + \hat{v}^2) \end{bmatrix}, \widehat{K}^{(3)} = \begin{bmatrix} 0 \\ 1 \\ 0 \\ \hat{u} \end{bmatrix}, \widehat{K}^{(4)} = \begin{bmatrix} 1 \\ \hat{u} \\ \hat{v} + \hat{a} \\ \hat{H} + \hat{v}\hat{a} \end{bmatrix}, \qquad (2.37)$$

$$\begin{cases} \hat{\alpha}_1 = \dfrac{p_R - p_L - \hat{\rho}\hat{a}(v_R - v_L)}{2\hat{a}^2}, \\ \quad \hat{\alpha}_2 = \rho_R - \rho_L - \dfrac{p_R - p_L}{\hat{a}^2}, \\ \quad \hat{\alpha}_3 = \hat{\rho}(u_R - u_L), \\ \hat{\alpha}_4 = \dfrac{p_R - p_L + \hat{\rho}\hat{a}(v_R - v_L)}{2\hat{a}^2}, \end{cases} \qquad (2.38)$$

where the indices 'L' and 'R' refer to the cells '(i,j)' and '$(i, j + 1)$', respectively. The flux is then computed according to

$$G_{i,j+\frac{1}{2}} = \frac{1}{2}(G_L + G_R) - \frac{1}{2}\left[\hat{\alpha}_1|\hat{\lambda}_1|\widehat{K}^{(1)} + \hat{\alpha}_2|\hat{\lambda}_2|\widehat{K}^{(2)} + \hat{\alpha}_3|\hat{\lambda}_3|\widehat{K}^{(3)} + \hat{\alpha}_4|\hat{\lambda}_4|\widehat{K}^{(4)}\right]. \quad (2.39)$$

Note that should the solutions of Riemann problems in eqs. (2.30) and (2.31) contain sonic rarefactions, the Harten-Hyman [44] entropy fix must be applied to obtain the correct flux values.

The WENO5 implementation given in §2.4 avoids stencils with sharp gradients by designating the lower weights to them, while maintaining fifth-order accuracy globally. The simplest extension of the WENO5 method to 2D problems involves implementing the scheme using a direction-by-direction approach. However, it was shown in [48] that this approach yields fifth-order accuracy only for linear problems, while for nonlinear problems (such as the Euler equations), it results in a second-order-accurate solution. In the current work, the direction by direction approach is used, while an extension to higher-order accuracy [48] is planned.

2.6 Level set method

In IMPACT, the interface motion is described using the LS approach introduced in Chapter

1. The motion of an interface is represented by a LS function, and is modeled using

$$\frac{\partial \phi}{\partial t} + u \frac{\partial \phi}{\partial x} + v \frac{\partial \phi}{\partial y} = 0. \tag{2.40}$$

Note that the LS function should be chosen such that it produces an accurate description of

the interface between two media. For instance, if the interface is a circle with center

(x_0, y_0) and radius R, a possible choice for the LS function will be:

$$\phi(x, y) = (x - x_0)^2 + (y - y_0)^2 - R^2.$$

However, LS functions that satisfy the property $|\nabla \phi| = 1$ (referred as signed-distance

functions [25]) have been shown [49] to produce interface behavior with high accuracy.

As the interface evolves, the signed-distance property of the LS function must be enforced

at every time step. This step is called reinitialization (introduced by Sussman et al. [49]),

and is enforced by numerically solving the equation below:

$$\frac{\partial \phi}{\partial \tau} + S(\phi_0)(|\nabla \phi| - 1) = 0. \tag{2.41}$$

In eq. (2.41), τ is a time-like variable, and $S(\phi_0)$ is the sign function defined by:

$$S(\phi_0) = \frac{\phi_0}{\sqrt{\phi_0^2 + (\Delta x)^2}} \tag{2.42}$$

with $\phi_0(x, y)$ being the LS function before reinitialization. Note that when eq. (2.41) is

solved to steady state, ϕ approaches a signed distance function. Reinitialization leads to

more accurate determination of the unit normal vectors and curvature of the interface that

are in turn computed using:

$$\widehat{N} = \frac{\nabla \phi}{|\nabla \phi|} \tag{2.43}$$

and

$$\kappa = \nabla . \widehat{N} \quad . \tag{2.44}$$

Determining the interface curvature to high order is required to accurately compute surface tension effects on the interface. Equations (2.40) and (2.41) belong to the Hamilton-Jacobi category and are solved using high-order upwinding schemes. Following [26, 50], WENO5 is used to compute left- and right-sided spatial derivatives of ϕ. Equation (2.40) is solved in a band of cells around the interface following the approach in [51].

Note that applying the WENO5 method of [50] to the solution of eq. (2.41) gives solutions that are only second-order accurate at best resulting in noisy interface curvatures [50, 52, 53]. An alternative is the higher-order method proposed in [54], which yields second-order accuracy in solving eq. (2.41), resulting in more accurate interface locations compared to [50]. This method is also capable of handling situations in which the ϕ_0 function is steep or shallow (i.e. $|\nabla \phi_0|$ is very different from unity), without the need for complex modifications to the sign function (eq. (2.42)) as carried out by [51]. In the current work, however, the numerical method of [53] is used, which is an extension of [54] such that all the benefits of [54] are retained, while resulting in fourth-order accuracy for eq. (2.41) and curvature calculations that are second-order accurate. Similar to eq. (2.40), eq. (2.41) is also solved in a band of cells around the interface, following [51].

2.7 Time discretization

Time advancement is implemented in IMPACT to a high order of accuracy using the total variation diminishing (TVD) Runge-Kutta [55] (RK) scheme. We use a third-order TVD-RK method for solving eqs. (2.7), (2.29), (2.40), and (2.41), where the solution is advanced over three sub-steps per time step. Writing the governing equations in general form, we obtain

$$\frac{d\Theta}{dT} = L(\Theta) \tag{2.45}$$

where Θ may be the vector of conserved variables (U in eqs. (2.7) and (2.29)) or the LS function (ϕ in eqs. (2.40) and (2.41)), T may denote real (t) or fictitious (τ) time, and L is the appropriate spatial discretization from the numerical methods for each of the equations. The third-order TVD-RK implementation for eq. (2.45) is written as [55]

$$\Theta^{(1)} = \Theta^n + \Delta T L(\Theta^n),$$

$$\Theta^{(2)} = \frac{3}{4}\Theta^n + \frac{1}{4}\Theta^{(1)} + \frac{1}{4}\Delta T L(\Theta^{(1)}), \tag{2.46}$$

$$\Theta^{n+1} = \frac{1}{3}\Theta^n + \frac{2}{3}\Theta^{(2)} + \frac{2}{3}\Delta T L(\Theta^{(2)})$$

where $\Theta^{(1)}$, $\Theta^{(2)}$, and Θ^{n+1} are the solutions after the first, second, and final sub steps, respectively.

CHAPTER 3: THE GHOST FLUID METHOD

3.1 Introduction

The Ghost Fluid Method (GFM) was originally developed by Fedkiw et al. [26] to model

contact discontinuities in inviscid, compressible, multi-material flows. The GFM is based

on applying physically accurate interfacial boundary conditions at the material interface

between different fluids. Consider two fluids (A and B) separated by an interface that is

moving as shown in figure 3.1. Fluids A and B may be distinguished by an LS function,

where $\phi \leq 0$ corresponds to Fluid A, $\phi > 0$ indicates Fluid B, and the $\phi = 0$ level set

identifies the interface. In the GFM approach, the effect of Fluid B on Fluid A is modeled

through appropriately chosen boundary conditions enforced at the interface by replacing

Fluid B with a 'ghost fluid'. Similarly, Fluid A can be replaced with a ghost fluid, and in

conjunction with interface boundary conditions represents the effect of Fluid A on B. This

is shown in figures 3.1 and 3.2.
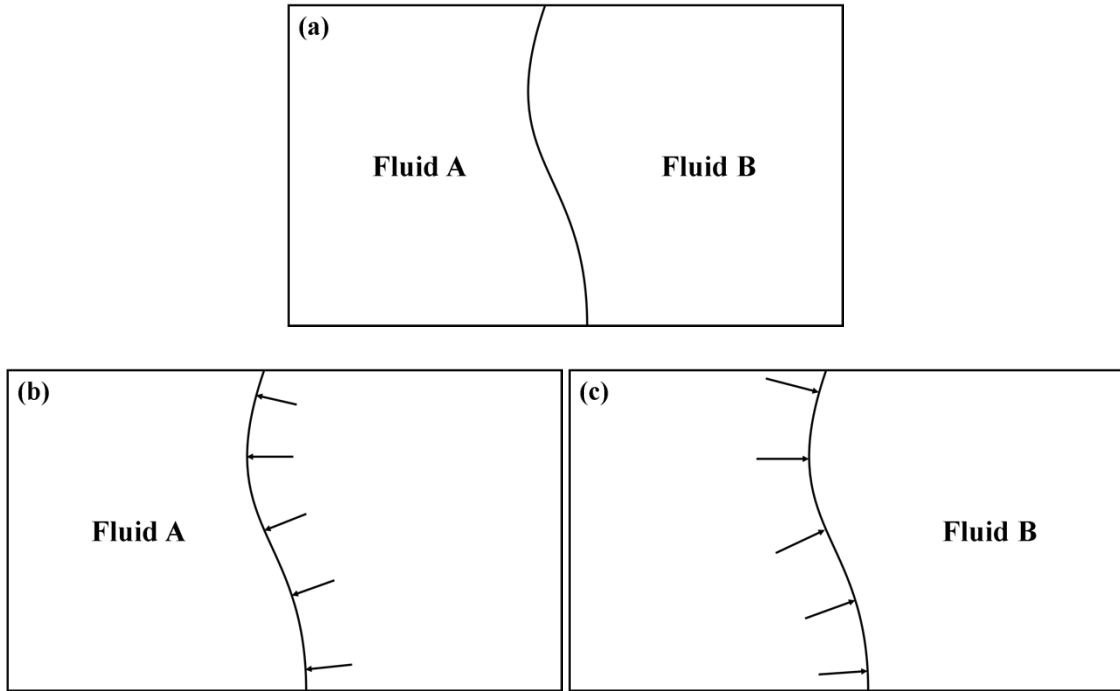
Figure 3.1. The GFM approach to treating Fluids A and B separated by an interface. (a) Actual domain, (b) interfacial boundary condition applied to Fluid A, (c) interfacial boundary condition applied to Fluid B.
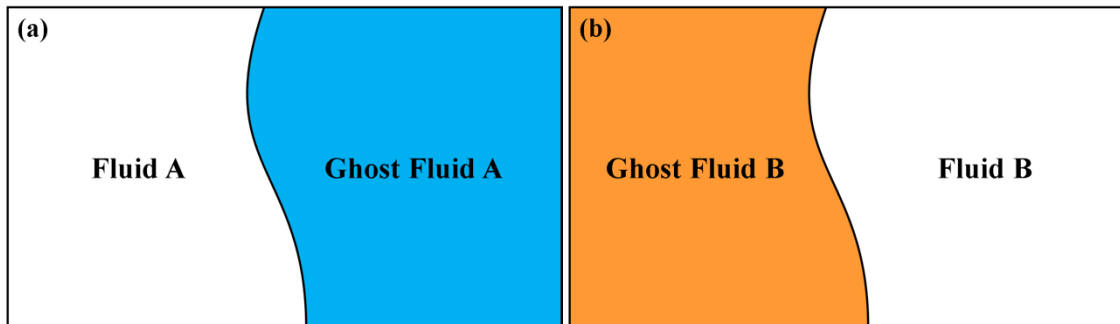
Figure 3.2. Applying interfacial boundary condition using (a) Ghost Fluid A, and (b) Ghost Fluid B.

The efficacy of the GFM approach therefore lies in accurately applying the interfacial boundary conditions between the real fluids in each case using their 'ghost' counterparts. In [25], the authors show that Rankine-Hugoniot jump conditions, i.e. flux conservation,

when applied across the interface yield interfacial conditions that ensure the continuity of *pressure* and *normal velocity*. In [26], the authors define the ghost fluids based on the interfacial flux conservation discussed above. They propose using the pressure and velocity of Fluid B (Fluid A) for Ghost Fluid A (Ghost Fluid B), while the density of Ghost Fluid A (Ghost Fluid B) comes directly from Fluid A (Fluid B) through constant extrapolation. In numerical calculations, however, the ghost fluids are defined over a band of cells on either side of the interface for reasons of computational expediency. Fedkiw et al. [26] suggest using a band of 3 to 5 ghost cells depending on the computational stencil required to implement a specific numerical scheme and interface displacement. Once the ghost cells are populated, the fluid pairs (Fluid A+Ghost Fluid A) and (Fluid B+Ghost Fluid B) can each be updated independently with their corresponding EOS using standard single-medium numerical schemes, without requiring specific treatments for the interface or the need for cut cells. Often, the GFM is coupled with the LS approach [25-27], where the LS function is updated by solving eq. (2.40) to determine the new location of the interface. The above approach results in a *sharp representation* of the interface, which is a central feature of the GFM, when compared with other interface approaches including the VOF method [56], mass fraction methods [57], and gamma-based models [57, 58] all of which diffuse the interface over multiple cells, giving rise to 'numerical mixing' between the two fluids. This property of the GFM makes it suitable for simulations of multi-material problems involving interfacial phenomena such as problems with interfacial instabilities, surface tension effects, and evaporation.

Figure 3.3 shows an example where results from the GFM are compared to exact solution as well as results from a diffusive approach [58]. As seen in the figure, the density profile

from the GFM is sharp at the interface. However, the numerical solution from the GFM is slightly different from the analytical values near the interface following shock passage. This behavior of the GFM solution is termed overheating [35], and occurs when a shock wave interacts with an initially sharp interface. It has been shown [39] that overheating results from numerical inaccuracies that stem from applying single-medium numerical schemes to the fluid pairs (Fluid A+Ghost Fluid A) and (Fluid B+Ghost Fluid B). Since these schemes are naturally associated with diffusion, they give rise to overheating. In the next section, overheating will be discussed in greater detail along with a proposed novel approach to address the issue.
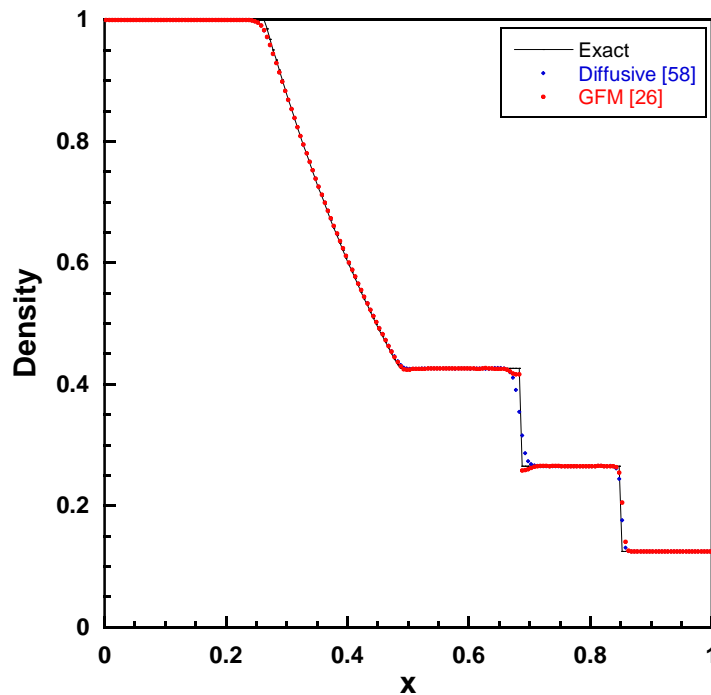
Figure 3.3. Sharp representation of the interface with the GFM approach. Overheating is observed near the interface.

Figure 3.4 (based on figure 1 from [26]) depicts the methodology adopted for the population of the ghost cells for 1D problems using the GFM framework. Ghost Fluid A is

defined by copying node by node, the corresponding pressures and velocities from Fluid

B, while the density is obtained from constant extrapolation from Fluid A. Ghost Fluid B

is defined in a similar manner. A similar approach is used in multi-dimensional problems,

where the pressure and velocity values for the ghost cells are copied directly from the real

fluids, while densities are extrapolated using the following equation:

$$\frac{\partial \rho}{\partial \tau} \pm \widehat{N} \cdot \nabla \rho = 0 \ . \tag{3.1}$$

Eq. (3.1) is used with $+(-)$ for Ghost Fluid A (B), while the interface normal vector $\widehat{N}$ is

defined using the function ϕ through eq. (2.43). Note that the unit normal vector is taken

to point from Fluid A ($\phi \leq 0$) towards Fluid B ($\phi > 0$).
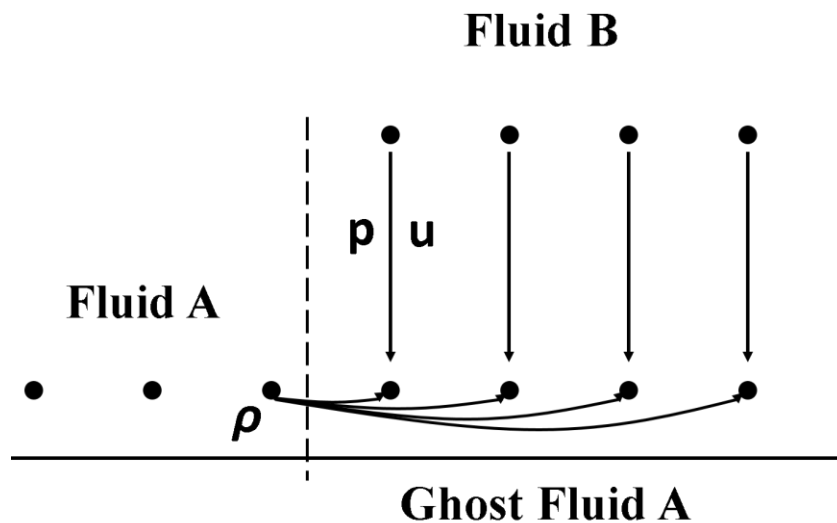
Figure 3.4. Definition of Ghost Fluid A using density extrapolation from Fluid A, and the velocity and pressure values from Fluid B. Figure is based on figure 1 from [26].

The GFM approach is thus easy to implement, and avoids the difficulties associated with

implementing cut cells or the use of complicated mixture rules [58, 59]. As a result of these

properties, the GFM has been widely used in different problems in science and engineering.

Fedkiw et al. [60] used the GFM for modeling deflagration and detonation discontinuities; Liu et al. [61] utilized the GFM approach to capture the boundary conditions for the variable coefficient Poisson equation; Kang et al. [28] exploited the methods in [61] to propose a boundary condition capturing model for multi-phase incompressible flows; Caiden et al. [27] applied the GFM to two-phase flows including separate regions for compressible and incompressible fluids (also, see [62] for a monolithic coupling of incompressible flow to compressible flow as opposed to the partitioned coupling of [27]); Nguyen et al. [63] simulated incompressible flames using the GFM; Gibou et al. [64] used the GFM for the multi-phase incompressible Navier-Stokes equations with phase change (also, see [65]); Fedkiw [66] introduced the coupling of an Eulerian fluid calculation to a Lagrangian solid calculation using the GFM. An interested reader may also refer to [25] for additional details of the applications mentioned above. Finally, additional discussions of applications of the GFM are given in various papers, including GFM for front tracking methods for simulating compressible multi-phase flows [67-69], crystallization [70, 71], atomization [72], and other recent applications [52].

Modifications to the GFM have been proposed to accommodate two-phase flows, including flows where one fluid is significantly stiffer than the other (see for instance [27], [66], and [25]). Koren et al. [73] introduced a variation of the GFM to address pressure oscillations near the interface in two-fluid flows with arbitrarily large density ratios. Arienti et al. [74] proposed a modified version termed the ghost-fluid Eulerian Lagrangian (GLE) method to couple Eulerian compressible flow with a Lagrangian solver for fluid-solid interactions (authors of [75] describe the procedure to define ghost values in the explicit coupling of fluids with solids). Nguyen et al. [76] introduced a fully conservative version of the GFM

that applied to the inviscid reactive Euler equations. The above discussion is but a short list of the modifications to the GFM and its applications. In the next section, we discuss a separate class of the GFM defined using multi-medium Riemann problems (MMRPs) at the interface, which has been shown [36, 40] to be more robust and accurate than the original GFM (OGFM) approach.

3.2 Ghost Fluid Methods based on multi-medium Riemann solvers

Using multi-medium Riemann solvers at the interface to couple fluids governed by different equations of state has been shown to result in high-quality numerical solutions at or near the interface ([77], [78]). To extend this idea to the GFM, Liu et al. [36] proposed a modified GFM (MGFM), where approximate Riemann solvers were used to obtain more accurate values for the ghost cells with lower conservation errors (also, see [38, 79, 80] for a discussion of the applications of the MGFM, and [40] for a description of the accuracy and conservation errors associated with GFMs for MMRPs). Liu et al. [18] further developed the MGFM idea to simulate compressible fluids coupled to deformable structures in the presence of cavitation in fluids. Also, Hu and Khoo [37] proposed a numerical method called I-GFM, where the ghost values were obtained by real and ghost interactions (see [69] for the application of the I-GFM in primary breakup of a liquid jet and [81] for a proposed modified I-GFM). Wang et al. [38] proposed a real GFM (RGFM) approach to extend the capabilities of the MGFM and suggested a novel algorithm for the advection of the LS function. Xu et al. [39] proposed the so-called practical GFM (PGFM) for compressible multi-medium flows. Sambasivan and Udaykumar [32] implemented the RGFM approach to apply isobaric fix and to populate ghost cells in multi-dimensions, by using normal vectors obtained from LS functions to construct MMRPs in the normal

direction to the interface. In [82], the authors provided an extension of the approach of [32] by coupling with local mesh refinement and for shock-induced vaporization of droplets [83].

The GFM framework is summarized in the *GFM theorem*, which was introduced in [40] as a lemma and states that a two-fluid Riemann problem can be split into two component single-fluid Riemann problems (or "GFM Riemann problems" as labelled by [40]). Figures 3.5 and 3.6 show the two-fluid Riemann problem ($RP(U_L, U_R)$) with the solution, and the GFM Riemann problems ($RP(U_L, U_{*L})$ and $RP(U_{*R}, U_R)$), respectively. Each GFM Riemann problem has a real and a ghost state, where the real state is obtained directly from the original two-fluid Riemann problem (U_L or U_R), and the ghost state from its solution (U_{*L} or U_{*R}). From the GFM theorem, the superposition of the real-fluid solutions to the component GFM Riemann problems (figure 3.6) correspond to the solution of the original two-fluid Riemann problem (figure 3.5).
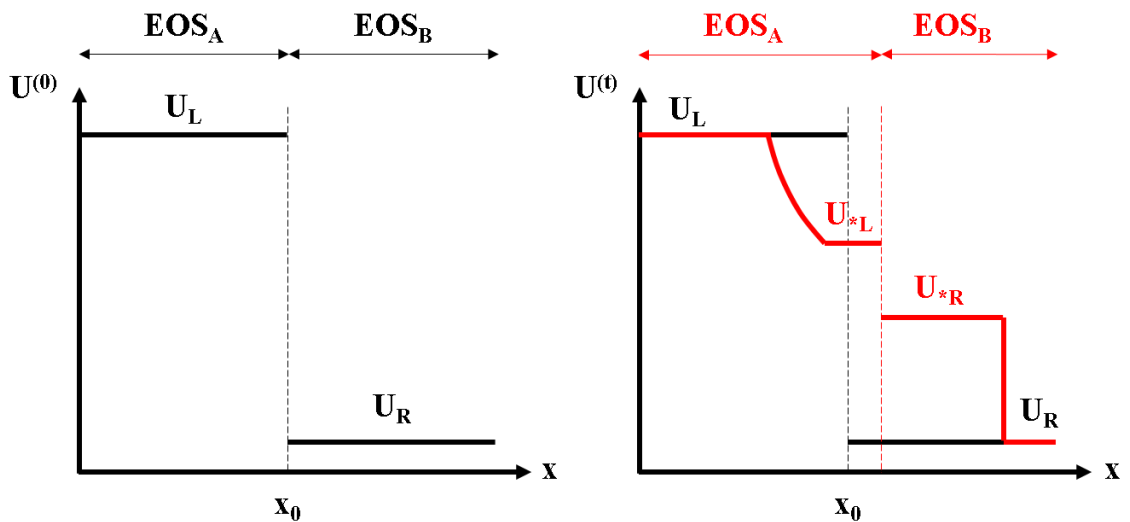
Figure 3.5. Two-fluid Riemann problem and its solution.

In contrast to the OGFM [26] approach, where flux conservation at the interface is the basis for defining ghost fluids, MMRP-based GFMs rely on the solution of the MMRP at the interface to populate the ghost cells. These GFMs result in more accurate solutions for problems with strong shocks and high-density ratios [36, 38].
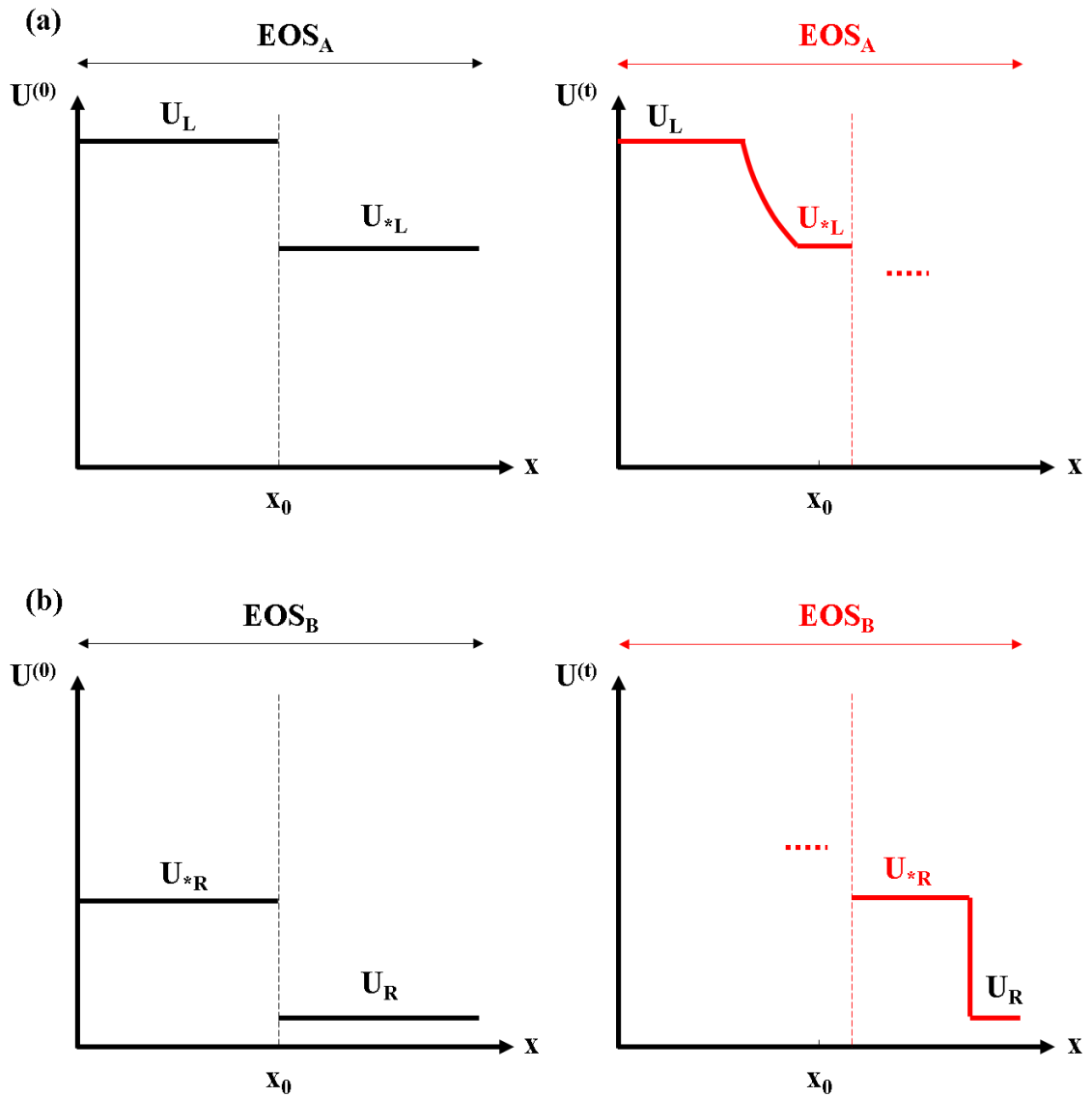
Figure 3.6. GFM Riemann problems and their solutions for (a) Fluid A, and (b) Fluid B.

3.3 The Efficient Ghost Fluid Method and overheating treatment

In § 3.1, the GFM method was introduced along with a discussion of the advantages of the approach. A central feature of such methods is the ability to resolve a sharp interface, by removing unphysical diffusion at or near such interfaces. However, the GFM and its variants can still result in some diffusion on both sides of the interface. This phenomenon, as discussed in § 3.1, is termed overheating, and has been shown [4] to result from numerical inaccuracies that stem from applying single-medium numerical schemes to (Fluid A+Ghost Fluid A) and (Fluid B+Ghost Fluid B). In this section, we propose an improvement to the GFM approach that addresses overheating, resulting in highly accurate solutions near the interface.

First, a brief review of approaches to address overheating in the GFM is provided here. In [26], the authors proposed to extrapolate entropy instead of density (as shown in figure 3.7 (based on figure 1 from [26])), since entropy contains less overheating errors [35]. The extrapolated entropy can then be used to obtain density values at the ghost points to form the vector of conserved variables. In addition, these authors suggested an isentropic fix (shown in figure 3.8 (based on figure 2 from [26])) where rather than extrapolating the entropy of the cells next to the interface, the entropy value is obtained by extrapolating from cells further afield. For example, in figure 3.8 where the interface is between cells 'i' and '$i + 1$', the entropy of cell '$i - 1$' is used to fix the entropy of cell 'i' and to populate the ghost cells. For multi-dimensional problems, the corresponding correction is applied in the interface normal direction [26], by extrapolating entropies from points $1.5\Delta x$ away from the interface.
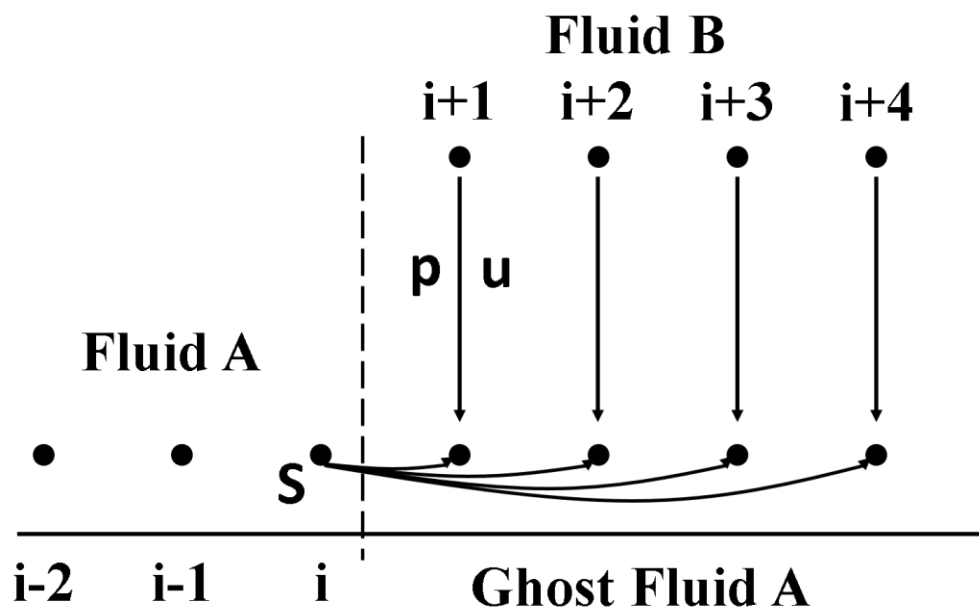
Figure 3.7. Using entropy to define ghost fluids. Figure is based on figure 1 from [26].
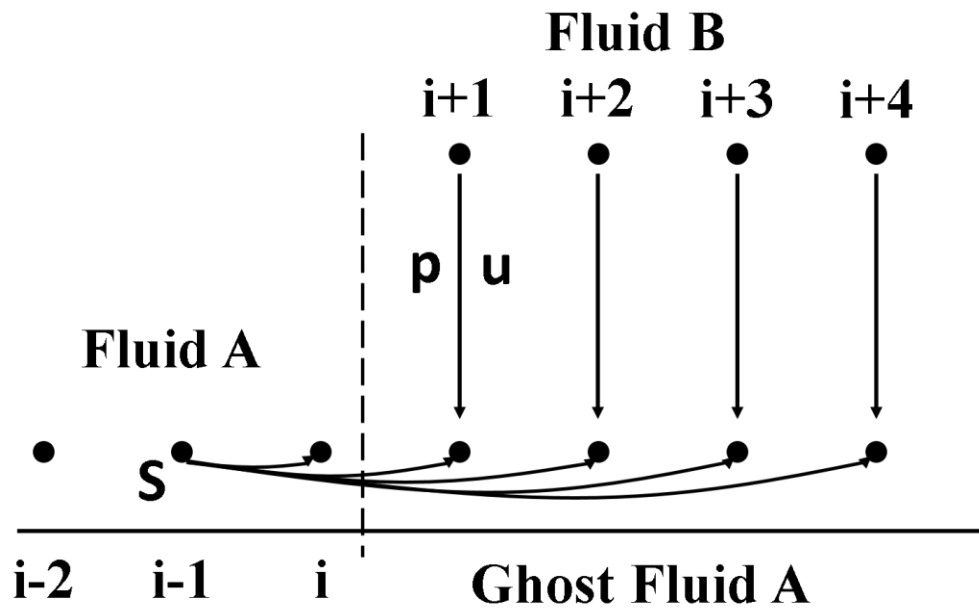
Figure 3.8. Isentropic fix. Figure is based on figure 2 from [26].

In versions of the GFM [36, 38, 39] which rely on the solution to MMRPs at the interface, it has been shown that using the cell values from '$i - 1$' and '$i + 2$' as initial conditions for the MMRP resulted in an improvement in reducing overheating (when compared with the choice of using data from 'i' and '$i + 1$'). In [36], the entropy values of the real cells next to the interface were fixed by the solution to the MMRP, which showed further improvement in the overheating error. In the RGFM approach [38], real cells next to the interface were corrected for density, velocity, and pressure values, rather than for entropy. This resulted in more accurate imposition of boundary conditions at the interface, resulting in improved behavior in shock impedance matching problems [36] by reducing the amplitude of the erroneous numerical wavelets reflecting off the interface.

Note that in the GFM approach, the description of the entropy field is closely related to overheating. Since entropy (or density) of fluids cannot pass through the interface, and is instead transported by the linearly degenerate field, the entropy jump across the interface should remain sharp without diffusion. However, numerical inaccuracies associated with single-medium solvers give rise to the diffusion of entropy near the interface, thus causing overheating. In isentropic fix, the entropy of the cells next to the interface are obtained from cells further afield which are less afflicted by the numerical diffusion.

As an alternative to the approach outlined in figure 3.8, the isentropic fix can also be implemented using more sophisticated methods such as those outlined in the PGFM [39] approach where the isentropic relation is applied between a reference cell located far from the interface and the cell next to the interface. This approach is depicted in figure 3.9 (based on figure 10 from [39]), which shows the reference values of entropy (density) can be used

to fix these variables at points near the interface. By comparing the pressures, one decides

to use either isentropic or shock relation for density:

$$\rho_j = \begin{cases} \rho_r \left(\dfrac{p_j + p_{\infty L}}{p_r + p_{\infty L}}\right)^{\frac{1}{\gamma_L}}, & p_j \leq p_r \ (rare) \\[2em] \rho_r \left[\dfrac{(\gamma_L - 1)(p_r + p_{\infty L}) + (\gamma_L + 1)(p_j + p_{\infty L})}{(\gamma_L - 1)(p_j + p_{\infty L}) + (\gamma_L + 1)(p_r + p_{\infty L})}\right], & p_j > p_r \ (shock) \end{cases} \tag{3.2}$$

where j denotes the points where the density fix is to be applied.
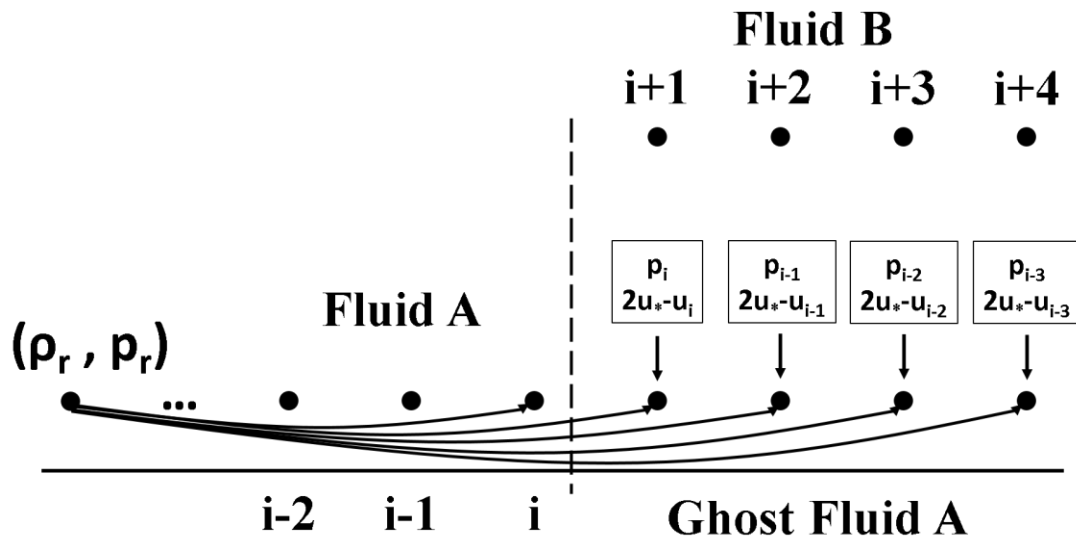
Figure 3.9. Isentropic fix and population of ghost cells in the PGFM. Figure is based on figure 10 from [39].

Unfortunately, the methods discussed above, while reducing overheating errors, are not

able to completely eliminate them. Since overheating stems from numerical inaccuracies

associated with single-medium solvers, coupling an isentropic fix with such solvers will

still result in diffusion (albeit to a smaller extent) near the interface.

We observe the key to eliminating overheating is that the isentropic fix (or any similar

numerical remedy) must be applied *after* the solution from the single-medium solver is

obtained. A GFM version can be constructed from this insight, and we propose such an approach be termed the *Efficient* Ghost Fluid Method or *EGFM*.

The EGFM approach: The GFM Theorem, (§ 3.2), states that a two-fluid Riemann problem can be split into two different GFM Riemann problems. We show that this theorem can be exploited to establish the EGFM approach, modifying the numerical solution near the interface to eliminate overheating errors. Considering the two-fluid Riemann problem in figure 3.5, note that in the immediate aftermath of the removal of the diaphragm between Fluids A and B, two new values (U_{*L} and U_{*R}) emerge in the solution. As depicted in figure 3.10, the fluids then start to interact with these new values, i.e. in Fluid A, U_{*L} and U_L form a leftward rarefaction wave and in Fluid B, U_{*R} and U_R form a rightward shock wave. The jump between Fluids A and B, however, moves by the linearly degenerate field which is the interface velocity. The above process occurs in the exact same manner in figure 3.6: U_{*L} emerges in figure 3.6(a) and interacts with U_L to form the rarefaction wave, while U_{*R} emerges in figure 3.6(b) and interacts with U_R to form the shock wave.
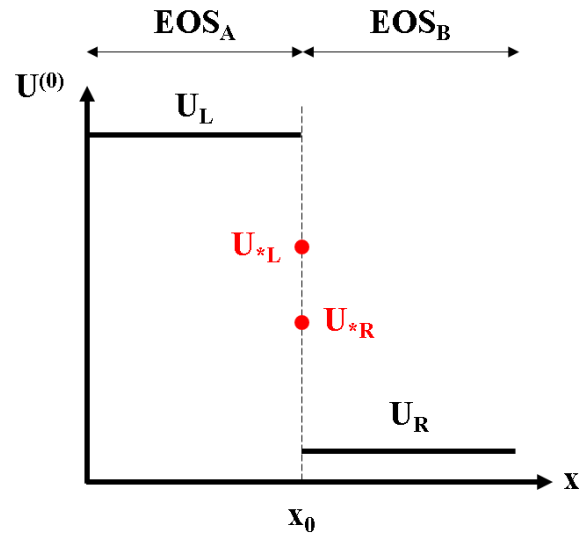
Figure 3.10. The solution status immediately after removing the diaphragm between Fluids A and B.

Based on the above discussion regarding figure 3.6, we now describe the EGFM approach to address the overheating errors. In figure 3.11(a), the Riemann problem $RP(U_L, U_{*L})$ is solved numerically over one time step Δt using a single-medium solver with EOS$_A$. Note that this changes the value of some cells near the initial interface marked by red symbols.
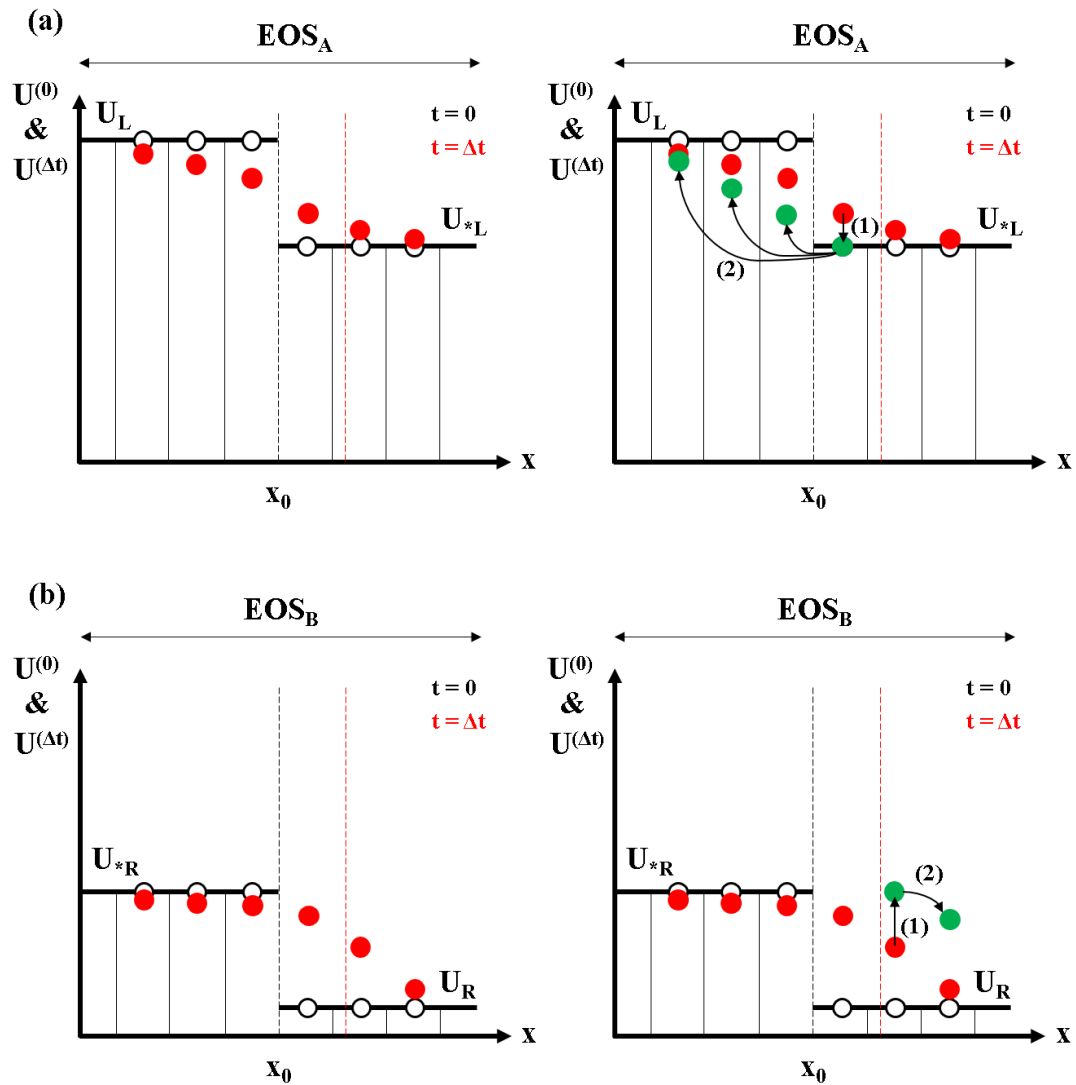
Figure 3.11. The EGFM implementation for (a) Fluid A, and (b) Fluid B.

Thus, the red symbols show the solution affected by the numerical diffusion from applying the single-medium solver. The EGFM approach fixes these values in two steps (the fixed values are shown in green): (1) The value of the cell next to the new interface (at $t = \Delta t$) is changed to U_{*L}, which is the exact solution immediately following the removal of the diaphragm (see figure 3.10); (2) Similar to [39], the isentropic relation is then applied between the cell next to the new interface and the cells away from it. Note that in this

second step, the isentropic relation is applied not only to densities (as in [39]), but also to velocities. These relations are as follows:

$$\rho = \rho_{*L}\left(\frac{p + p_{\infty L}}{p_{*L} + p_{\infty L}}\right)^{\frac{1}{\gamma_L}} \tag{3.3}$$

$$u = u_* + \frac{2}{\gamma_L - 1}(a_{*L} - a) \tag{3.4}$$

We found that applying just the density fix (as suggested in [39]) was insufficient in addressing overheating, without the accompanying velocity fix. The above steps are depicted with the labels (1) and (2) in figure 3.11(a).

The corresponding fix applied to Fluid B is shown in figure 3.11(b), where the Riemann problem $RP(U_{*R}, U_R)$ is solved numerically for one time step with EOS$_B$. Similar to figure 3.11(a), the red symbols are associated with the numerical inaccuracies. As before, the fix (shown as red → green) is applied in two steps: (1) The value of the cell next to the new interface (at $t = \Delta t$) is changed to U$_{*R}$, which is the exact solution immediately following the removal of the diaphragm; (2) Similar to [39], the shock relation is then applied between the cell next to the new interface and the cells further from it. Again, this is implemented for both density and velocity using:

$$\rho = \rho_{*R}\left[\frac{(\gamma_R - 1)(p_{*R} + p_{\infty R}) + (\gamma_R + 1)(p + p_{\infty R})}{(\gamma_R - 1)(p + p_{\infty R}) + (\gamma_R + 1)(p_{*R} + p_{\infty R})}\right] \tag{3.5}$$

$$u = u_* + a\left(\frac{\rho}{\rho_{*R}} - 1\right)\sqrt{\frac{\gamma_R + 1}{2\gamma_R}\frac{(p_{*R} + p_{\infty R})}{(p + p_{\infty R})} + \frac{\gamma_R - 1}{2\gamma_R}} \tag{3.6}$$

A few observations are in order:

1. While step (1) of the fix is implemented only for a single point, step (2) may be applied to one or more points. Choosing a wider stencil for step (2) was found to improve the solution, and we have used a stencil of 10 points for our simulations.

2. Figure 3.11 shows the EGFM applied in conjunction with the forward Euler method for time discretization. For multi-step approaches such as the TVD-RK method, the EGFM corrections must be implemented over each sub step, i.e. the level set is first advanced for the sub step, followed by application of the corrections using the above protocol.

3. Figure 3.11 depicts a case with a rarefaction and a shock wave to the left and right sides of the interface, and in step (2), the isentropic or the shock relation would be applied accordingly. In practice, the wave types are not available a priori and will have to be determined from the pressure values.

4. Equations (3.3) and (3.4) correspond to a left rarefaction. For a left shock, the following relations are applied in step (2):

$$\rho = \rho_{*L} \left[\frac{(\gamma_L - 1)(p_{*L} + p_{\infty L}) + (\gamma_L + 1)(p + p_{\infty L})}{(\gamma_L - 1)(p + p_{\infty L}) + (\gamma_L + 1)(p_{*L} + p_{\infty L})} \right] \tag{3.7}$$

$$u = u_* - a \left(\frac{\rho}{\rho_{*L}} - 1 \right) \sqrt{\frac{\gamma_L + 1}{2\gamma_L} \frac{p_{*L} + p_{\infty L}}{p + p_{\infty L}} + \frac{\gamma_L - 1}{2\gamma_L}} \tag{3.8}$$

Similarly, for a right rarefaction, the following equations apply:

$$\rho = \rho_{*R} \left(\frac{p + p_{\infty R}}{p_{*R} + p_{\infty R}} \right)^{\frac{1}{\gamma_R}} \tag{3.9}$$

$$u = u_* + \frac{2}{\gamma_R - 1}(a - a_{*R}) \tag{3.10}$$

5. If the Riemann problem shown in figure 3.5 represents a shock wave, i.e. $EOS_A = EOS_B$ and U_L and U_R are the post- and pre-shock values of the shock, respectively, the above method cannot remove the numerical inaccuracies and will result in a diffuse shock. Consequently, the EGFM implementation must be modified to be compatible with problems involving shock waves (including single shock and shock-interface interactions). This is described in the next section.

We conclude this section by summarizing all the steps involved in advancing the solution by one time step using the EGFM algorithm:

1. Assuming the interface is located between cells i and $i + 1$, solve the MMRP $RP(U_i, U_{i+1})$ to obtain U_{*L} and U_{*R} (ρ_{*L}, ρ_{*R}, u_*, p_{*L}, p_{*R}).

2. Use U_{*L} to define Ghost Fluid A at cells $i + 1, i + 2, i + 3$, etc.

3. Use U_{*R} to define Ghost Fluid B at cells $i, i - 1, i - 2$, etc.

4. Apply an appropriate reconstruction, e.g. WENO to (Fluid A+Ghost Fluid A) and (Fluid B+Ghost Fluid B) separately.

5. Find fluxes and advance the solution for (Fluid A+Ghost Fluid A) and (Fluid B+Ghost Fluid B) separately over a sub step of a multi-step time integration method (e.g. TVD-RK).

6. Using u_*, advance the level set over the same sub step.

7. Fix the value of the cell next to the new interface and located in Fluid A to U_{*L} and the value of the cell next to the new interface and located in Fluid B to U_{*R}.

8. Apply either the isentropic or the shock relation between the cells next to the new interface and the cells further from it to fix densities and velocities.

9. Form the actual domain according to the fixed Fluid A and Fluid B.

Note that the novelty of the EGFM lies in steps 7 and 8.

3.4 Application of the Efficient Ghost Fluid Method to shock-interface interactions

A framework for applying the EGFM to shock-interface interactions is presented in this section. Consider the problem configuration in figure 7 in which a shock is located at x_{S0} and a material interface is at x_0. Osher and Fedkiw [25] suggested using two separate LS fields (for the shock and the interface) to ensure the shock front and the interface remain sharp. The approach presented in this section in which the EGFM is extended achieves the same objective, while requiring the use of only one LS field to track the interface.

To implement the EGFM for shock-interface problems, care must be taken to ensure the incident shock remains sharp as it impinges on the interface. Initially sharp shock fronts that have diffused numerically in time are not compatible with the EGFM approach in that such shocks already contain numerical errors. In the following, we discuss an implementation of the EGFM in which the shock is maintained as a sharp front.

In figure 3.12, the initial boundary between U_S and U_L, i.e. post- and pre-shock states, moves to the right with shock speed given by the Rankine-Hugoniot jump conditions:

$$S = \frac{\rho_S u_S - \rho_L u_L}{\rho_S - \rho_L} \tag{3.11}$$

The diffuse shock is fixed by first computing the location of the shock according to $x_{S1} = x_{S0} + S\Delta t$, where Δt is obtained from the CFL condition. If a cell center is located behind (in front of) x_{S1}, its value is changed to the post-shock U_S (pre-shock U_L) value. Our numerical simulations show that fixing only two cells on either side of the shock is sufficient to completely remove diffusion. The explained fix holds for shocks traveling in the negative x-direction as well.
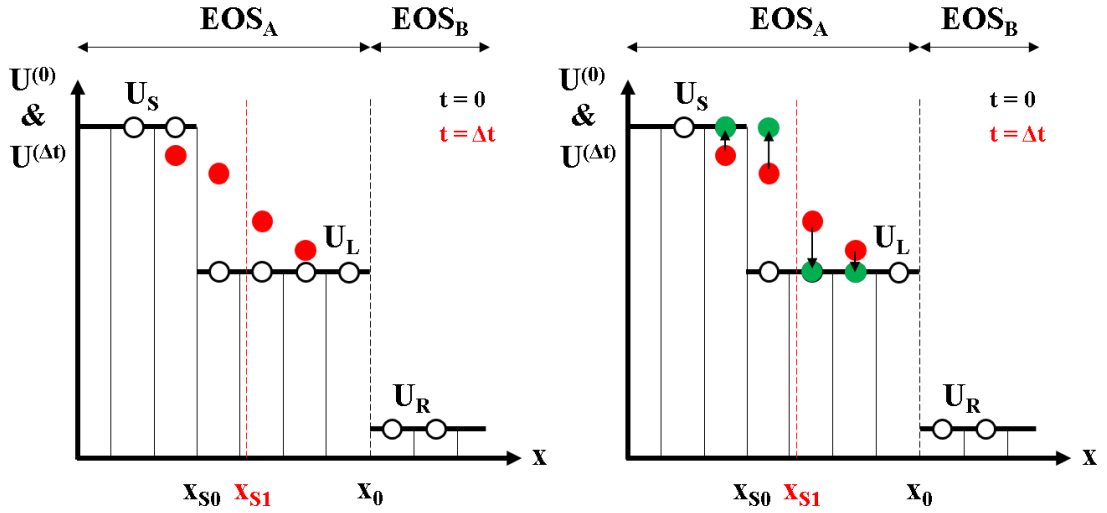
Figure 3.12. Shock-interface interaction on a 1D computational domain.

We thus propose computing sharp shock-interface interactions using the following approach: If $x_{S1} < x_0 - 0.5\Delta x$, the above shock treatment must be applied. However, if $x_0 - 0.5\Delta x \leq x_{S1}$ (the shock has reached the interface), only the two cells behind the shock are fixed, followed by applying the EGFM for the rest of the simulation. Note that for this condition, the EGFM will handle $RP(U_S, U_R)$. For shock-interface interactions with a leftward shock impacting the interface from the right, the above procedure is changed by comparing x_{S1} with $x_0 + 0.5\Delta x$, while the EGFM solves $RP(U_L, U_S)$.

3.5 Modeling surface tension at fluid interfaces using the Ghost Fluid Method

In this work, we use the GFM approach for simulating surface tension effects in compressible two-phase flow problems. In the GFM framework, surface tension is added to the interface through modifying the interfacial boundary conditions to account for the pressure jump induced by surface tension. This can be carried out by utilizing the OGFM approach (see for example [27]) or by adding surface tension to pressure terms in multi-

medium Riemann solvers in MMRP-based GFMs (see [84] for instance). Both approaches are implemented in IMPACT.

In addition to the OGFM, the MMRP-based GFM of Sambasivan and UdayKumar [32] is implemented in IMPACT. As discussed in § 3.2, this approach is broadly similar to the RGFM [38] implementation, but constructs the MMRP at the interface using normal vectors and bilinear interpolations. This approach results in a more accurate Riemann problem at the interface, since the MMRP is solved in the interface normal direction. Moreover, the algorithm of [32] reduces overheating errors by taking for the left and right states of the MMRP, cell values that are $1.5\Delta x$ away from the interface. An interested reader is referred to [82] and [83].

Figure 3.13 (based on figure 2 from [32]) demonstrates the above approach applied to Fluids A and B separated by a sharp interface. In the figure, Point P is located next to the interface, $\widehat{N}$ is the normal vector at P, point I is on the interface ($\phi = 0$), while points A and B are located in Fluids A and B respectively, each at a distance $1.5\Delta x$ from the $\phi = 0$ surface. From the value of ϕ at P, the location of I is obtained using $(x_I, y_I) = (x_P, y_P) - \phi_P \widehat{N}$. Similarly, the coordinates of A and B are found from (x_I, y_I) using $(x_A, y_A) = (x_I, y_I) - (1.5\Delta x)\widehat{N}$ and $(x_B, y_B) = (x_I, y_I) + (1.5\Delta x)\widehat{N}$, respectively.
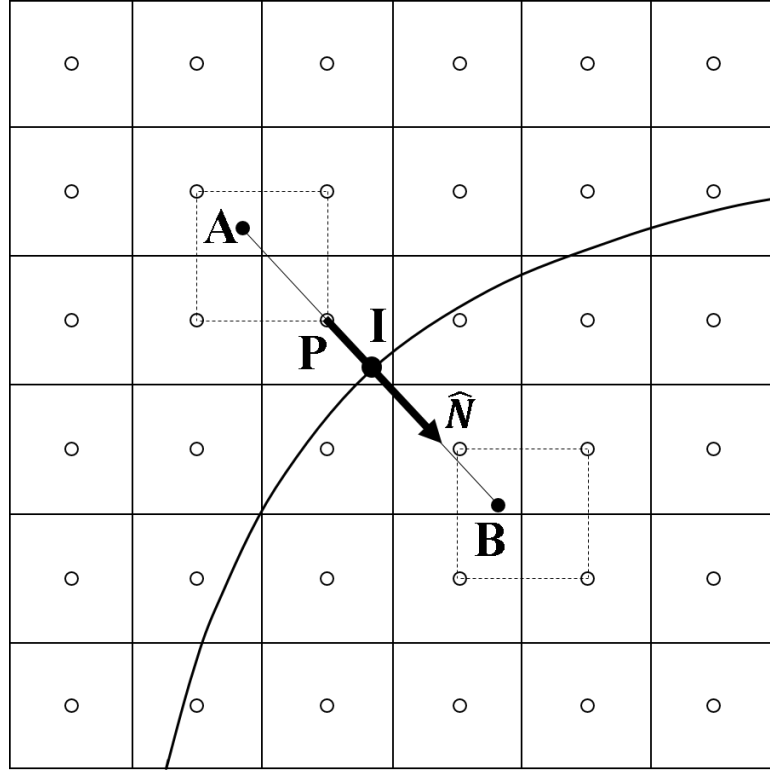
Figure 3.13. The method of [32] to formulate the MMRP at the interface. Figure is based on figure 2 from [32].

Thus, the density, normal velocity V_N, tangential velocity V_T, and pressure at points A and B can be obtained from the surrounding four cell centers using bilinear interpolation. Then the multi-medium Riemann problem $RP(U_L, U_R)$ can be defined using (ρ_A, V_{NA}, p_A) and (ρ_B, V_{NB}, p_B) as the left and right states respectively. We follow the approach of [32], and use the exact Riemann solver to solve $RP(U_L, U_R)$, so that accuracy is maintained and strong shock-interface interactions are captured with fidelity. The solution U$_{*L}$ and U$_{*R}$ (ρ_{*L}, ρ_{*R}, u$_*$, p$_{*L}$, p$_{*R}$) to $RP(U_L, U_R)$ is utilized to apply an isobaric fix to point P by setting $(\rho_P, V_{NP}, p_P) = (\rho_{*L}, u_*, p_{*L})$ [32, 38], while the tangential velocity V_{TP} remains unchanged. Once this algorithm has been conducted for all cells in Fluid A which are located next to the interface, eq. (3.1) is used with a '+' sign to extrapolate

$(\rho_P, V_{NP}, V_{TP}, p_P)$ to the other side of the interface to populate Ghost Fluid A. The isobaric fix is repeated for Fluid B, which for a sample point P is given by: $(\rho_P, V_{NP}, p_P) = (\rho_{*R}, u_*, p_{*R})$, while the tangential velocity V_{TP} remains unchanged again. As before, once this algorithm has been applied to cells in Fluid B located next to the interface, eq. (3.1) is used with a '−' sign to extrapolate $(\rho_P, V_{NP}, V_{TP}, p_P)$ to the other side of the interface to populate Ghost Fluid B. Note that we have used two different pressures p_{*L} and p_{*R} in the solution of the MMRP, to account for surface tension effects according to $[p] = p_{*R} - p_{*L} = \sigma\kappa$, where $[p]$ is the pressure jump across the interface, σ is the surface tension coefficient, and κ is the interface curvature computed from eq. (2.44).

Exact multi-medium Riemann solver with surface tension:

Detailed descriptions of exact multi-medium Riemann solvers are given in [32, 40, 83-85], while multi-medium Riemann solvers adapted to account for surface tension effects are presented in [84, 86]. In IMPACT, we follow [32] where pressure is solved using the equation below:

$$f_L(p, W_L) + f_R(p, W_R) + u_R - u_L = 0 , \qquad (3.12)$$

where $W_L = (\rho_L, u_L, p_L)$ and $W_R = (\rho_R, u_R, p_R)$ are the left and right states of the MMRP, respectively, and functions f_L and f_R are defined as follows:

$$f_L(p, W_L) = \begin{cases} (p_{*L} - p_L)\sqrt{\dfrac{\dfrac{2}{(\gamma_A + 1)\rho_L}}{p_{*L} + p_{\infty A} + \dfrac{\gamma_A - 1}{\gamma_A + 1}(p_L + p_{\infty A})}} & (shock) \\[4ex] \dfrac{2}{\gamma_A - 1}\sqrt{\dfrac{\gamma_A(p_L + p_{\infty A})}{\rho_L}}\left[\left(\dfrac{p_{*L} + p_{\infty A}}{p_L + p_{\infty A}}\right)^{\frac{\gamma_A - 1}{2\gamma_A}} - 1\right] & (rare) \end{cases} \qquad (3.13)$$

$$f_R(p, \boldsymbol{W}_R) = \begin{cases} (p_{*R} - p_R) \sqrt{\dfrac{\dfrac{2}{(\gamma_B + 1)\rho_R}}{p_{*R} + p_{\infty B} + \dfrac{\gamma_B - 1}{\gamma_B + 1}(p_R + p_{\infty B})}} & (shock) \\[3em] \dfrac{2}{\gamma_B - 1} \sqrt{\dfrac{\gamma_B(p_R + p_{\infty B})}{\rho_R}} \left[\left(\dfrac{p_{*R} + p_{\infty B}}{p_R + p_{\infty B}} \right)^{\frac{\gamma_B - 1}{2\gamma_B}} - 1 \right] & (rare) \end{cases}$$

$$(3.14)$$

In eqs. (3.13) – (3.14), the relations for shock and rarefaction are selected based on the pressures (see [32] for details). We use the Newton-Raphson method to solve eq. (3.12) for either p_{*L} or p_{*R}, and impose the condition $p_{*R} - p_{*L} = \sigma\kappa$. Then, eqs. (3.3)-(3.10) are used to find ρ_{*L}, ρ_{*R}, and u_*.

At the end of this chapter, we summarize the numerical capabilities of IMPACT in table 3.1 showing the major numerical methods used for the flow solver, the LS function, and the interface coupling. We have referred to the equation(s) required to be solved in each module along with the numerical methods used and the references in the literature.

Table 3.1. A summary of the numerical capabilities of IMPACT.

Module	Equation	Method	References
Flux calculator	(2.16)	Roe solver	[41] [43]
EOS	(2.6)	Stiff gas	-
Cell reconstruction	(2.22) (2.23)	WENO5	[45] [46]
LS equation	(2.40)	WENO5	[26] [50] [51]
Reinitialization	(2.41)	WENO5	[26] [50] [51] [53]
Extrapolation	(3.1)	1st-order ENO	[26] [87]
Time discretization	(2.45) (2.46)	TVD-RK3	[55]
Interface coupling	-	OGFM RGFM EGFM	[26] [27] [32] [38]

CHAPTER 4: RESULTS AND DISCUSSION

This chapter describes simulations performed to validate the numerical methods in IMPACT, and is organized as follows: In § 4.1, 1D single- and multi-medium Riemann problems and various shock-interface interaction simulations are summarized; 2D problems are presented and discussed in § 4.2; in § 4.3, results from IMPACT simulations of the shock-driven RMI are presented with corresponding analyses; finally, the ability of IMPACT to simulate flow problems in which surface tension effects are significant is demonstrated in § 4.4 including RMI with surface tension. All test problems in this chapter are summarized in table 4.1.

4.1 1D test cases

In this section, we solve various 1D Riemann problems analytically as well as numerically with IMPACT using OGFM, RGFM, and EGFM. Unless mentioned otherwise, the simulations were performed in a computational domain of length unity with 200 cells and $CFL = 0.2$. In order to highlight the capabilities of the EGFM, we include the numerical results from EGFM step (1) for the first two tests (*4.1.1* and *4.1.2*) as well.

4.1.1. Sod shock tube problem [41, 88]: This problem is initialized in a domain filled with air ($\gamma = 1.4$) with a discontinuity at $x_0 = 0.5$, and the following initial conditions:

$$\boldsymbol{W}_L = (\rho_L, u_L, p_L) = (1,0,1),$$

$$\boldsymbol{W}_R = (\rho_R, u_R, p_R) = (0.125,0,0.1).$$

Table 4.1. 1D and 2D problems used to validate IMPACT.

	Problem	Section	Reference
	Sod shock tube	*4.1.1*	[41, 88]
	Shock impedance matching	*4.1.2*	[36, 38, 39]
	Shock tube with strong pressure jump 1	*4.1.3*	[41]
	Shock tube with strong pressure jump 2	*4.1.4*	[41]
	Collision of two strong shocks	*4.1.5*	[41]
	Multi-component shock tube problem 1	*4.1.6*	[89]
1D	*Multi-component shock tube problem 2*	*4.1.7*	[36]
	Multi-component shock tube problem 3	*4.1.8*	[36, 38]
	Strong shock impacting on a gas-gas interface (heavy → light)	*4.1.9*	[26]
	Strong shock impacting on a gas-gas interface (light → heavy)	*4.1.10*	[26]
	Strong shock impacting on a gas-water interface (heavy → light)	*4.1.11*	[58]
	Sod shock tube problem with prescribed pressure jump	*4.4.1*	[84]
	Underwater explosion of an air bubble	*4.2.1*	[58]
	Strong shock impacting on an air cavity (heavy → light)	*4.2.2*	[90]
	Shock-bubble interaction (light → heavy)	*4.2.3*	-
2D	Richtmyer-Meshkov Instability	4.3	-
	Oscillating drop	*4.4.2*	[31, 86]
	Shock-bubble interaction under surface tension effects (light → heavy)	*4.4.3*	-
	Richtmyer-Meshkov instability under the effect of surface tension	*4.4.4*	-

The solution to the problem consists of a left rarefaction, a contact discontinuity, and a right shock, and is shown for $t = 0.25$ in figure 4.1. In this figure, we have implemented only step (1) of the fix in the EGFM.

As seen in figure 4.1, the OGFM, RGFM, and EGFM step (1) work equally accurately to capture the wave structure of the solution. For a closer comparison of the three methods near the contact discontinuity, we have plotted in figure 4.2 the density distributions over a narrow band of cells next to the middle wave. This figure shows that the EGFM step (1) gives the exact values for the cells immediately to the left and to the right of the wave, while the OGFM and RGFM are susceptible to overheating. For cells away from the interface, all three methods result in numerical inaccuracies.
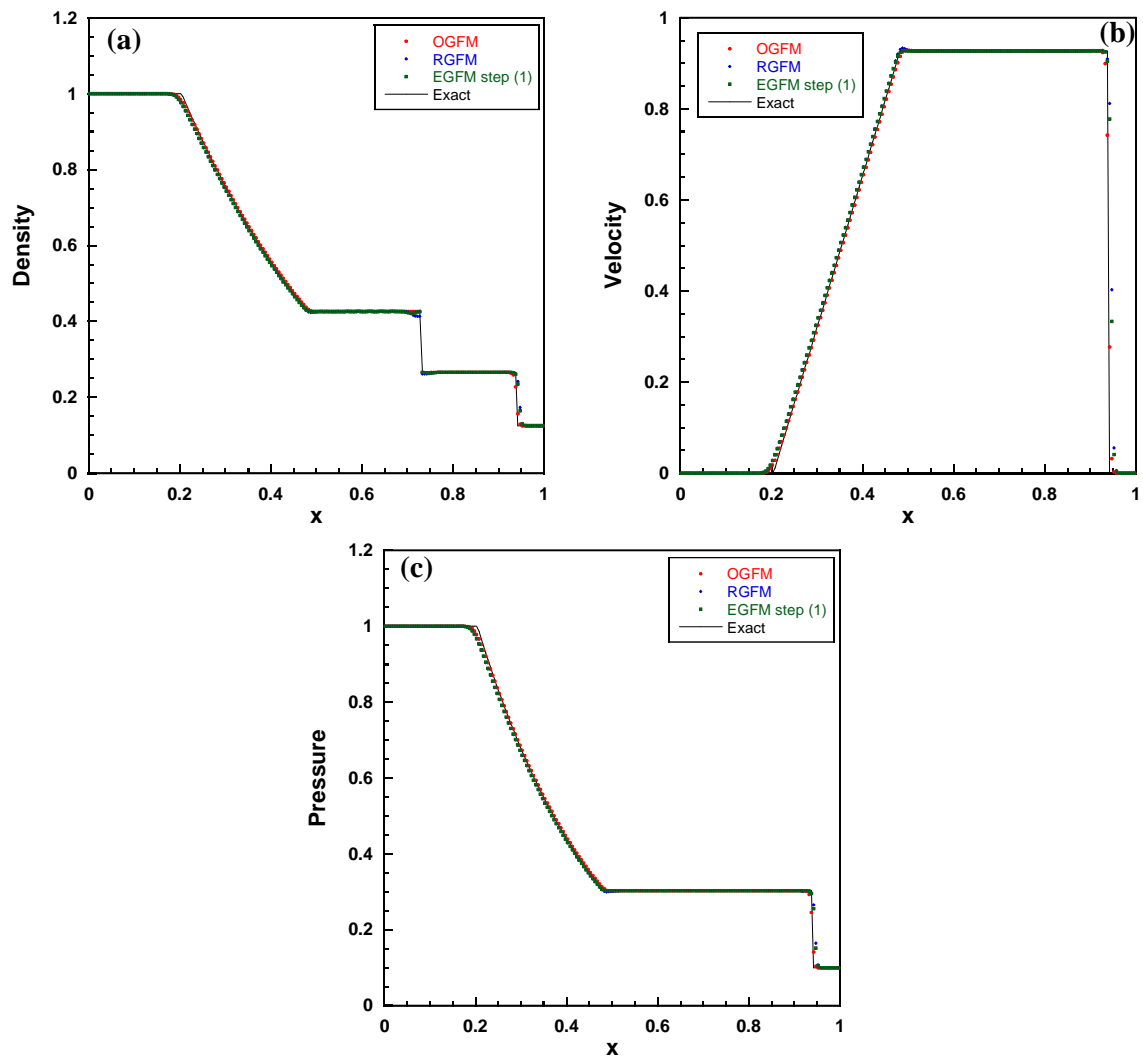
Figure 4.1. (a) Density, (b) velocity, and (c) pressure profiles for the Sod shock tube problem.
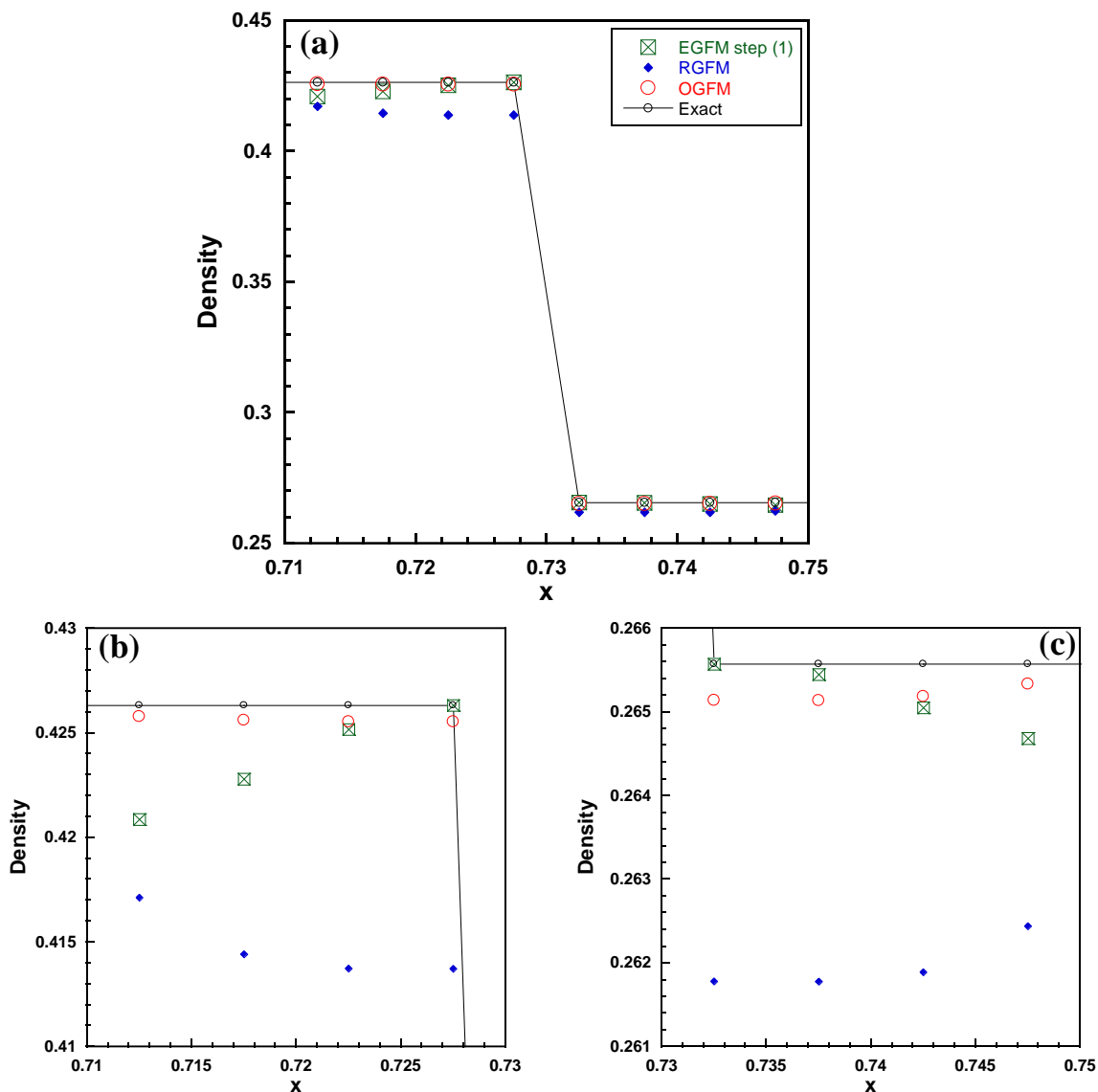
Figure 4.2. (a) Density distribution near the contact discontinuity. Density values on the (b) left and (c) right sides of the wave. The density values of the two cells immediately next to the contact wave show the agreement of the results from the EGFM step (1) with the exact solution.

We also compare the accuracy with which the three methods capture the corners of the rarefaction by plotting in figure 4.3 (a), (b), and (c) the density, velocity, and pressure distributions across the corner located at $x = 0.482$. As seen in figure 4.3, the OGFM and

RGFM underpredict the analytical values of density and pressure (undershoots), and overpredict the velocity values (overshoots). In contrast, the EGFM (step (1)) captures the analytical solution with accuracy. This demonstrates the EGFM approach in which the numerical solution is rectified according to the local behavior of the corresponding analytical solution, provides the most accurate solution for the Sod shock tube problem.
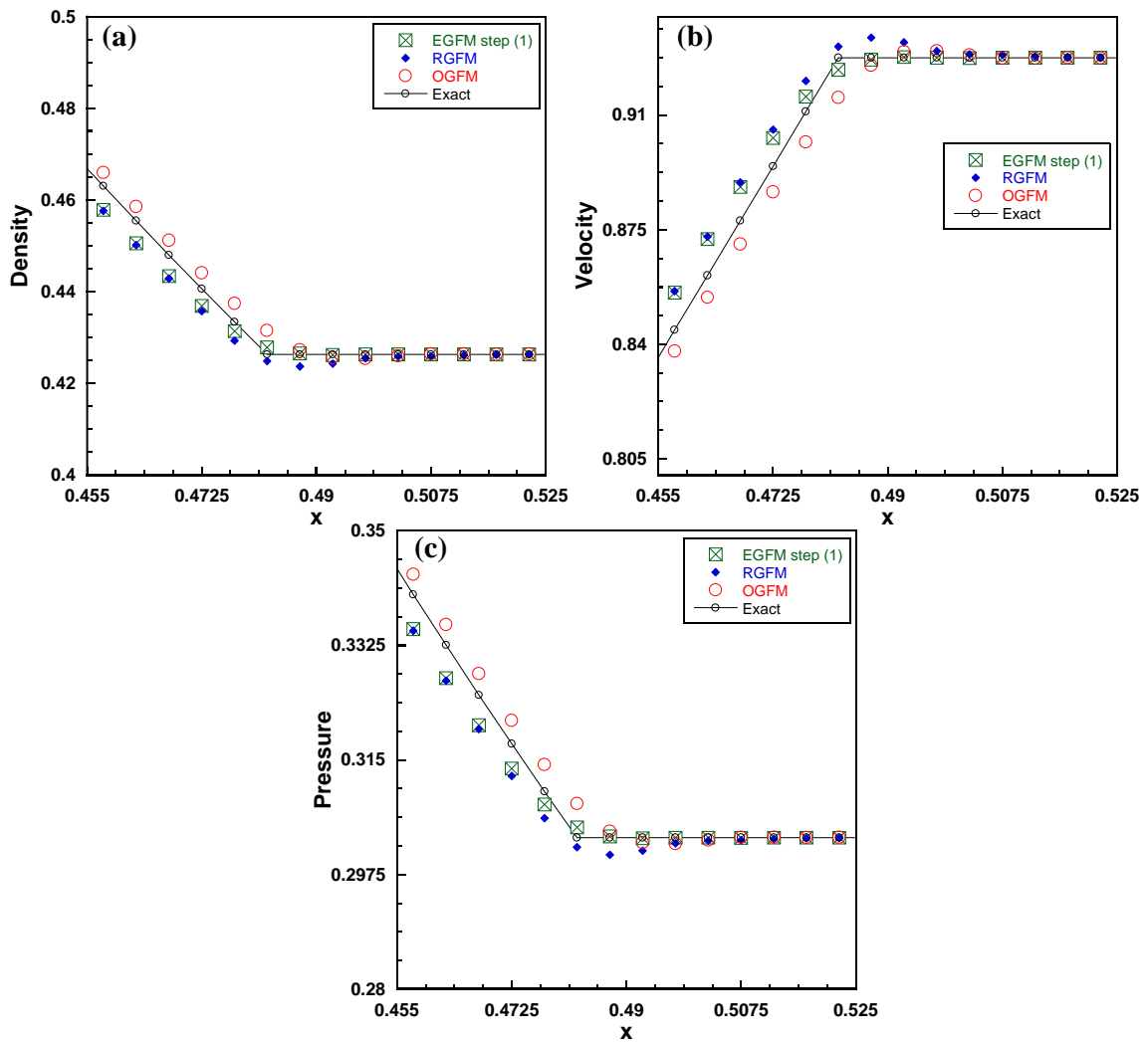
Figure 4.3. (a) Density, (b) velocity, and (c) pressure distributions across the rarefaction corner. The EGFM (step (1)) rectifies the incorrect troughs associated with the OGFM as well as the mild overshoots and undershoots associated with the RGFM.

In figures 4.1-4.3, we demonstrated that by applying step (1) of the EGFM, an improved numerical solution can be obtained to the Sod shock tube problem, compared to the OGFM and RGFM. However, density values at the cells away from the contact wave in figure 4.2 contain numerical inaccuracies, and require the application of step (2) to be corrected. In figures 4.4 and 4.5, the EGFM was applied in its entirety, resulting in solutions that are in excellent agreement with the analytical solution for each of the reported quantities.
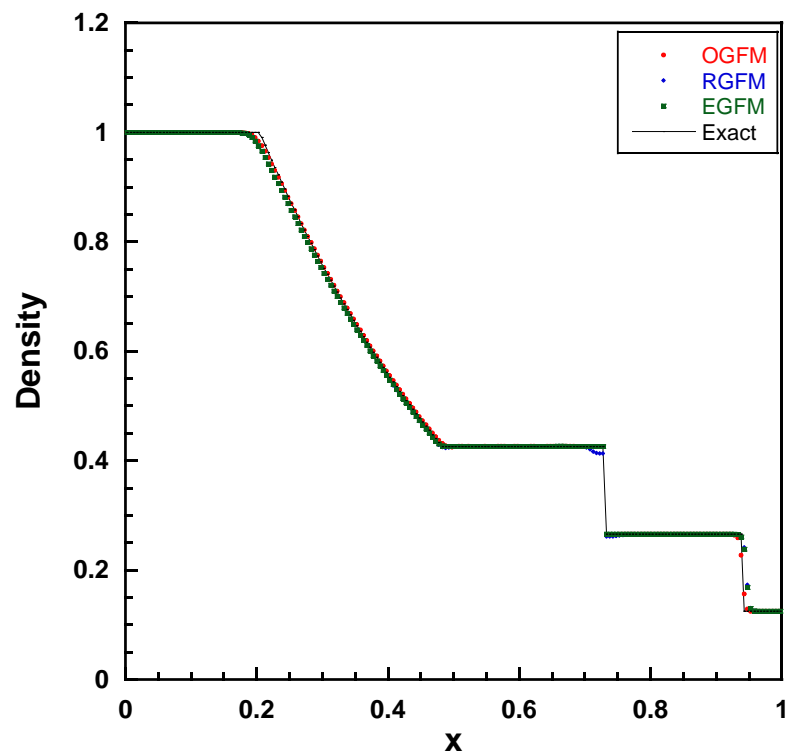
Figure 4.4. Density profile for problem *4.1.1*. The EGFM has been applied in its entirety.
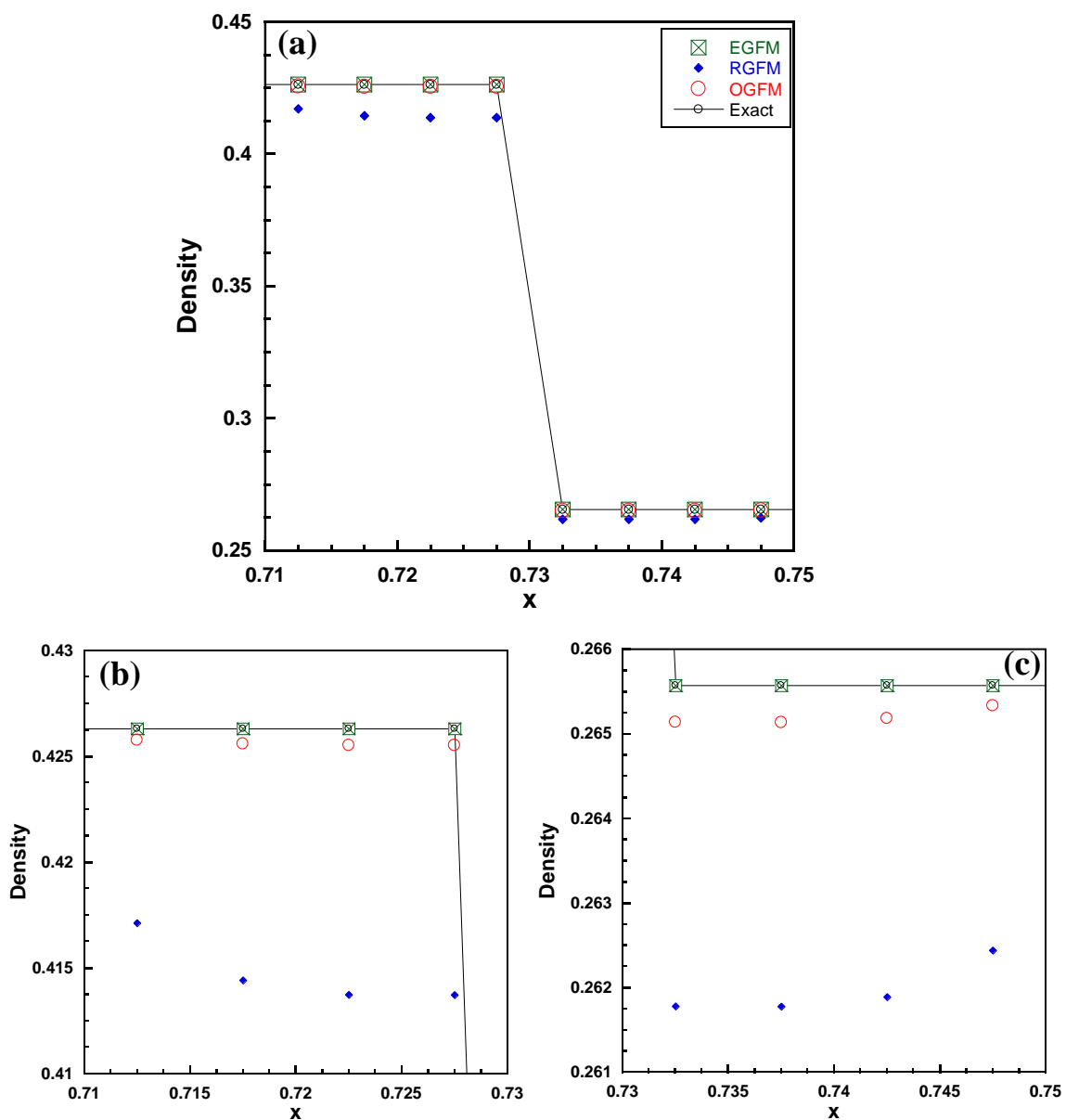
Figure 4.5 (a) Density values near the contact discontinuity. Density values on the (b) left and (c) right sides of the wave. The EGFM completely removes overheating from the numerical solution.

4.1.2. Shock impedance matching problem [36, 38, 39]: In this specifically designed Riemann problem, the solution comprises a shock wave to the right of the original discontinuity, while no wave forms on the left. The domain is filled with two gases ($\gamma_L = 1.667$ and $\gamma_R = 1.2$) with a discontinuity at $x_0 = 0.2$, and the following initial condition:

$$W_L = (\rho_L, u_L, p_L) = (3.174819866, 9.434397965, 100),$$

$$W_R = (\rho_R, u_R, p_R) = (1, 0, 1).$$

The solution obtained at $t = 0.06$ is shown in figure 4.6, where the problem was solved using OGFM, RGFM and step (1) of the fix in the EGFM.
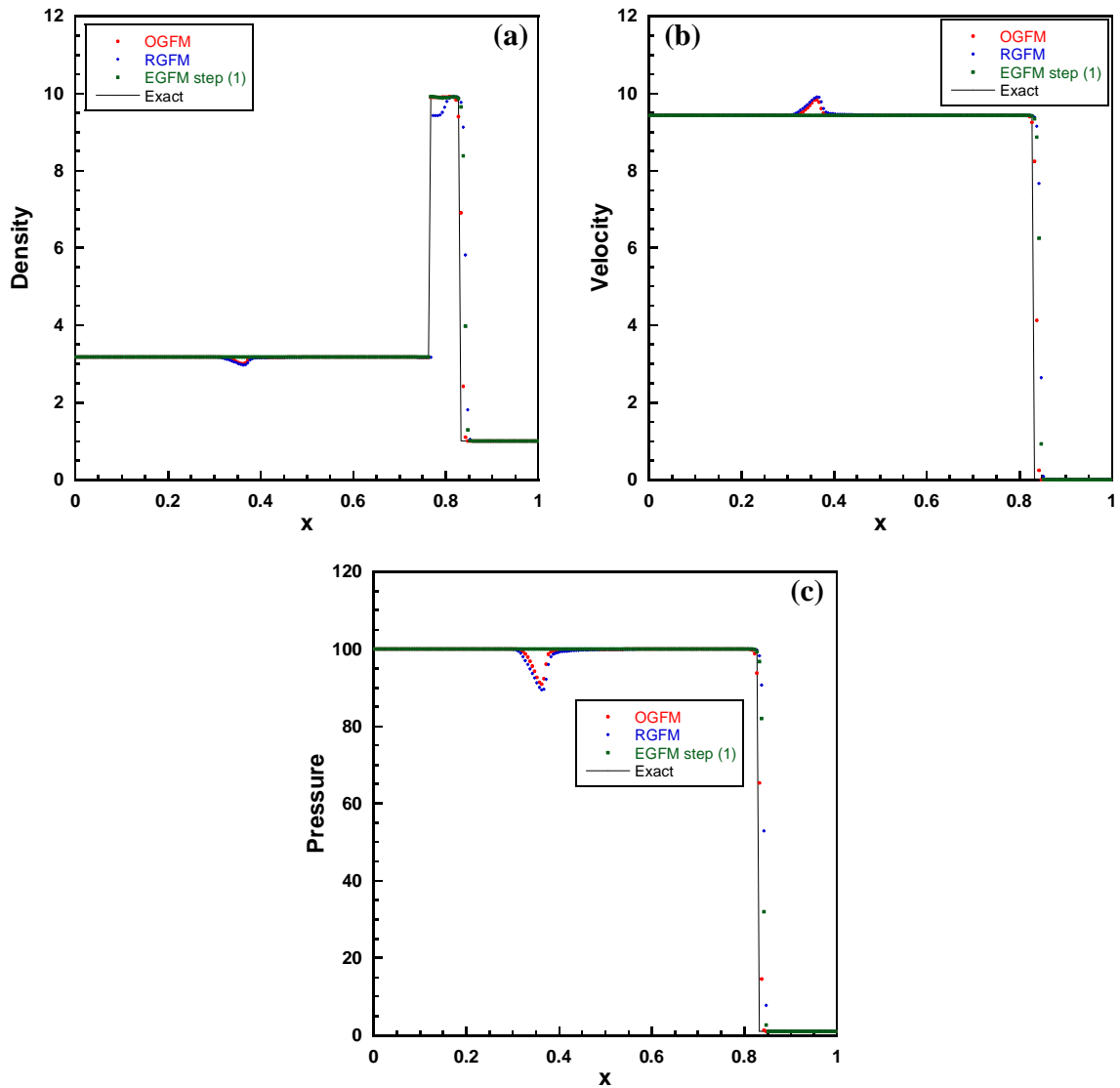
Figure 4.6. (a) Density, (b) velocity, and (c) pressure distributions in the shock impedance matching problem. The inability of the OGFM and RGFM to apply the correct boundary condition at the interface results in the spurious reflection.

As seen in figure 4.6, even a partial implementation of the EGFM (step (1)) completely eliminates the unphysical reflecting wave to the left of the interface. This is shown in detail in figure 4.7, where the density, velocity, and pressure are plotted for $x \in [0.3, 0.4]$. Note that the OGFM and RGFM solutions contain numerical errors and spurious reflections,

since they apply approximate boundary conditions at the interface. The EGFM solution, however, exactly matches the analytical values, as the EGFM applies the exact interfacial boundary conditions following the GFM theorem in figures 3.6 and 3.10. Earlier efforts to simulate this problem include the MGFM [36], RGFM [38], and PGFM [39] approaches. In these earlier studies, the erroneous reflections observed in figure 4.6 were not completely removed, but mitigated in some instances.

Similarly, figure 4.8 shows the solution detail across the interface and demonstrates results from step (1) of the EGFM is in excellent agreement with the analytical solution for the cells immediately next to the interface, while the OGFM and RGFM suffer from overheating. In figure 4.8(a), the interface location computed using the RGFM is displaced one mesh cell away from the exact location. This stems from the approximate implementation in RGFM of the interfacial boundary conditions, giving rise to an approximate interface velocity advecting the LS function, and hence the slightly incorrect location of the interface. Note that although the RGFM (as well as the MGFM [36] and PGFM [39] approaches) is based on obtaining multi-medium Riemann solutions at the interface, the MMRP defined at the interface is based on the cell values already contaminated with overheating. The EGFM, however, fixes the cell values next to the interface (see figure 3.11), so that the initial condition for the MMRP is exact for the next time step/sub step. These issues are exacerbated for problems containing strong shocks (high pressure ratios), and are discussed later in this chapter.

To completely remove overheating and improve the global accuracy of the solution, step (2) of the EGFM was applied to the solution as well, and the results are plotted in figures

4.9 and 4.10. When the correction from step (2) is included, the EGFM solution matches exactly the analytical solution for all x.
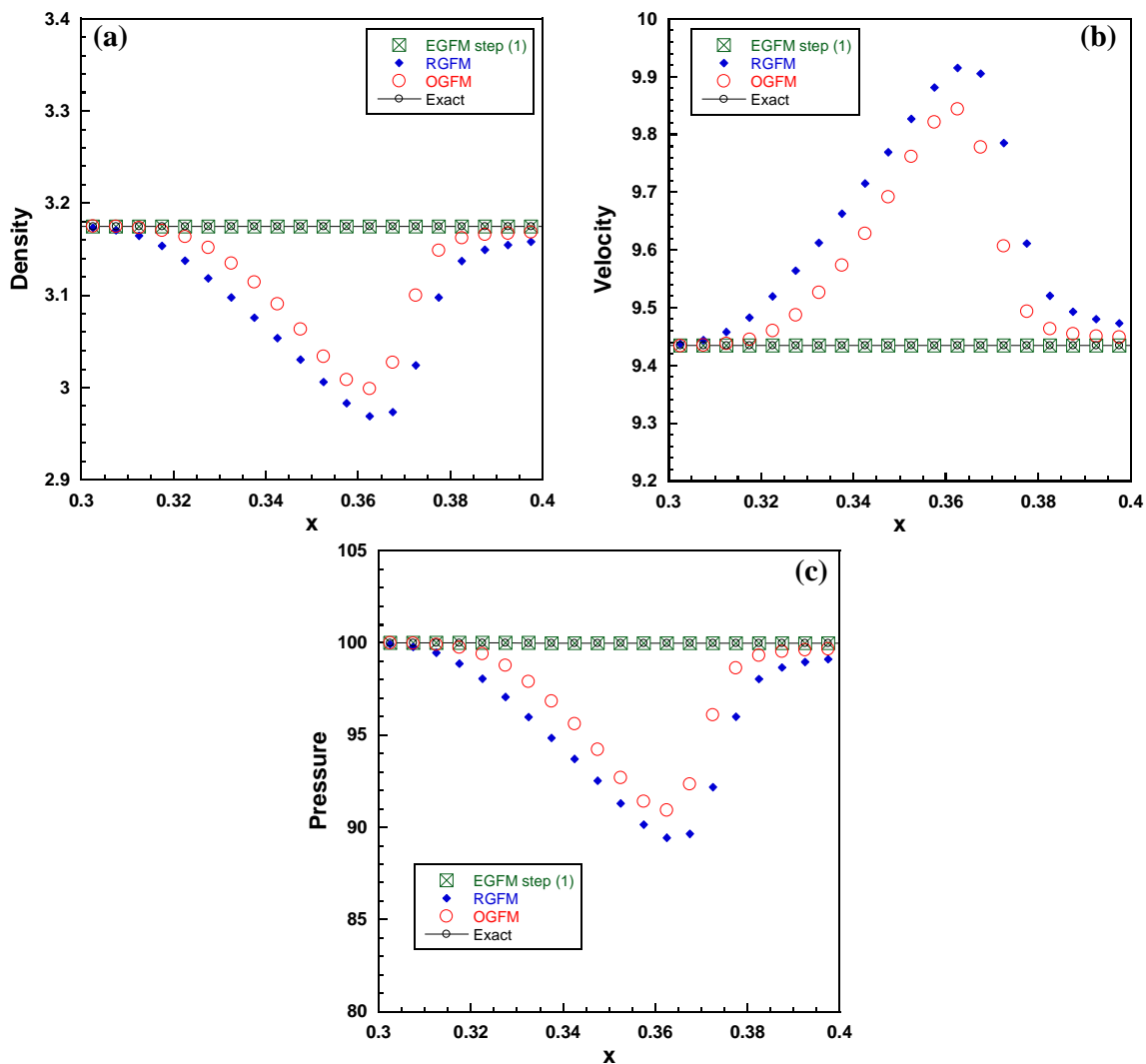
Figure 4.7. (a) Density, (b) velocity, and (c) pressure distributions highlighting the unphysical reflection wave in the shock impedance matching problem. The EGFM (step (1)) completely removes this reflection.
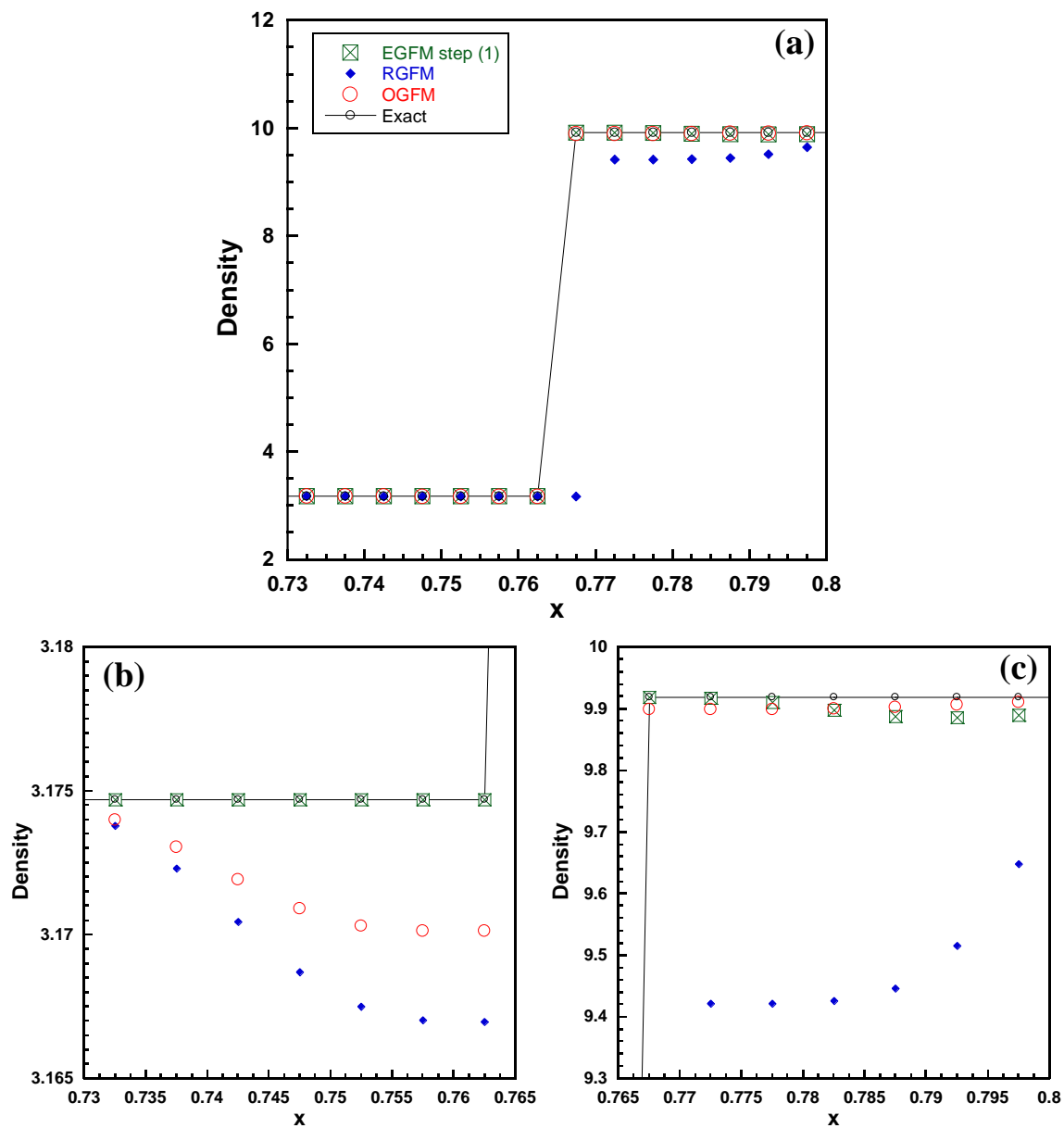
Figure 4.8. (a) Density distribution near the interface. Density values on the (b) left and (c) right of the interface. The density values of the two cells immediately next to the interface show the results from the EGFM step (1) in excellent agreement with the exact solution.
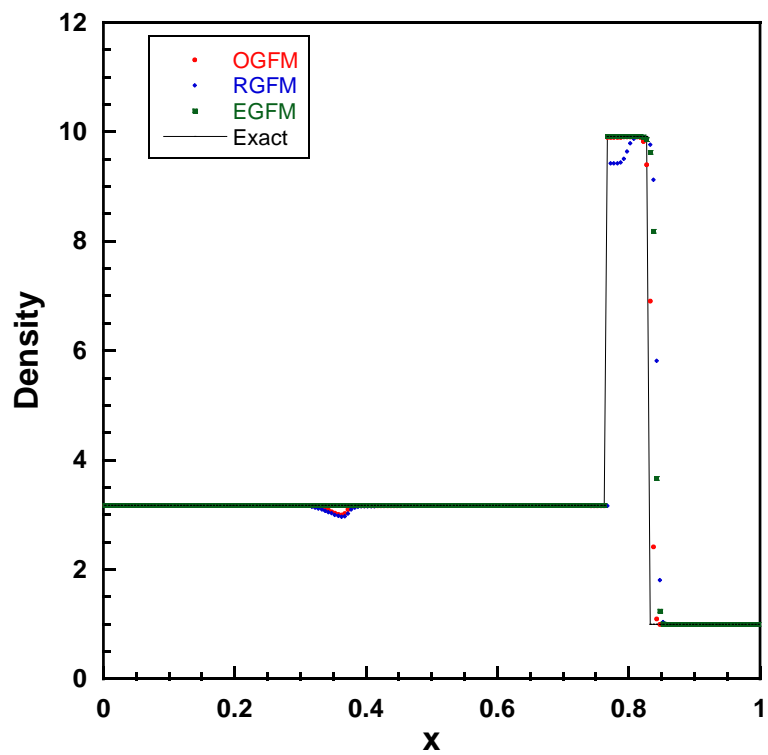
Figure 4.9. Density distributions for problem *4.1.2* where the EGFM has been implemented in its entirety.
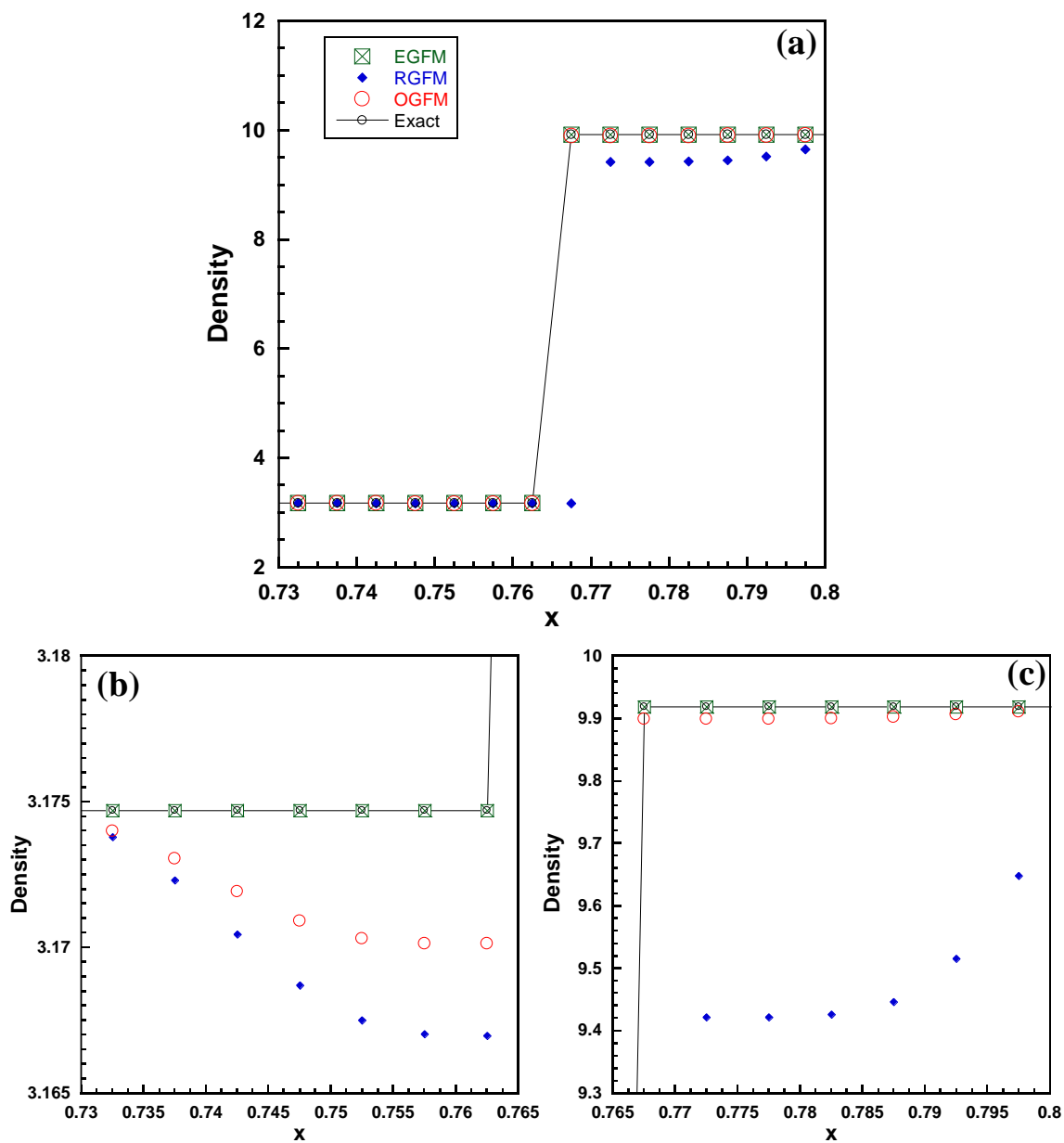
Figure 4.10. (a) Density distribution near the interface. Density values on the (b) left and (c) right of the interface. The EGFM removes overheating from the numerical values.

4.1.3. Shock tube with strong pressure jump 1 [41]: This is a shock tube problem where

the initial condition contains a strong pressure jump with a pressure ratio 1000:0.01. The

domain is filled with air ($\gamma = 1.4$) with an initial discontinuity located at $x_0 = 0.5$ with the following initial condition:

$$\boldsymbol{W}_L = (\rho_L, u_L, p_L) = (1,0,1000),$$

$$\boldsymbol{W}_R = (\rho_R, u_R, p_R) = (1,0,0.01).$$

The solution to this problem contains a left rarefaction and a right shock, and is shown for $t = 0.012$ in figure 4.11. Owing to the large magnitude of the initial pressure jump, the OGFM cannot resolve this problem, and the simulation breaks down following a few time steps. As pointed out by [36], this behavior of the OGFM results from inadequacy of the Rankine-Hugoniot jump conditions [25] to define the ghost fluids, which produces inaccurate solutions, especially for problems involving strong shocks, or high density ratios, or large disparities in the stiffness of the materials. Both the RGFM and EGFM, however, are able to provide solutions in agreement with the analytical solutions. Similar to the earlier test cases, the EGFM results in more accurate solution values, particularly near the contact discontinuity and around the corners of the rarefaction. Figure 4.12 is a detail of the density values near the interface from the EGFM and RGFM approaches and shows that in contrast to the RGFM, the EGFM is in very good agreement with the analytical values.
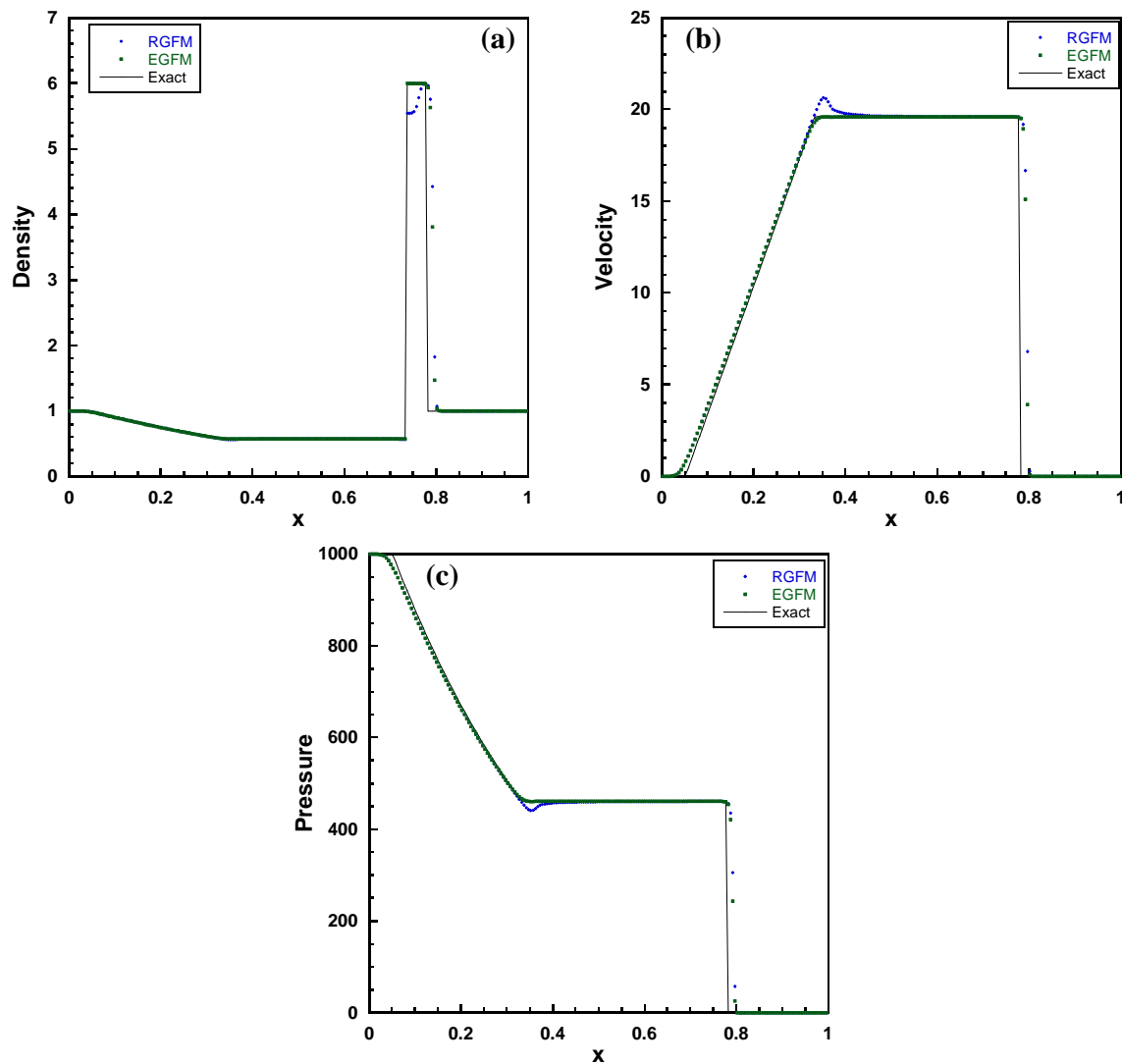
Figure 4.11. (a) Density, (b) velocity, and (c) pressure distributions in problem *4.1.3*. The OGFM is unable to resolve the wave structure associated with the strong pressure jump.
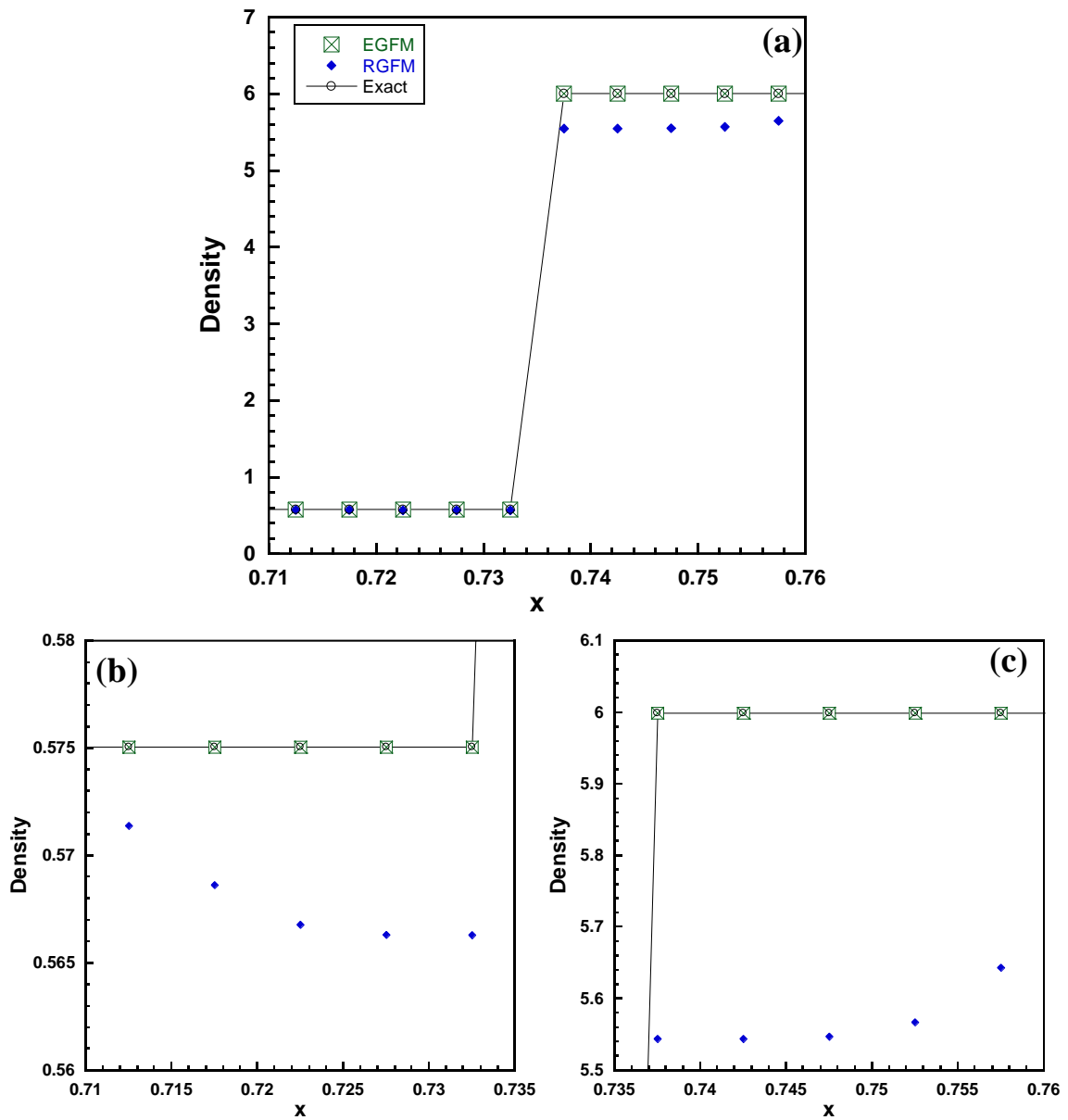
Figure 4.12. (a) Density values near the contact wave for problem *4.1.3*. Density values on the (b) left and (c) right sides of the wave. The EGFM results completely match the exact solution.

4.1.4. Shock tube with strong pressure jump 2 [41]: This Riemann problem is similar to

problem *4.1.3*, but with the initial high pressure region located to the right with a pressure

ratio of 100:0.01. The computational domain is filled with air ($\gamma = 1.4$) with the initial

discontinuity located at the center ($x_0 = 0.5$). The complete initial condition data is given by:

$$W_L = (\rho_L, u_L, p_L) = (1,0,0.01),$$

$$W_R = (\rho_R, u_R, p_R) = (1,0,100).$$

The solution thus consists of a left shock and a right rarefaction, and is shown for $t = 0.035$ in figure 4.13. Both the OGFM and RGFM lead to inaccurate solutions near the contact discontinuity and the rarefaction corner (see [36] and [40] where similar behavior has been reported for these versions of the GFM). In contrast, when the EGFM approach is applied, highly accurate numerical solutions are obtained. In particular, both the OGFM and RGFM approaches give rise to significant overshoots and undershoots for this demanding problem. In the appendix, an error and convergence analysis are performed for this problem, comparing the errors from the OGFM, RGFM, and EGFM. The details of the density field near the contact wave and the rarefaction corner are depicted in figures 4.14 and 4.15 respectively. In figure 4.14, the OGFM and RGFM approaches miscalculate the location of the contact wave by two and one cells respectively. As discussed in problem *4.1.2*, this behavior results from the approximations in capturing the interfacial boundary conditions. In the OGFM implementation, as pointed out in [26], the conservation of mass, momentum, and energy is relaxed at the contact discontinuity, giving rise to first-order convergence for the location of the wave. This could lead to incorrect values for the interface location, particularly for problems with strong shocks. In contrast, the EGFM predicts the correct contact wave location, as seen in figure 4.14.
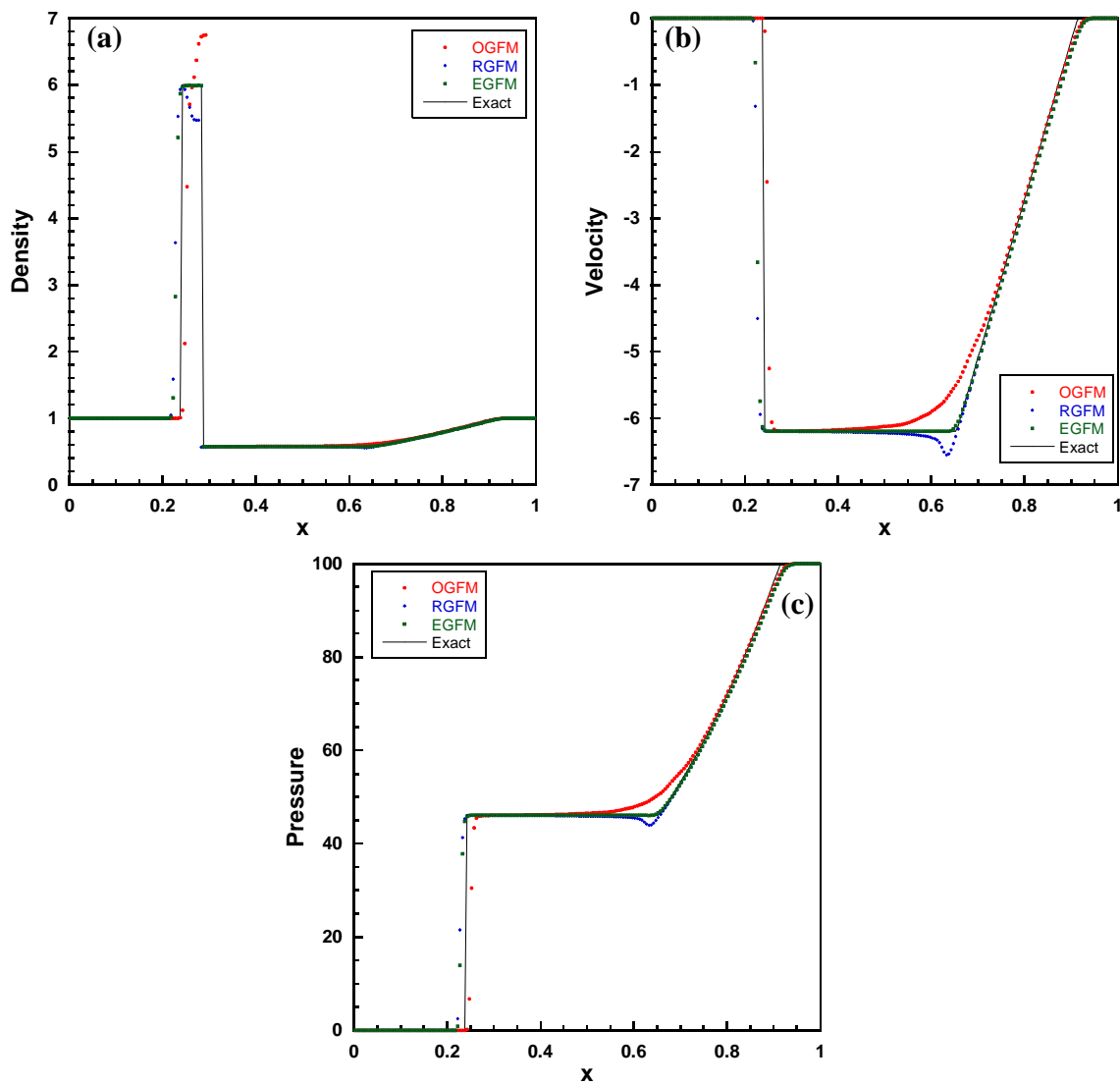
Figure 4.13. (a) Density, (b) velocity, and (c) pressure distributions in problem *4.1.4*. The results from the OGFM and RGFM exhibit noticeable errors.
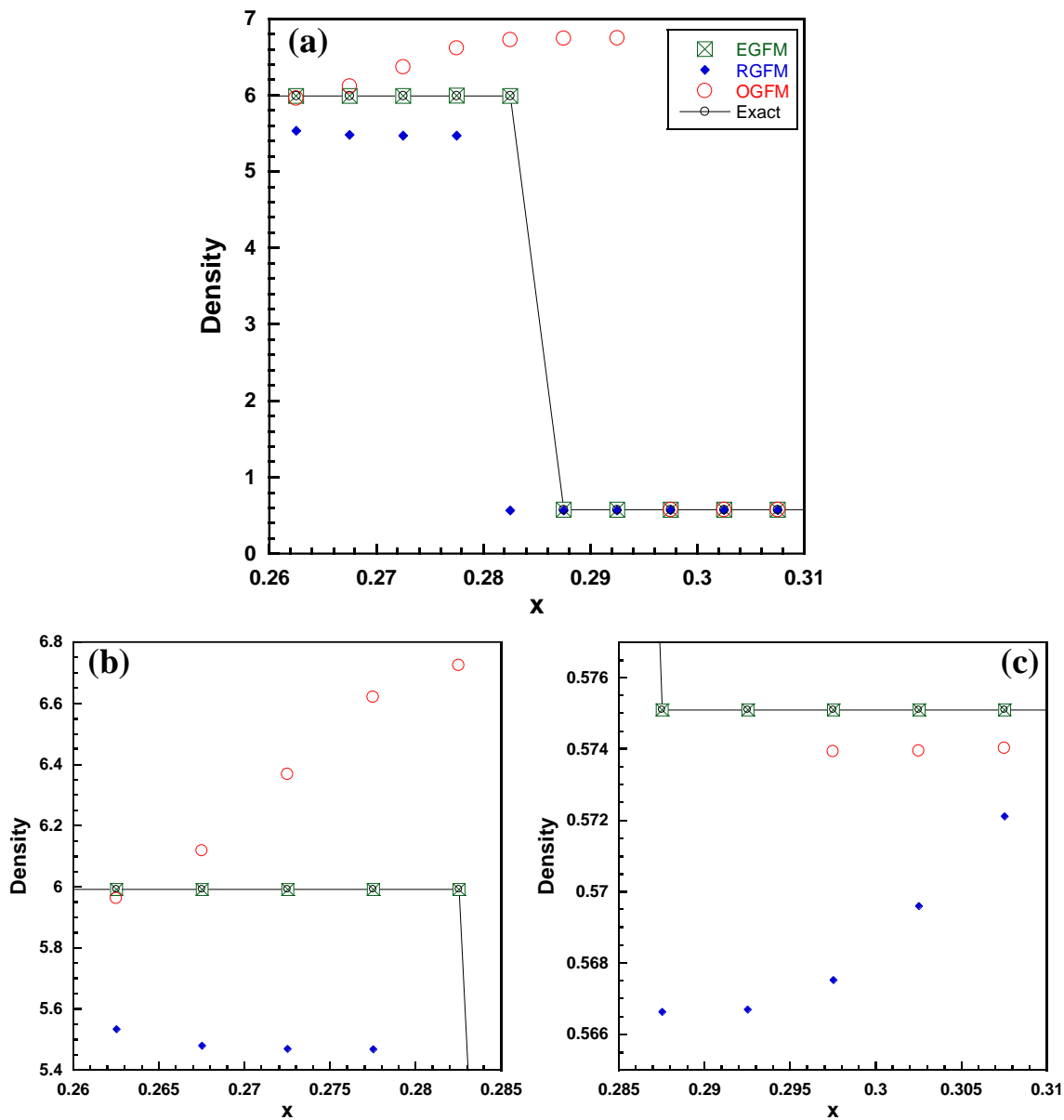
Figure 4.14. (a) Density values near the contact wave in problem *4.1.4*. Density values on the (b) left and (c) right sides of the wave. The EGFM results agree with the exact solution for both the density values and the location of the wave.
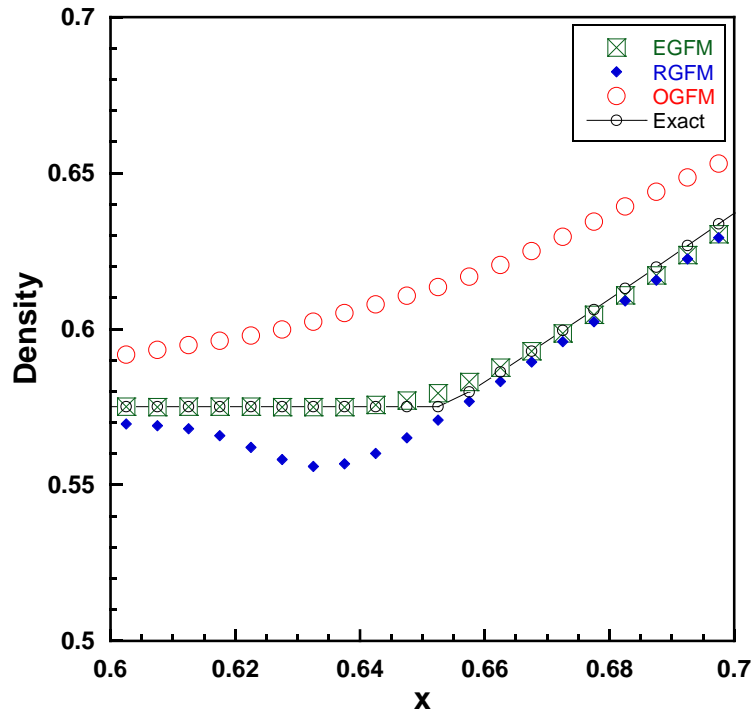
Figure 4.15. Density values near the rarefaction corner in problem *4.1.4*. The EGFM resolves the corner correctly.

4.1.5. Collision of two strong shocks [41]: In this Riemann problem, two strong shocks collide at the center ($x_0 = 0.5$) of a shock tube of length unity. These shocks are defined from problems *4.1.3* and *4.1.4*. The fluid is air ($\gamma = 1.4$), with the following initial data:

$$\boldsymbol{W}_L = (\rho_L, u_L, p_L) = (5.99924, 19.5975, 460.894),$$

$$\boldsymbol{W}_R = (\rho_R, u_R, p_R) = (5.99242, -6.19633, 46.0950).$$

The solution to this problem consists of two reflected shocks and a contact discontinuity, and is plotted for $t = 0.035$ in figure 4.16. As seen in the figure, density values from the OGFM and RGFM are highly inaccurate near the contact wave, while the EGFM values coincide with the exact solution (see figure 4.17). Moreover, we observe spurious

oscillations in pressures and velocities from the OGFM and RGFM, while the EGFM removes these oscillations completely near the interface (figure 4.17).
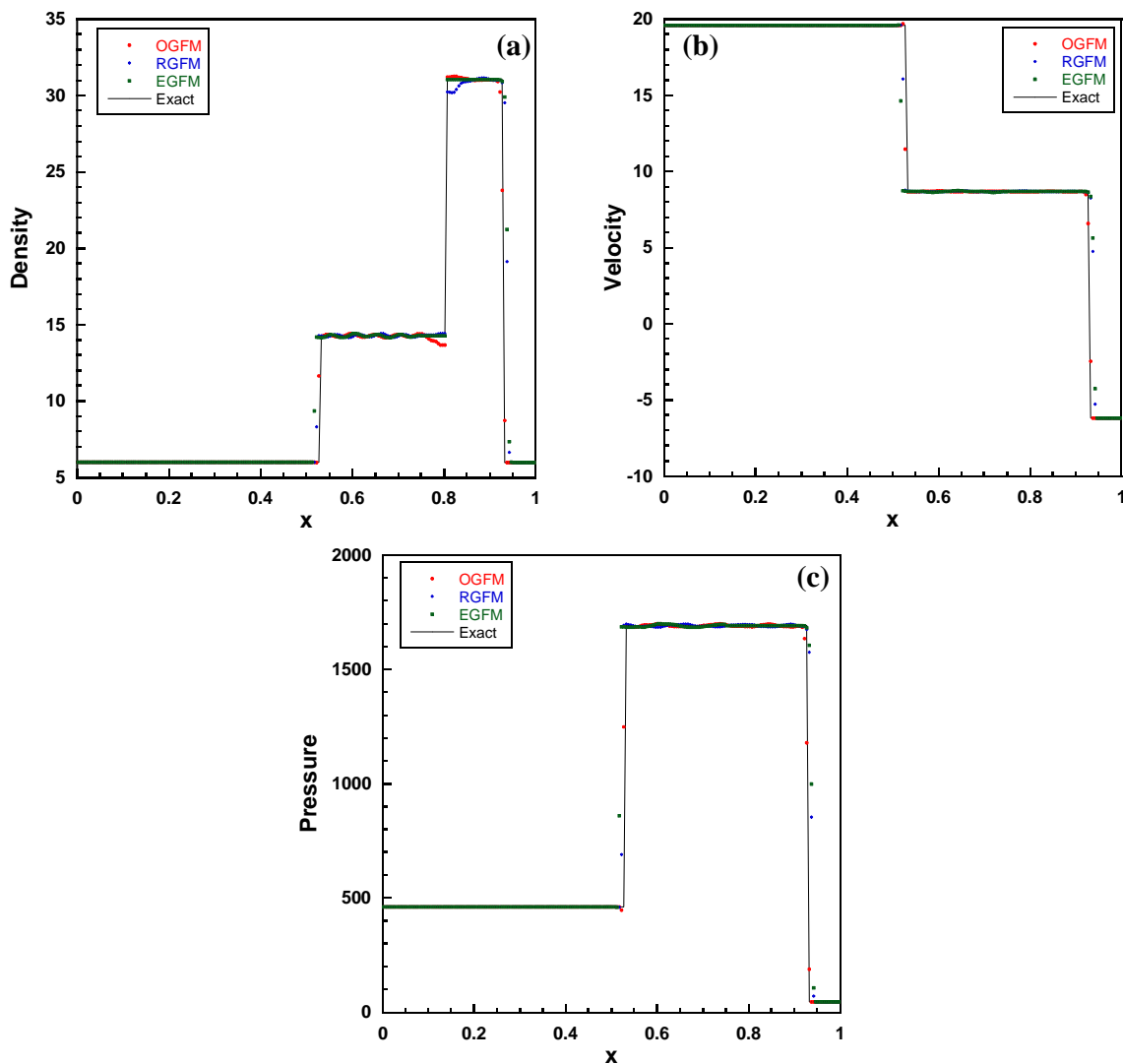
Figure 4.16. (a) Density, (b) velocity, and (c) pressure distributions for problem *4.1.5*. The numerical results exhibit oscillations between the left and right shock waves.
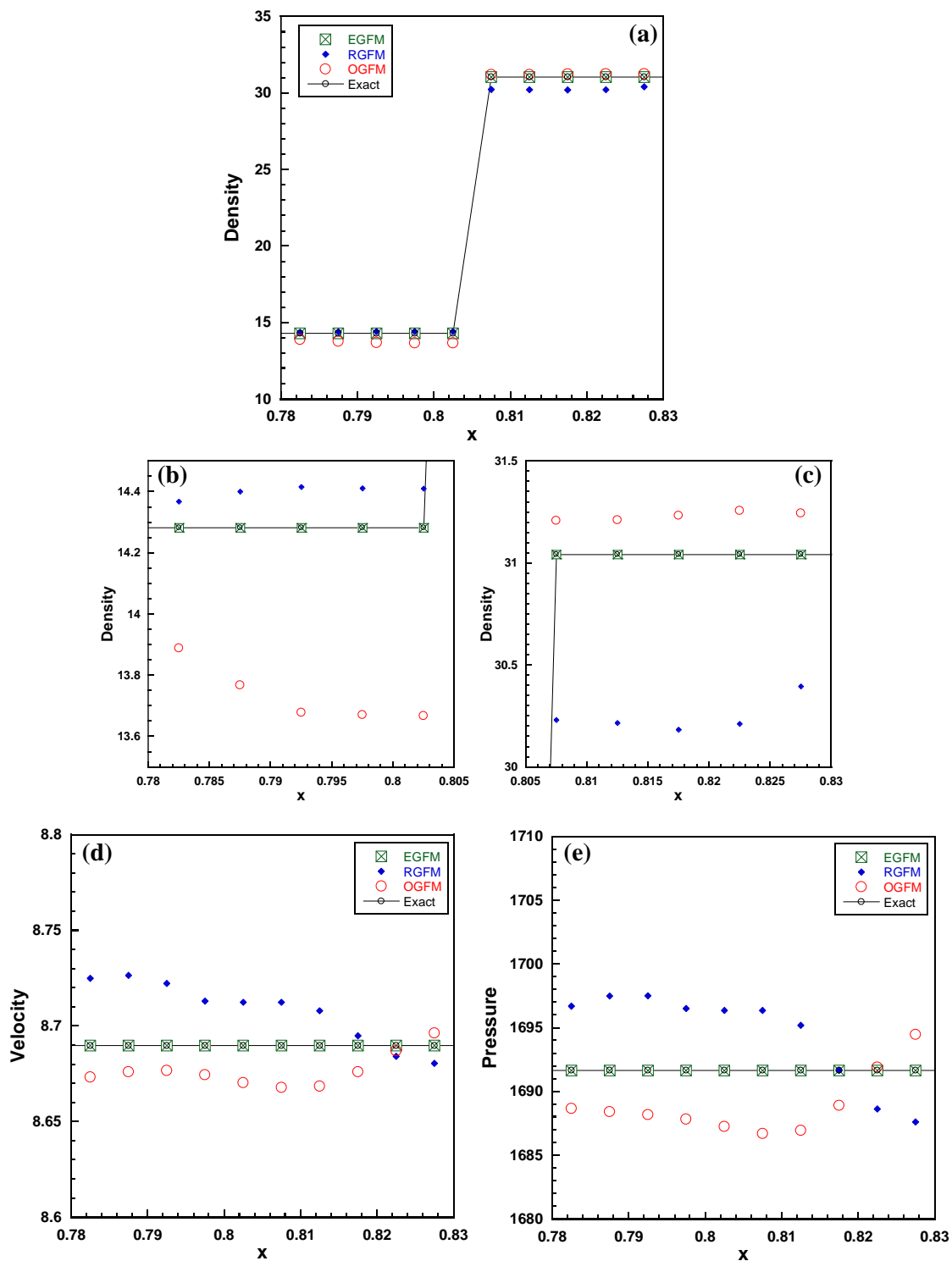
Figure 4.17. (a) Density, (d) velocity, and (e) pressure values near the interface. Density values on the (b) left and (c) right sides of the interface. The EGFM eliminates overheating as well as spurious oscillations in velocities and pressures.

4.1.6. Multi-component shock tube problem 1 [89]: This is an MMRP where a diaphragm separates two gases ($\gamma_L = 1.6$ and $\gamma_R = 1.4$) in the domain. The initial discontinuity is located at the center ($x_0 = 0.5$) of the shock tube and separates regions with a pressure ratio of 2500:1. The initial data may be summarized as

$$\boldsymbol{W}_L = (\rho_L, u_L, p_L) = (1,0,500),$$

$$\boldsymbol{W}_R = (\rho_R, u_R, p_R) = (1,0,0.2).$$

The solution [89] includes a left rarefaction and a right shock as shown for $t = 0.01$ in figure 4.18. Note that to obtain results using the OGFM, the CFL value must be reduced to ≤ 0.04, indicating the inefficiency of this approach for this MMRP. Furthermore, figures 4.18 and 4.19 show the results from the EGFM are of higher accuracy, while the OGFM and RGFM results contain strong overheating and unphysical numerical reflections near the rarefaction. Note the OGFM erroneously places the interface location by more than three cells from its actual location (figure 4.19). See the discussion of problem *4.1.4* for the details of such behavior.
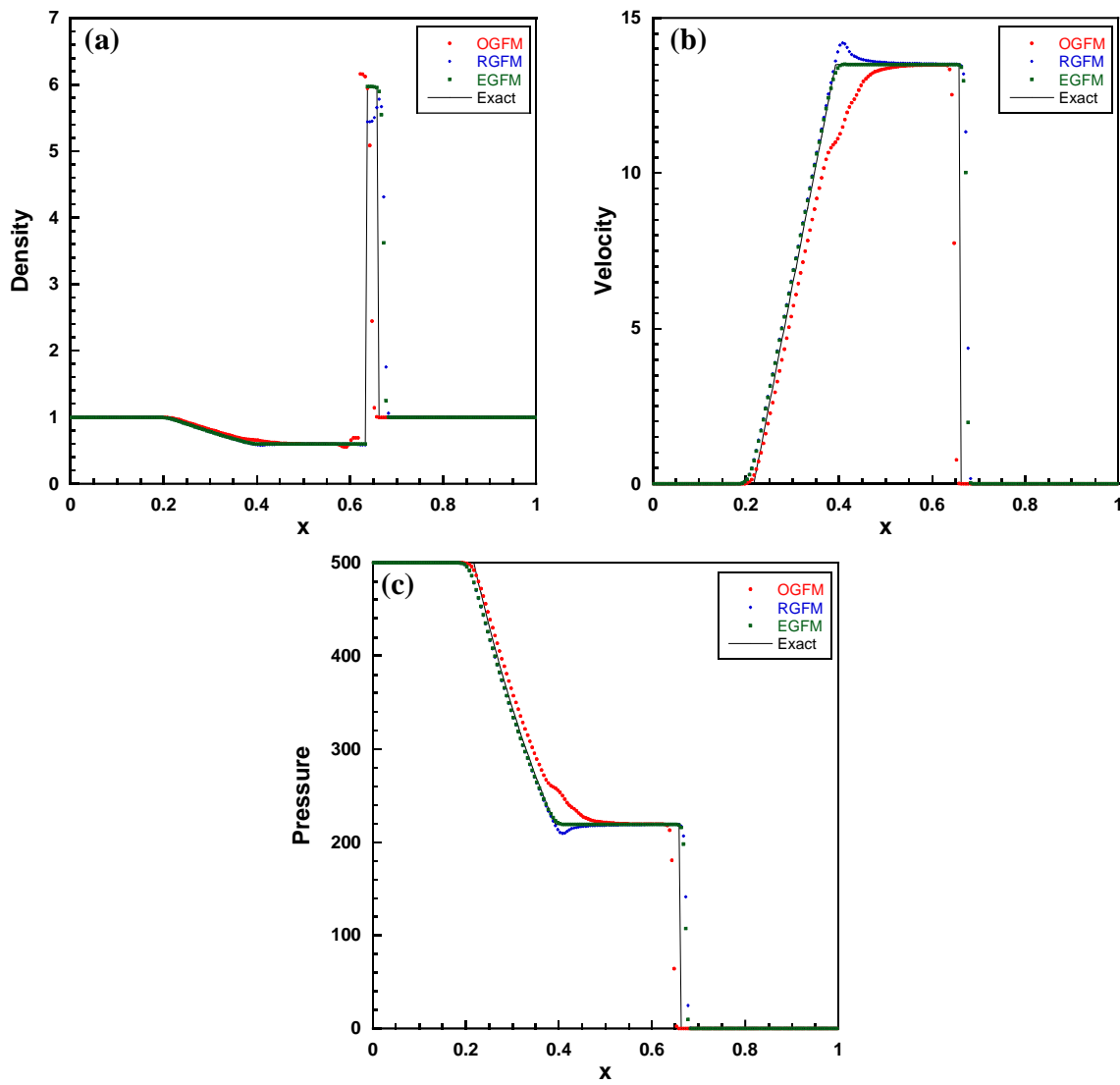
Figure 4.18. (a) Density, (b) velocity, and (c) pressure distributions for the multi-component shock tube problem.
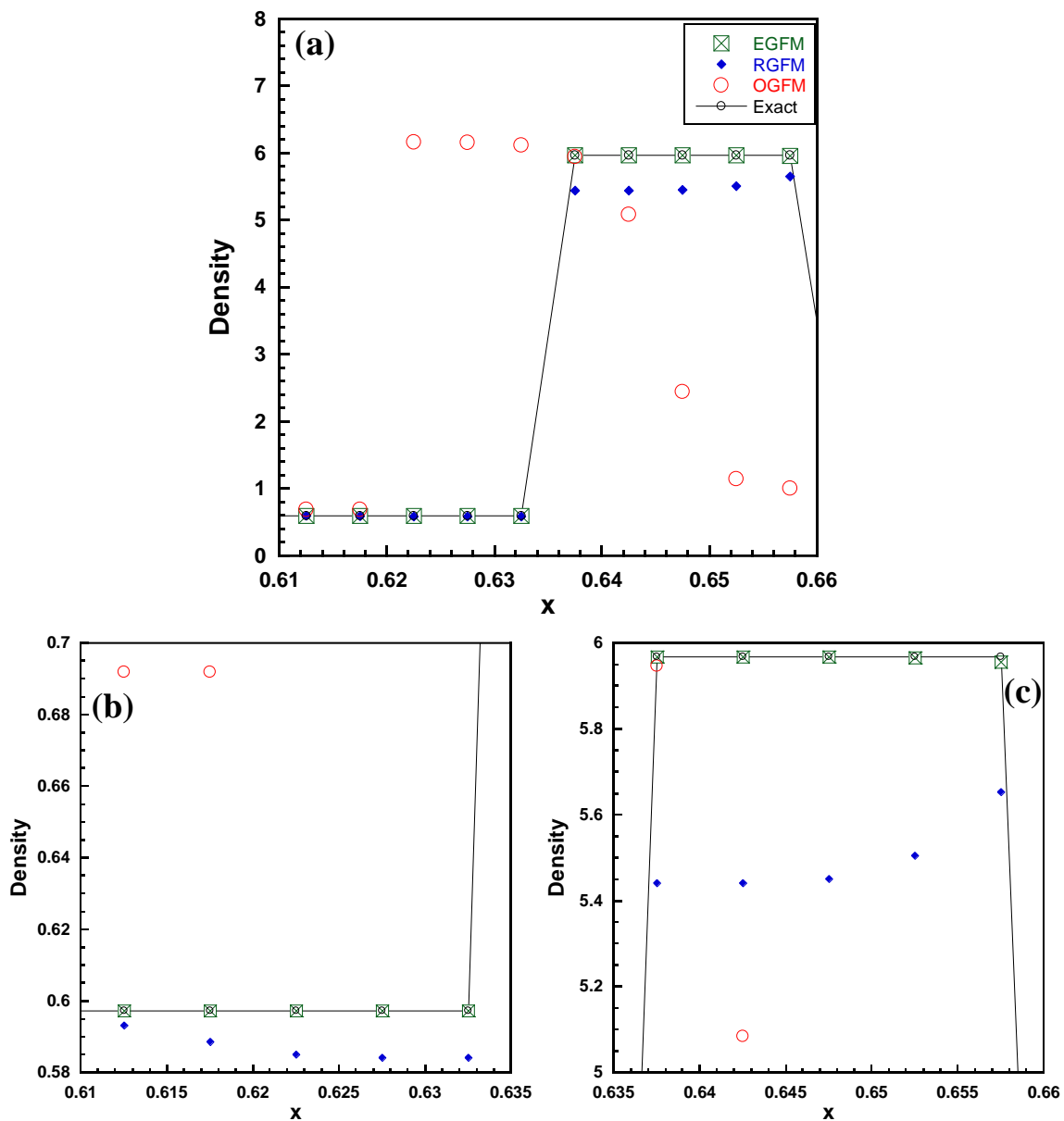
Figure 4.19. (a) Density values near the interface for problem *4.1.6*. Density values on the (b) left and (c) right sides of the interface. The OGFM and RGFM results display overheating errors, while the OGFM also miscomputes the interface location.

4.1.7. Multi-component shock tube problem 2 [36]: In this MMRP, the domain contains two gases ($\gamma_L = 1.6667$ and $\gamma_R = 1.4$) separated by a diaphragm at $x_0 = 0.2$ and the following initial data:

$$\boldsymbol{W}_L = (\rho_L, u_L, p_L) = (3.85563056, 8.562900568, 100),$$

$$\boldsymbol{W}_R = (\rho_R, u_R, p_R) = (0.1, 0, 1).$$

Removal of the diaphragm leads to a solution comprising a left rarefaction and a right shock, as shown in figure 4.20 for $t = 0.04$. As observed in the figure, the EGFM removes the numerical errors imposed by the OGFM and RGFM near the interface and the rarefaction. Figure 4.21 shows a detailed plot of the density profile near the interface, where the outcomes of the three GFM versions are compared.
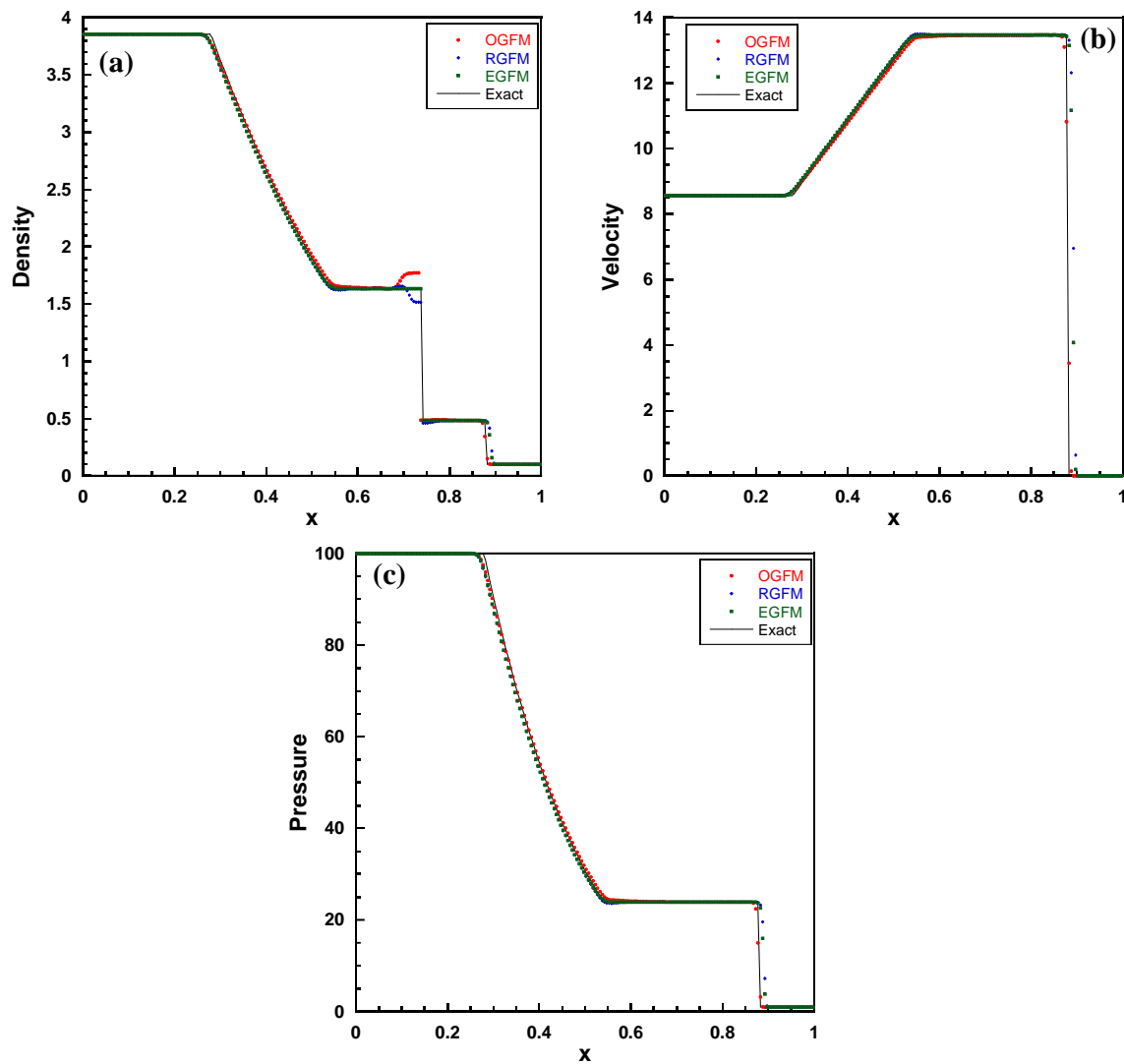
Figure 4.20. (a) Density, (b) velocity, and (c) pressure distributions for the MMRP in problem *4.1.7*. The OGFM and RGFM exhibit strong overheating in the density profiles.
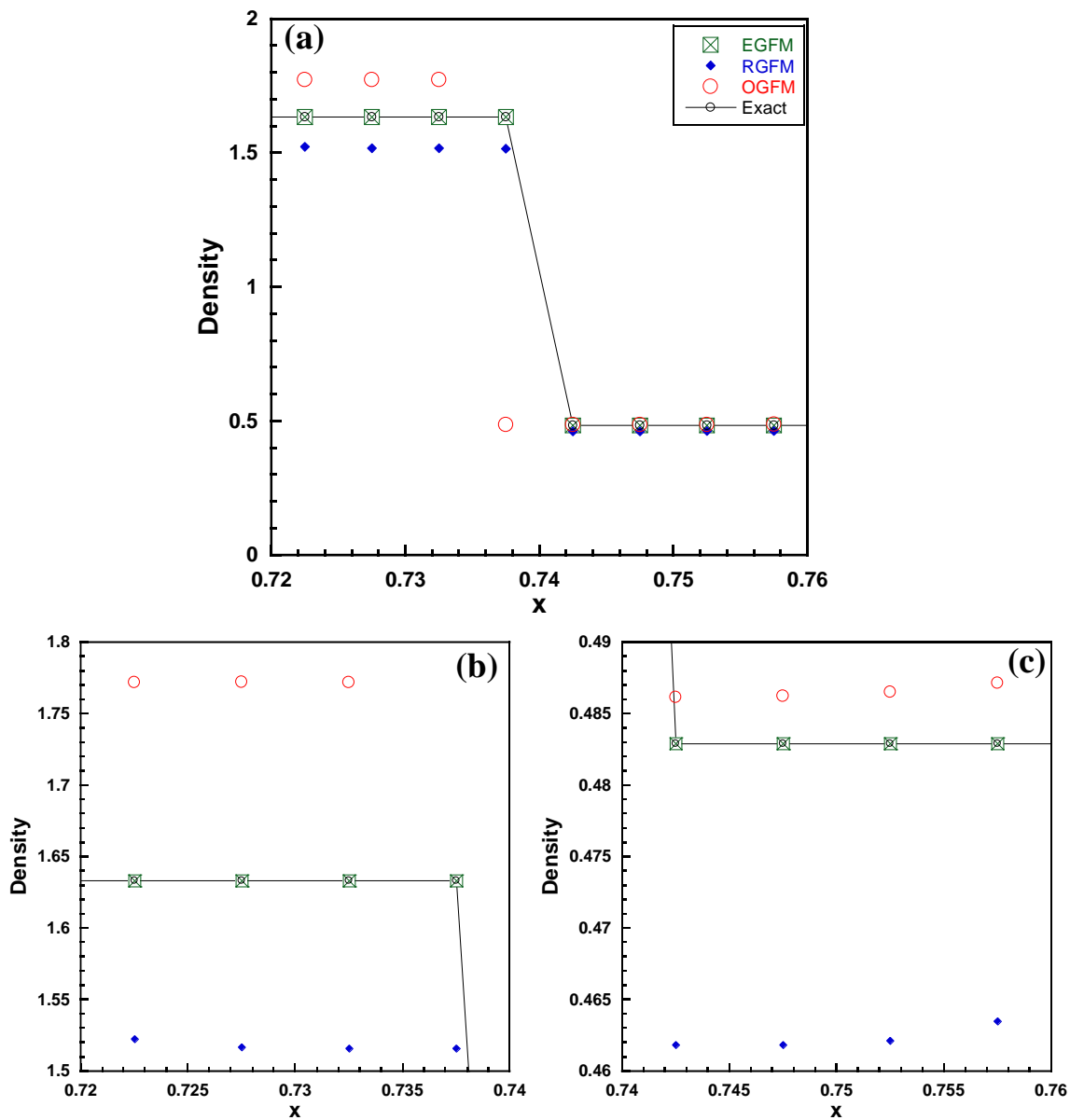
Figure 4.21. (a) Density values near the interface. Density values on the (b) left and (c) right sides of the wave. The EGFM removes overheating and computes the correct location of the interface.

4.1.8. Multi-component shock tube problem 3 [36, 38]: In this MMRP, the shock tube

domain is filled with high pressure air ($\gamma_L = 1.4$) and liquid water with the stiff gas EOS

parameters $\gamma_R = 7.15$ and $p_{\infty R} = 3309$. A diaphragm located at $x_0 = 0.5$ separates the two fluids, and the simulations are initialized with the following initial data:

$$\boldsymbol{W}_L = (\rho_L, u_L, p_L) = (0.00596521, 911.8821, 1000),$$

$$\boldsymbol{W}_R = (\rho_R, u_R, p_R) = (1,0,1).$$

The solution results in two shock waves with an interface located in between. Results are shown as density, velocity and pressure plots for $t = 0.0007$ in figure 4.22. In this multi-medium problem, the solution by the OGFM breaks down after a few time steps [36] (see the discussion in problem *4.1.3*), while the RGFM exhibits overheating and places the interface one cell away from its actual location. Once again, the EGFM results in exact values near the interface shown in detail in figure 4.23. Both the RGFM and EGFM, nonetheless, show small oscillations near the shock waves. This problem highlights the significance and superiority of MMRP-based GFM approaches over the OGFM in handling problems involving dramatically different stiffnesses.
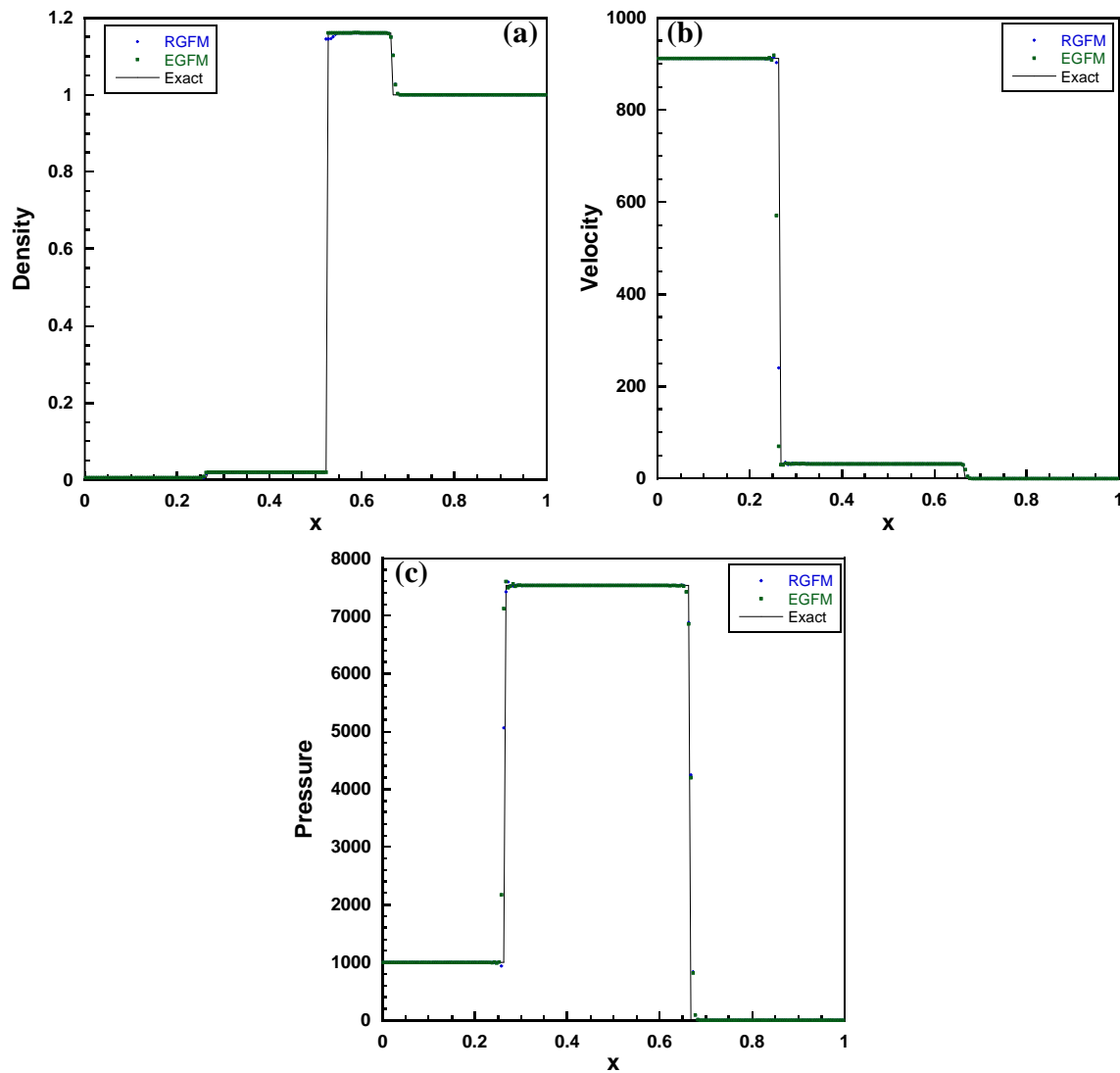
Figure 4.22. (a) Density, (b) velocity, and (c) pressure distributions for the gas-water shock tube in problem *4.1.8*.
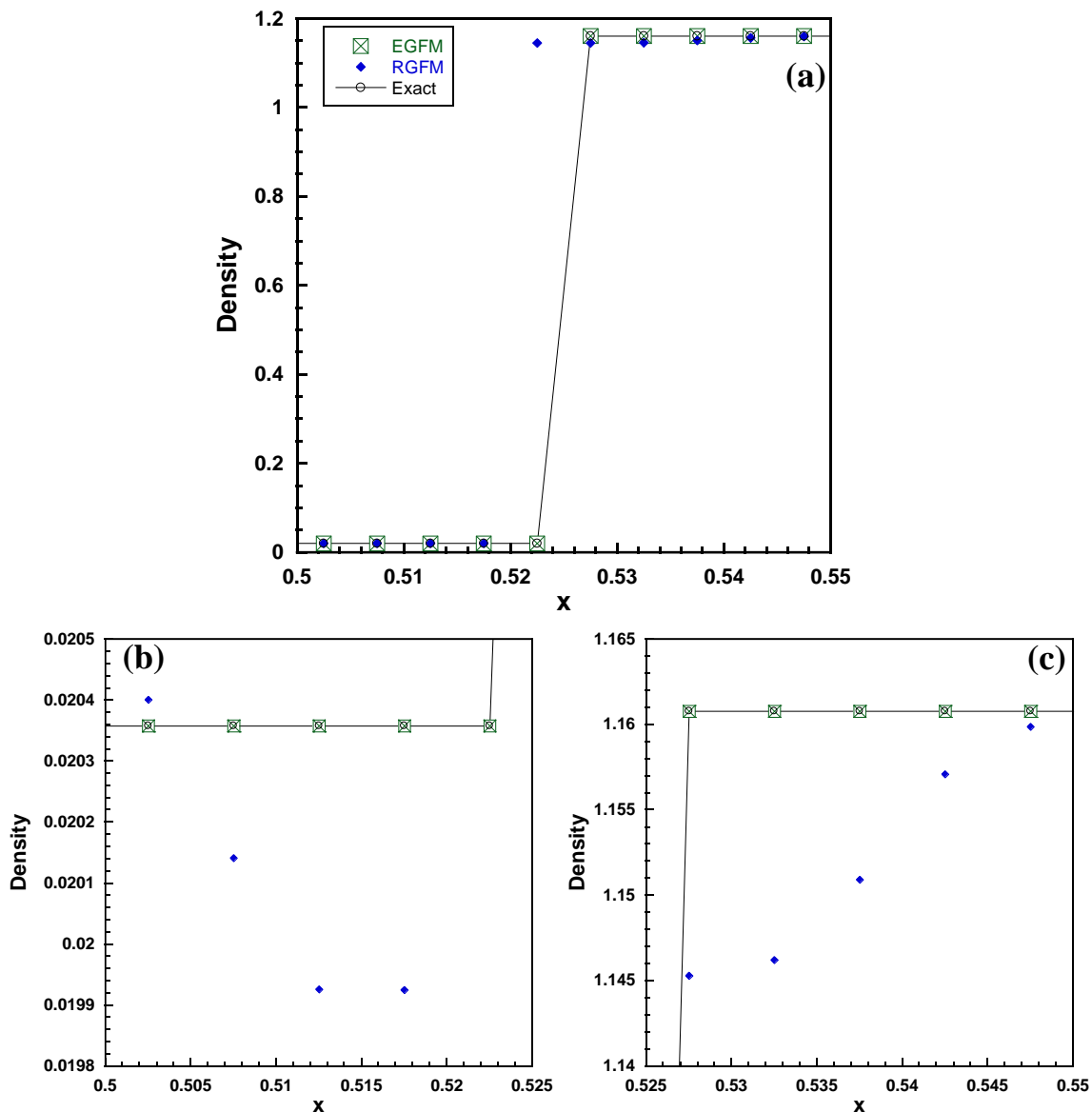
Figure 4.23. (a) Density values near the interface. Density values on the (b) left and (c) right sides of the interface. The OGFM solution breaks down after a few time steps, while the EGFM provides the exact values and interface location.

4.1.9. Strong shock impacting on a gas-gas interface (heavy → light) [26]. A gas-gas interface is processed by a strong shock, in a domain of length 1 m. (the corresponding 2D problem with a perturbed interface would lead to the development of the Richtmyer-

Meshkov instability). A right-traveling shock wave is initialized at $x_{S0} = 0.05\ m$, while

the interface is initially positioned at $x_0 = 0.5\ m$ and separates two gases ($\gamma_L = 1.4$ and

$\gamma_R = 1.67$). The complete initial conditions are given below

$$\boldsymbol{W}_S = (\rho_S, u_S, p_S) = (4.3333\ kg/m^3, 1037.7647\ m/s, 1.5 \times 10^6\ Pa),$$

$$\boldsymbol{W}_L = (\rho_L, u_L, p_L) = (1\ kg/m^3, 0\ m/s, 10^5\ Pa),$$

$$\boldsymbol{W}_R = (\rho_R, u_R, p_R) = (0.1379\ kg/m^3, 0\ m/s, 10^5\ Pa)$$

where we have used the subscripts as in figure 3.12. Since this is a '*heavy-to-light*' case,

the solution will consist of a rarefaction reflecting from the interface and a shock wave

transmitted into the light gas. This wave structure is seen in figure 4.24 where the solutions

by the OGFM, RGFM, and EGFM are compared to the analytical values at $t = 0.0005\ s$.

In figure 4.24, we observe that both the OGFM and RGFM exhibit a trough around $x = 0.2\ m$. As pointed out by Fedkiw et al. [26], this artifact stems from defining the shock as

a perfectly sharp discontinuity in the initial condition. In spite of this, we notice that the

EGFM provides the correct density, velocity, and pressure values near this feature, as

depicted in detail in figure 4.25. This is expected since the EGFM explicitly removes the

numerical errors (§ 3.4) imposed by shock capturing schemes that seek to resolve the

shock. Furthermore, it is observed that the interface obtained from EGFM is free of

overheating, in contrast to the results from the OGFM and RGFM schemes. This is

highlighted clearly in the detailed plot shown in figure 4.26.
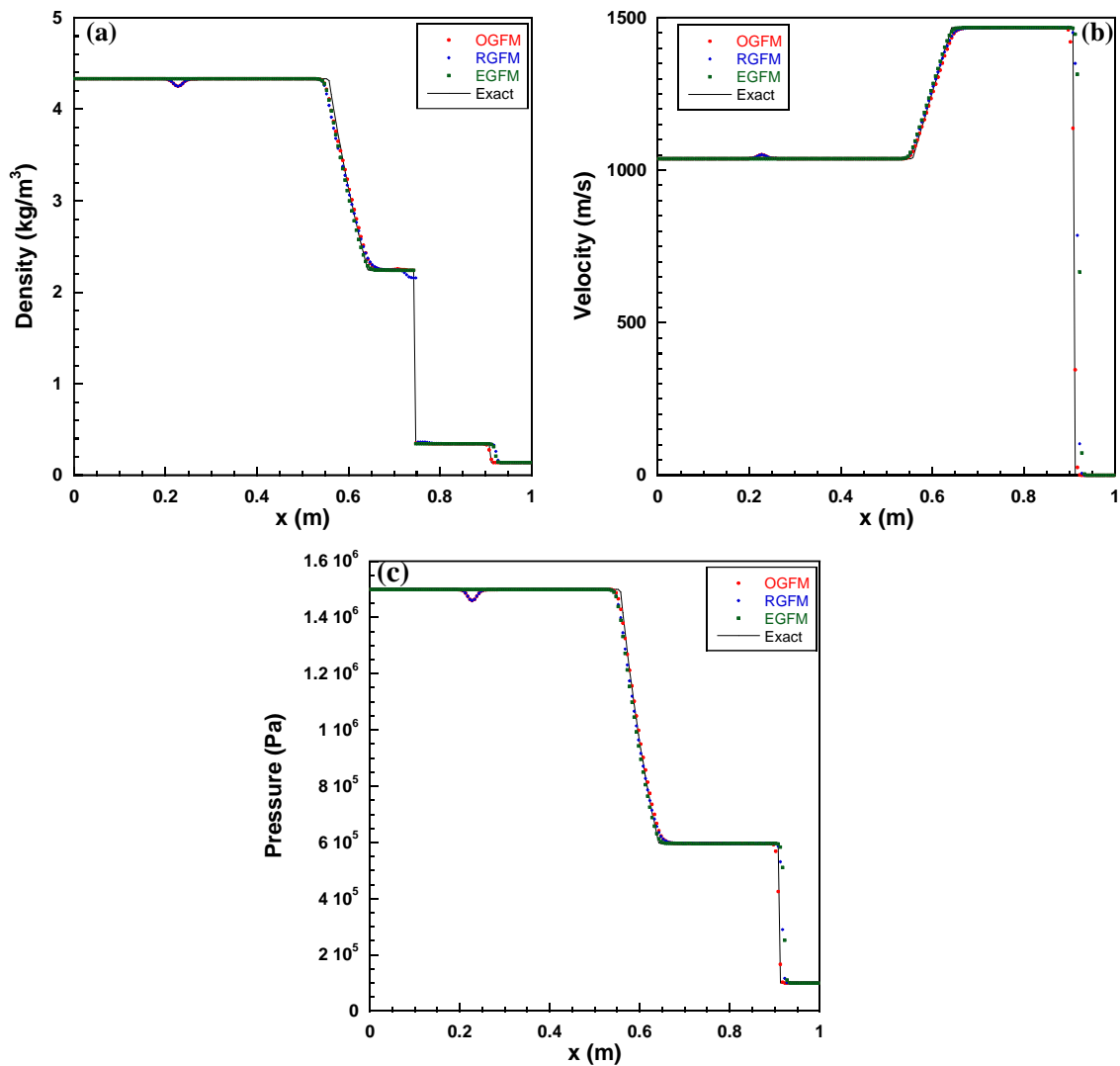
Figure 4.24. (a) Density, (b) velocity, and (c) pressure profiles in a heavy-to-light case. The EGFM eliminates the overheating and the numerical errors stemming from the shock capturing schemes.
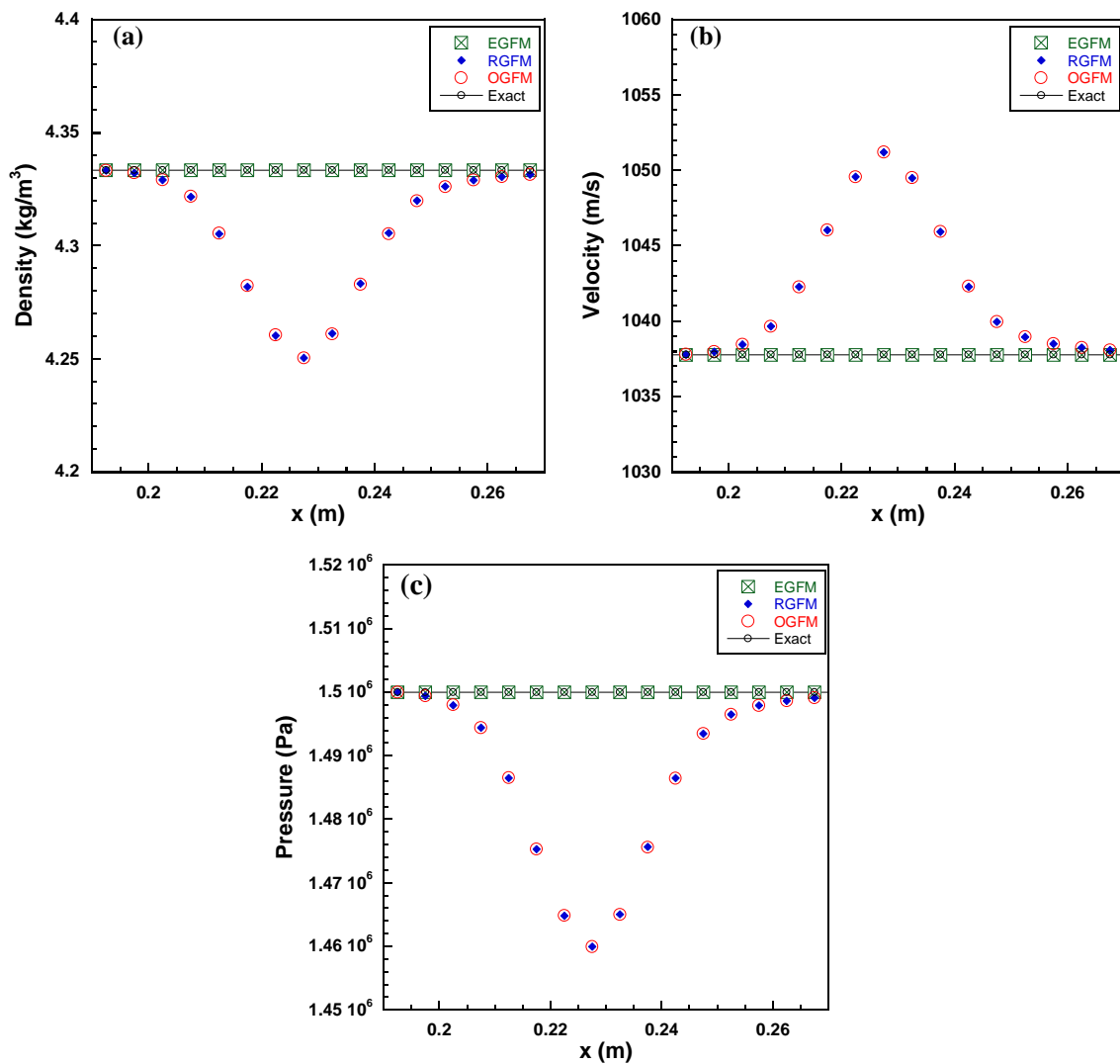
Figure 4.25. (a) Density, (b) velocity, and (c) pressure values near the numerical oscillation observed in the OGFM and RGFM schemes. The shock treatment carried out in the EGFM approach removes numerical errors imposed by shock capturing schemes.
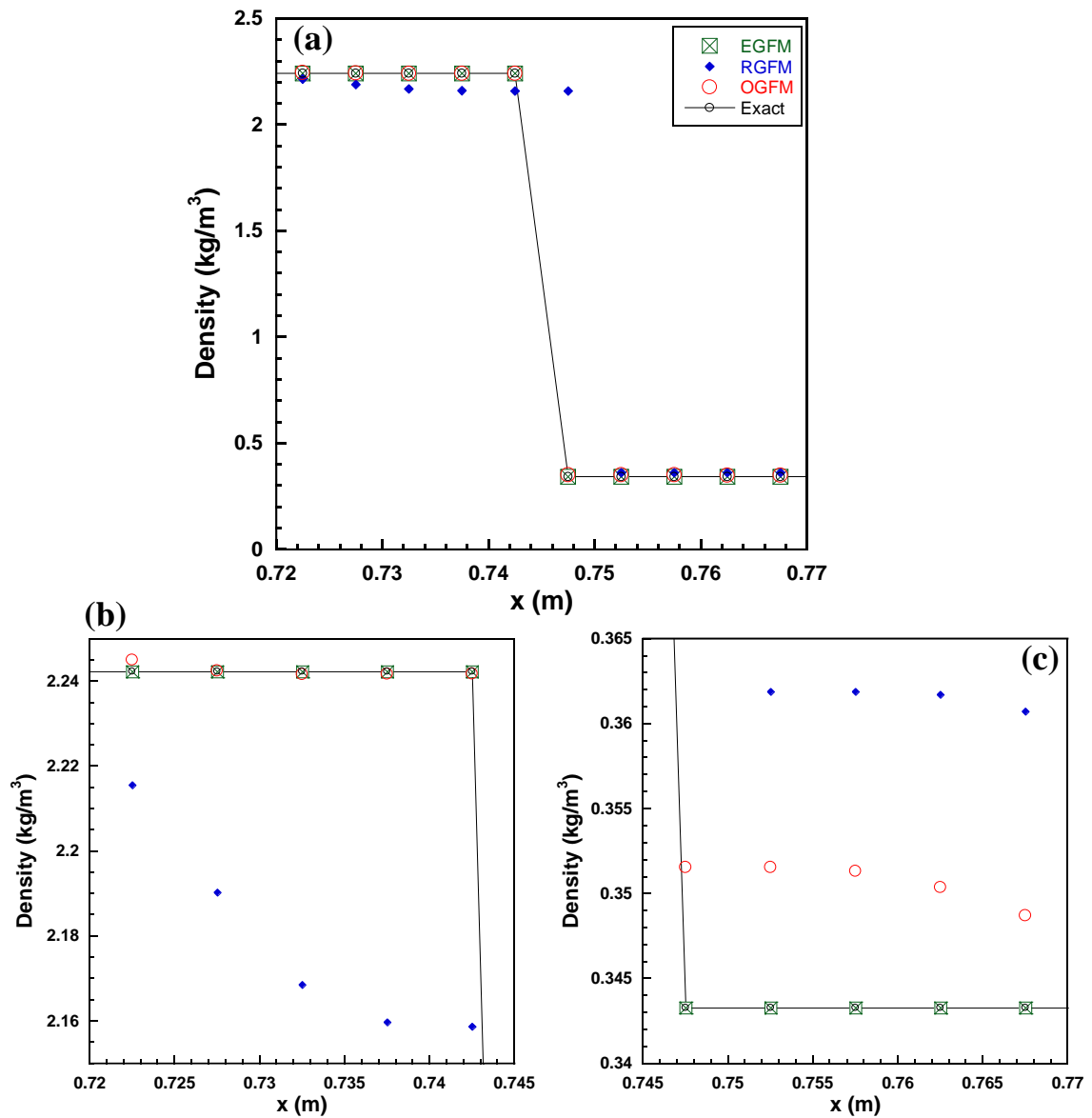
Figure 4.26. (a) Density profile near the interface for problem *4.1.9*. Density values on the (b) left and (c) right sides of the interface. The EGFM captures the density values and the interface location accurately.

4.1.10. Strong shock impacting on a gas-gas interface (light → heavy) [26]: This is similar to problem *4.1.9* except that the right fluid is replaced by a heavy gas of adiabatic index $\gamma_R = 1.249$ and the following initial condition:

$$\boldsymbol{W}_R = (\rho_R, u_R, p_R) = (3.1538 \; kg/m^3, 0 \; m/s, 10^5 \; Pa),$$

while the properties of the left gas are unchanged. Since the shock travels from the light gas to the heavy, both transmitted and reflected waves are shocks, while the interface will travel to the right. The expected wave structure is shown in figure 4.27 where the results from the OGFM, RGFM, and EGFM are compared to the exact solution at $t = 0.0007 \; s$. Once again, we observe that the shock treatment in the EGFM approach (§ 3.4) removes the numerical artifacts observed in the other approaches at $x \sim 0.3 \; m$. In addition, overheating has been eliminated by the EGFM solution, when compared with the numerical values obtained from OGFM and RGFM (see figure 4.28).
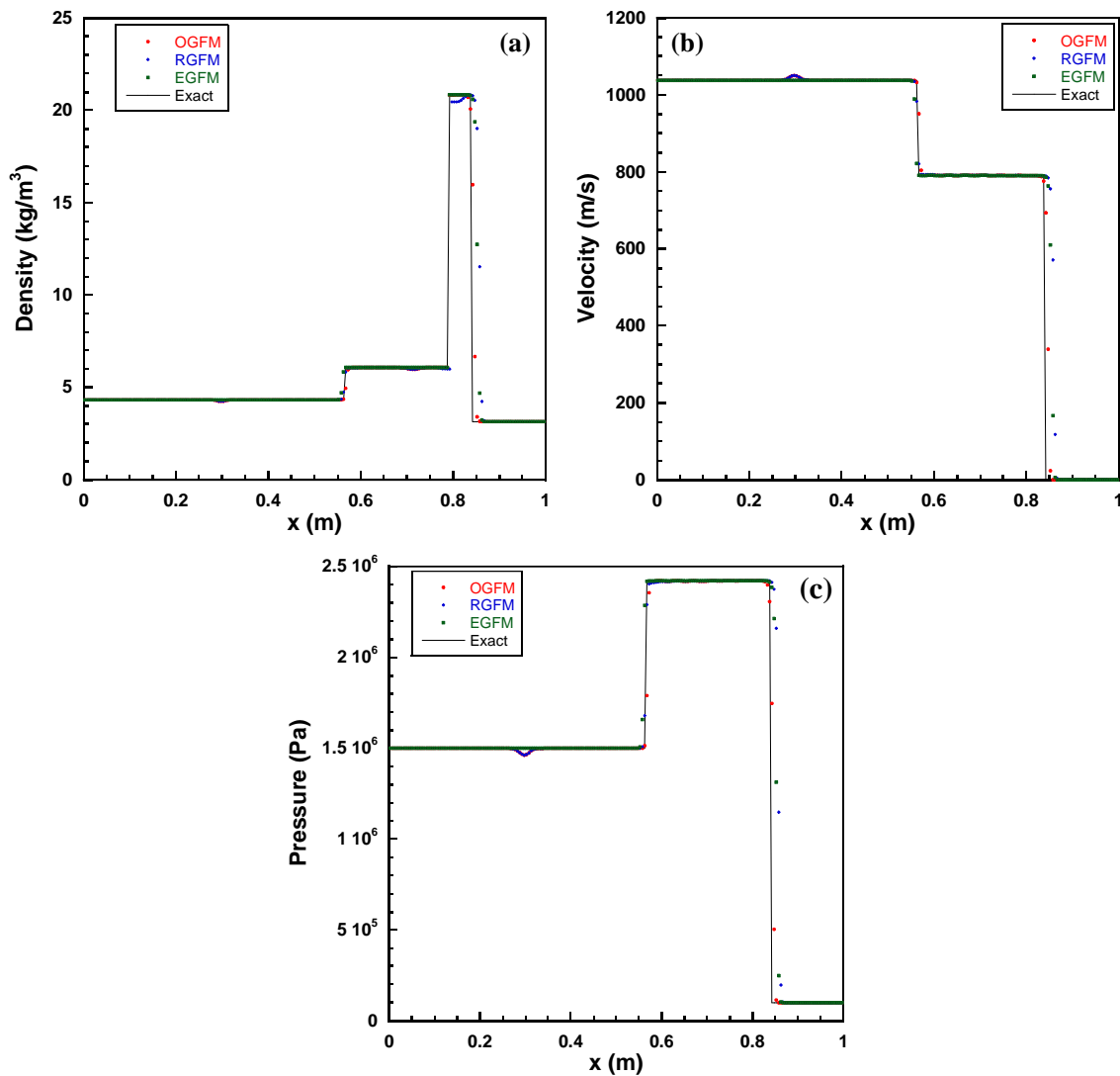
Figure 4.27. (a) Density, (b) velocity, and (c) pressure in a light-to-heavy case. The EGFM removes overheating and the numerical oscillation near $x = 0.3\ m$.
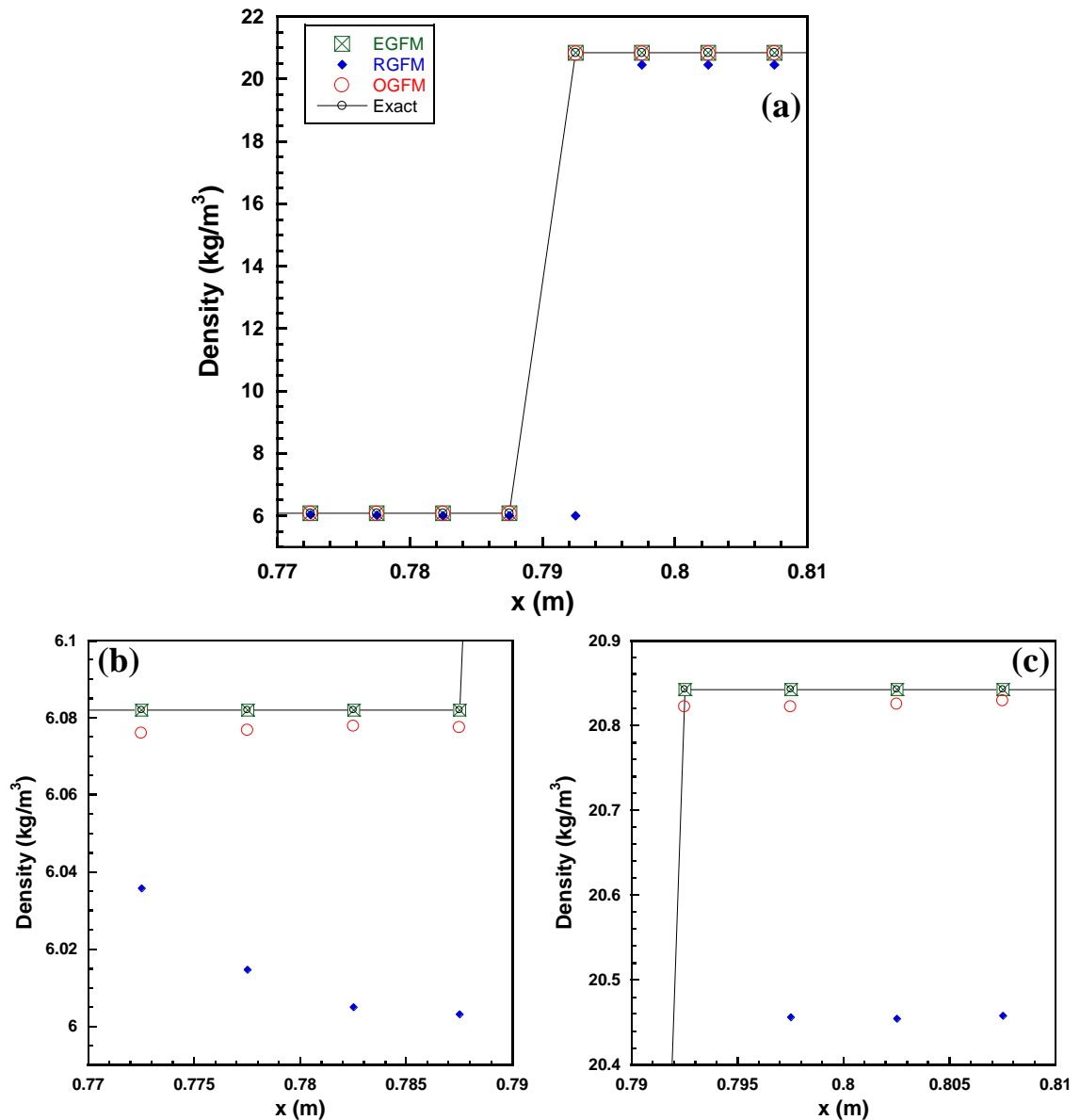
Figure 4.28. (a) Density profile near the interface. Density values on the (b) left and (c) right sides of the interface. The EGFM values match the exact solution, while the OGFM and RGFM exhibit overheating.

4.1.11. Strong shock impacting on a gas-water interface (heavy → light) [58]. In this example, the domain is occupied by air ($\gamma_L = 1.4$) and water ($\gamma_R = 4$ and $p_{\infty R} = 1$) where the two materials are separated by an interface at $x_0 = 0.5$. A strong leftward shock is

initialized at $x_{S0} = 0.6$ in the region of the shock tube containing water and traverses the interface. The complete initial data for this problem is:

$$\boldsymbol{W}_L = (\rho_L, u_L, p_L) = (1,0,1),$$

$$\boldsymbol{W}_R = (\rho_R, u_R, p_R) = (5,0,1),$$

$$\boldsymbol{W}_S = (\rho_S, u_S, p_S) = (7.093, -0.7288, 10)$$

where $\boldsymbol{W}_S$ represents the post-shock state. Since this is a heavy-to-light case, a rarefaction is reflected back in to the water, while a shock is transmitted into the air. Figure 4.29 shows this general solution structure from the analytical solution, as well as a comparison between the OGFM, RGFM, and EGFM approaches at $t = 0.2$. All the simulations shown in figure 4.29 were performed with a mesh of 250 cells and $CFL = 0.2$.

The introduction of the initial shock wave as a perfectly sharp discontinuity in the water leads to the formation of two blips in the solution propagating throughout the domain in time. However, these features (located at $x \sim 0.4$ and $x \sim 0.95$ at the end of the simulation), are removed by the shock treatment in the EGFM approach (§ 3.4). In addition, the EGFM eliminates overheating near the interface, as shown in detail in figure 4.30.
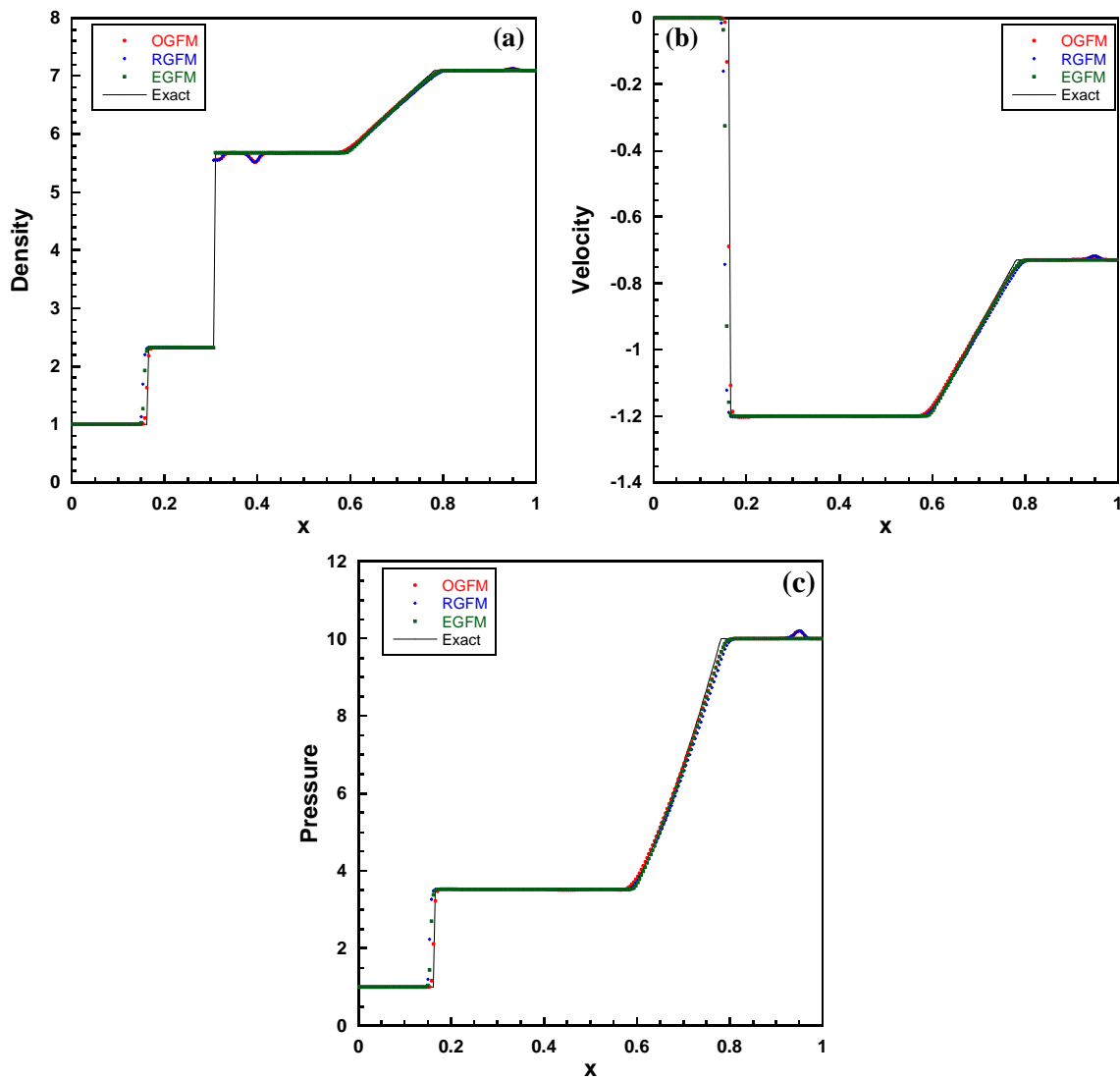
Figure 4.29. (a) Density, (b) velocity, and (c) pressure distributions for a shock impacting on a gas-water interface. The blips at $x = 0.4$ and $x = 0.95$ are removed owing to the shock treatment of the EGFM approach. The EGFM eliminates overheating as well.
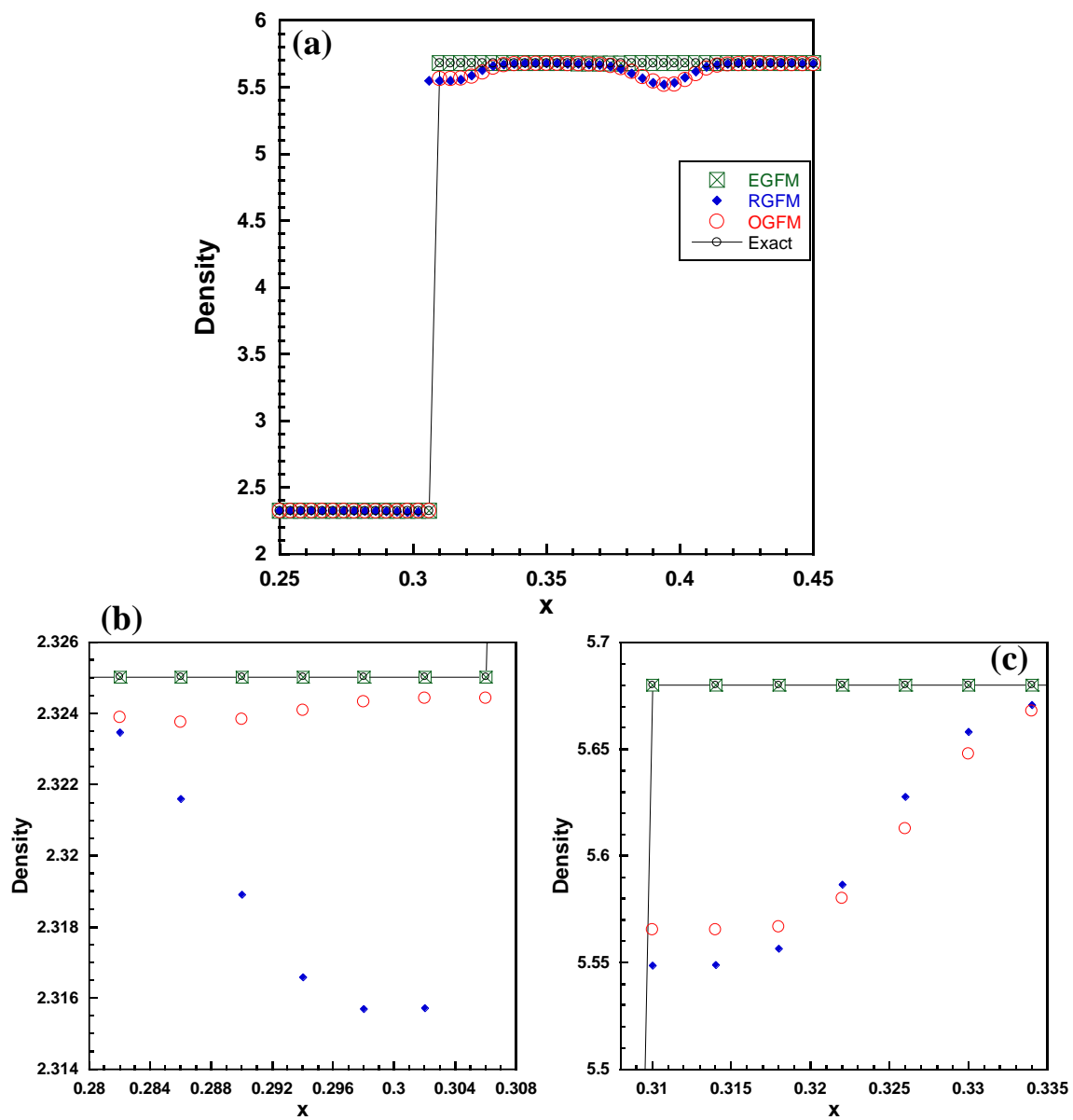
Figure 4.30. (a) Density profile near the interface for problem *4.1.11*. Density values on the (b) left and (c) right sides of the interface. The EGFM eliminates overheating and the numerical oscillation near the interface.

4.2 2D test cases

In this section, we present 2D test problems, where the different versions of the GFM were evaluated for their capabilities and robustness.

4.2.1. Underwater explosion of an air bubble [58]. An initially stationary, high pressure air bubble explodes in a domain filled with stationary water. The computational domain is square with dimensions 1×1, while the air bubble is a circle of radius 0.2 located at the center of the square. The initial condition for the air ($\gamma_a = 1.4$) and water ($\gamma_w = 5.5$ and $p_{\infty w} = 1.505$) regions were specified as follows:

$$W_a = (\rho_a, p_a) = (1.241, 2.753),$$

$$W_w = (\rho_w, p_w) = (0.991, 3.059 \times 10^{-4}).$$

The solution contains a rarefaction wave propagating toward the center of the circle, and an outward-propagating shock wave. The solution is obtained at $t = 0.058$ using the OGFM with 100×100 cells and $CFL = 0.3$ is shown in figures 4.31 and 4.32. The density contours in figure 4.31 highlight the presence of a rarefaction, interface, and shock. While the shock wave is slightly diffused, the interface remains sharp indicating negligible diffusion owing to the sharp interface approach of the GFM. This is better seen in figure 4.32 where the solution has been plotted for $y = 0.5$ and at $t = 0.058$ and shows good agreement between the results from IMPACT and those from LeVeque et al. [91] where the solution was obtained using 1D multi-component model for Riemann problem with source terms to account for radial symmetry.
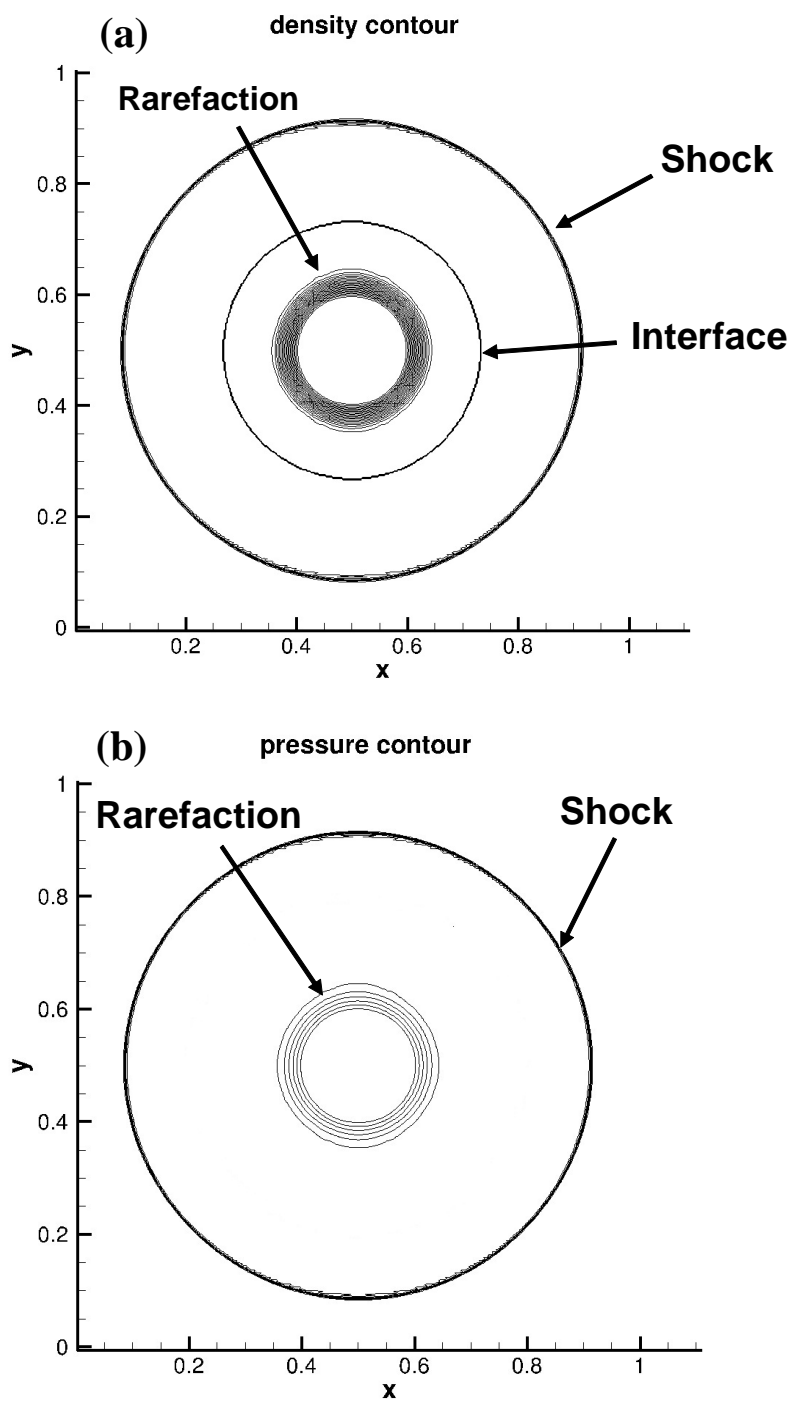
Figure 4.31. (a) Density and (b) pressure contours from the underwater explosion problem. The solution contains an inward-propagating rarefaction and outward-propagating interface and shock. The interface remains sharp owing to the implementation of the GFM.
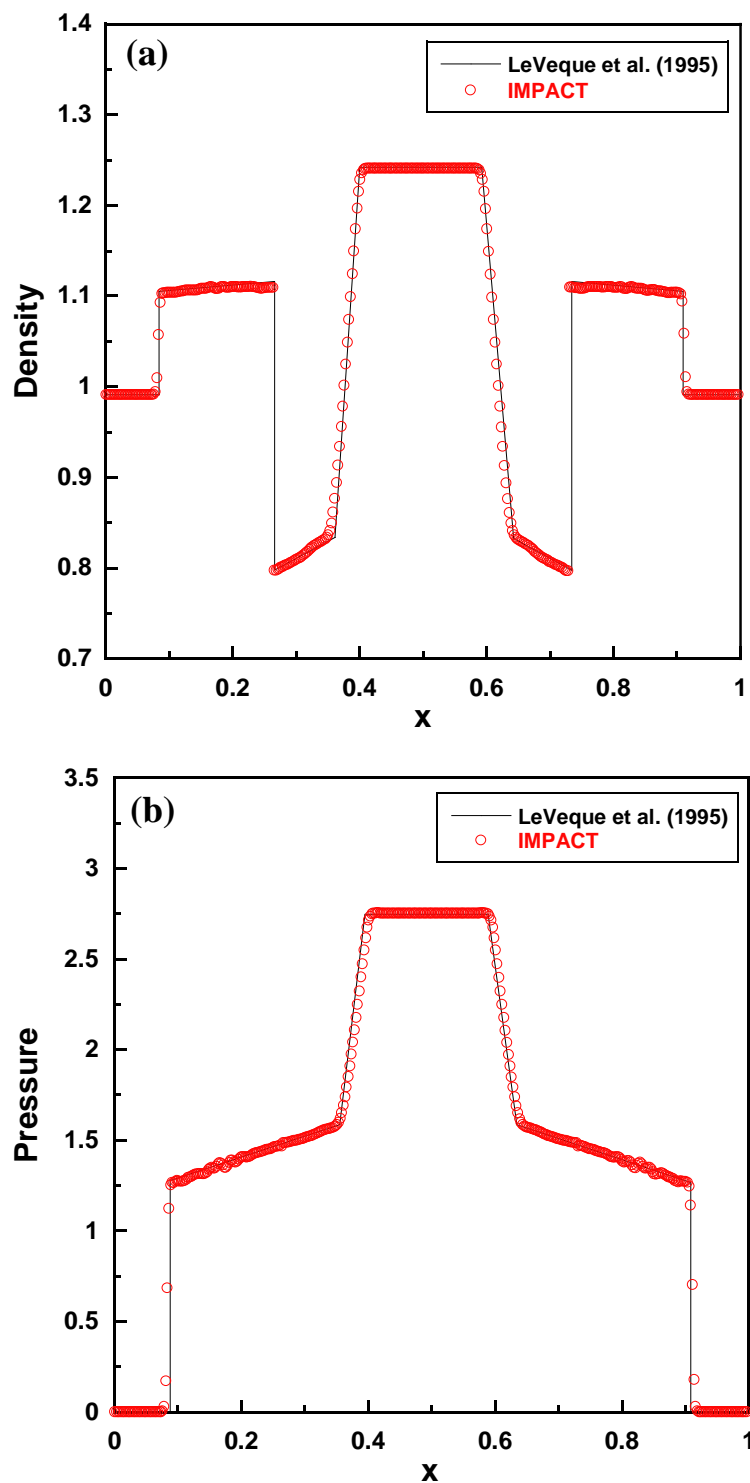
Figure 4.32. (a) Density and (b) pressure distributions along a cross section ($y = 0.5$) of the domain. Interface and wave locations have been properly captured by IMPACT, and show good agreement with the results from LeVeque et al. [91].

4.2.2. Strong shock impacting an air cavity [90] (heavy → light): In this problem, a strong shock in water travels to the right and impacts a circular air cavity. The computational domain is a rectangular box of dimensions $13.8 \ mm \times 12 \ mm$ filled with water, in which the air cavity of radius $3 \ mm$ is centered at $(6 \ mm, 6 \ mm)$. The shock is initially located at $x = 1.8 \ mm$ and divides the water into post- and pre-shock states. The initial condition of the air ($\gamma_a = 1.4$) and water ($\gamma_w = 4.4$ and $p_{\infty w} = 6 \times 10^8 \ Pa$) are as follows:

$$\boldsymbol{W}_{w,post} = (\rho, u, v, P)_{w,post} = (1323.6478 \ kg/m^3 \ , \ 681.577871 \ m/s \ , \ 0, \ 1.9 \ GPa),$$

$$\boldsymbol{W}_{w,pre} = (\rho, u, v, P)_{w,pre} = (1000 \ kg/m^3 \ , \ 0, \ 0, \ 10^5 \ Pa),$$

$$\boldsymbol{W}_a = (\rho, u, v, P)_a = (1 \ kg/m^3 \ , \ 0, \ 0, \ 10^5 \ Pa).$$

The computational domain consists of 230 and 200 cells in the x and y directions respectively, and the simulations were performed with $CFL = 0.4$ to a final time of $t = 3.05 \ \mu s$. The boundary conditions on the left and right boundaries are outflow, whereas the bottom and top boundaries are periodic. Due to the high strength of the shock and dramatic density contrast across the gas-water interface, the OGFM is unable to resolve this problem, and the simulation breaks down after a few time steps. We have used the modified version [27, 66] of the GFM here to obtain the solution shown in figures 4.33 and 4.34.
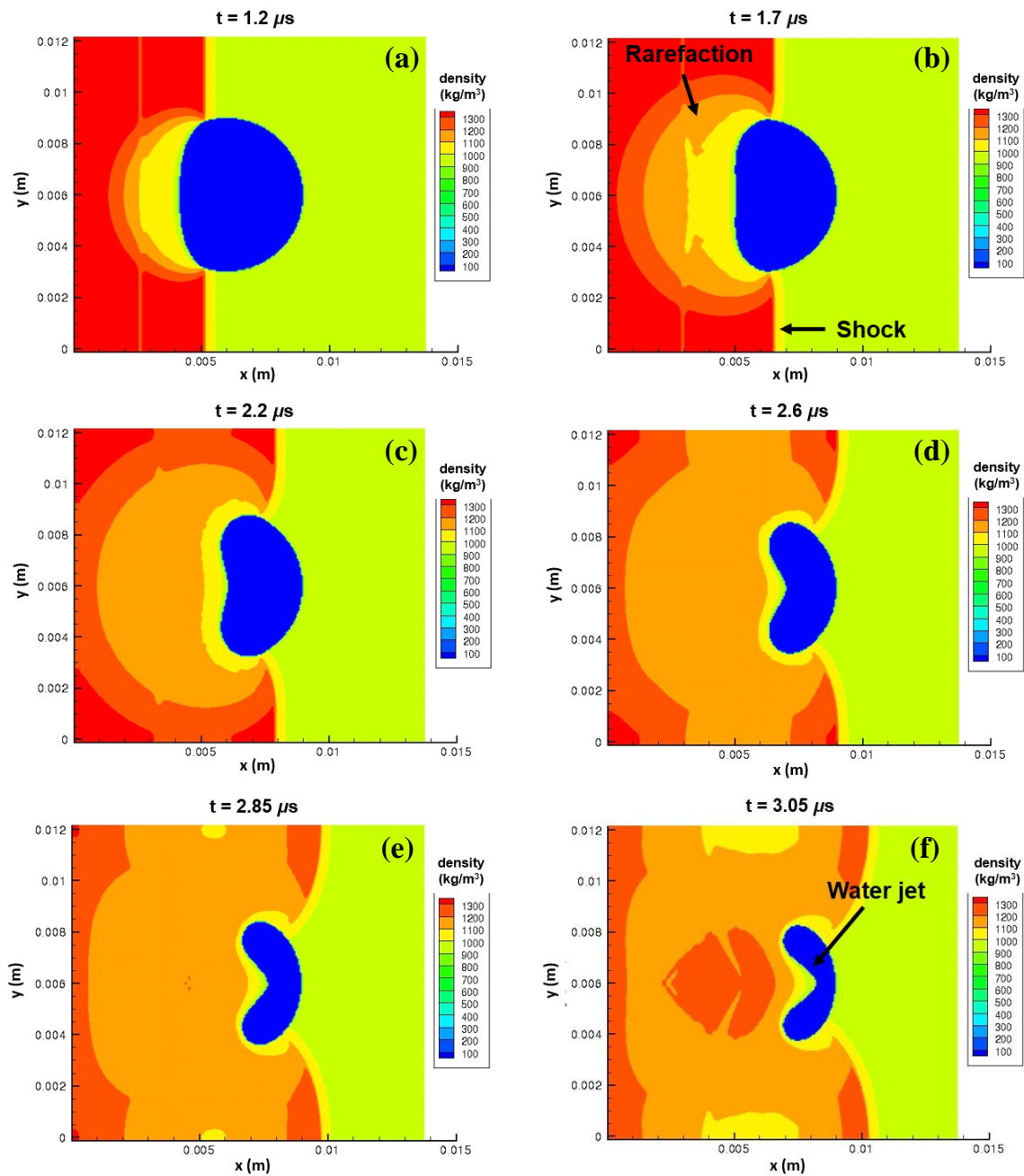
Figure 4.33. Density plots at different times in the shock-cavity interaction. The interaction results in a penetration of a water jet inside the cavity.

Since the shock-interface interaction is from heavy to light (At < 0), a rarefaction reflecting back in to the water is observed along with a transmitted shock into the air cavity. The

rarefaction wave is strong and visible in figure 4.33, while the transmitted shock is weak. We have plotted in figure 4.34 the line contours of density, so that the weak shock can be visualized. As before, we observe that the interface remains free of diffusion due to the GFM implementation.

The incident shock is initially planar, but is refracted by the air bubble and assumes an oblique shape near the interface. Furthermore, from figure 4.34, the speed of the incident shock is higher than the transmitted shock, and is due to the higher stiffness of water compared with air. The results presented in this problem are in good qualitative agreement with [90], and further underscores the capabilities of IMPACT in capturing flow features occurring under extreme conditions associated with strong shock waves and large density ratios.
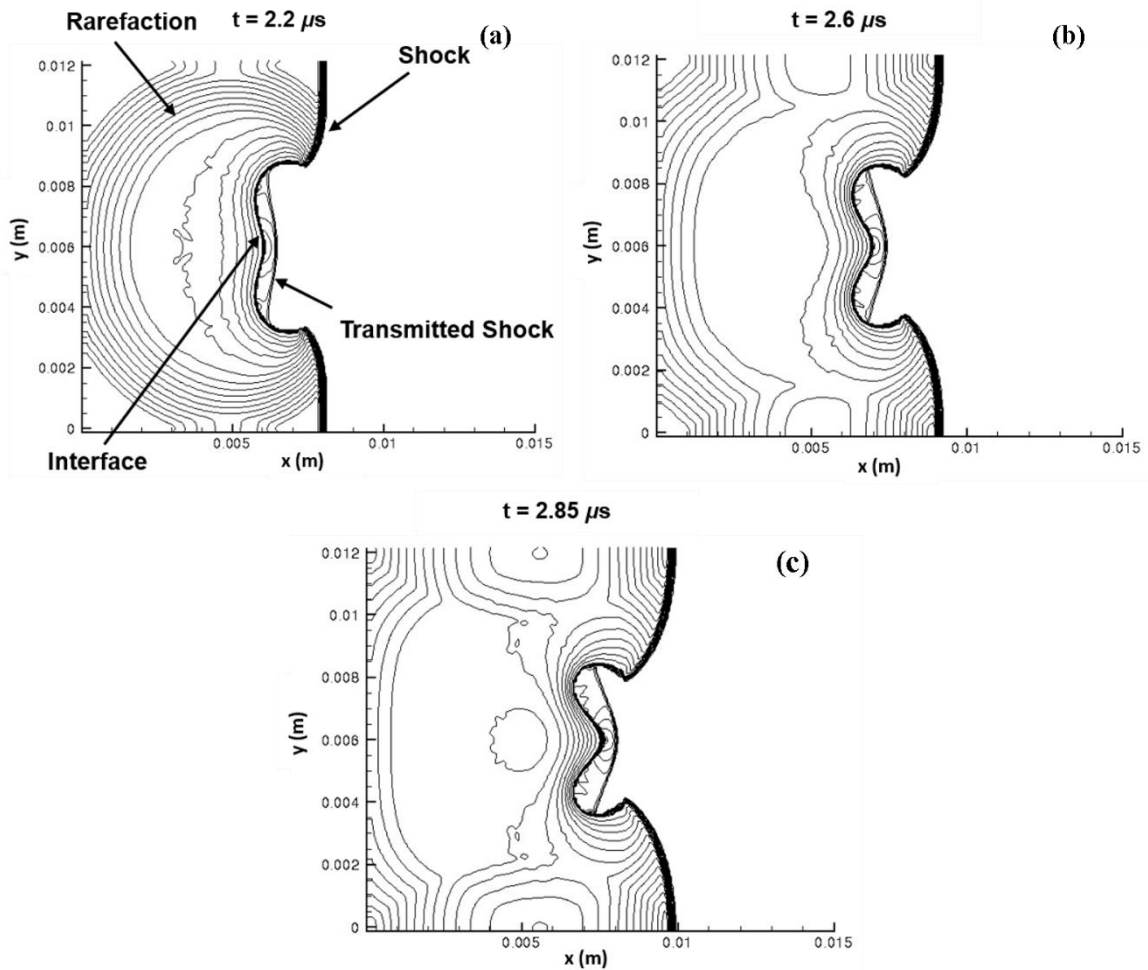
Figure 4.34. Density contours at (a) $t = 2.2 \, \mu s$, (b) $2.6 \, \mu s$, and (c) $2.85 \, \mu s$ for problem *4.2.2*. Due to the higher stiffness of water, shock velocities are higher in that medium, compared with the speed of the transmitted shock in the air cavity.

4.2.3. Shock-bubble interaction (light → heavy): A left-traveling shock wave is initialized in air and impacts a circular bubble containing R22. The domain is a rectangle of dimensions $267 \, mm \times 89 \, mm$ which contains an R22 bubble of radius $25 \, mm$ centered at $(178 \, mm, 44.5 \, mm)$, while the shock is initially at $x = 203 \, mm$. The initial conditions for the air ($\gamma_a = 1.4$) and R22 ($\gamma_{R22} = 1.249$) are given below:

$$\boldsymbol{W}_{a,pre} = (\rho, u, v, P)_{a,pre} = (1.4 \, kg/m^3, 0, 0, 10^5 \, Pa),$$

$$W_{a,post} = (\rho, u, v, P)_{a,post} = (1.927 \ kg/m^3, \ -114.42 \ m/s, \ 0, \ 1.57 \times 10^5 \ Pa),$$

$$W_{R22} = (\rho, u, v, P)_{R22} = (4.415 \ kg/m^3, \ 0, \ 0, \ 10^5 \ Pa).$$

The simulations were performed with 1200×400 cells in the x and y directions respectively ($CFL = 0.4$), and to a final time of $t = 820 \ \mu s$. The boundary conditions on the left and right boundaries were defined as outflow, while the bottom and top boundaries were defined as periodic surfaces. The density contours shown in figure 4.35 were obtained using the OGFM approach in IMPACT.
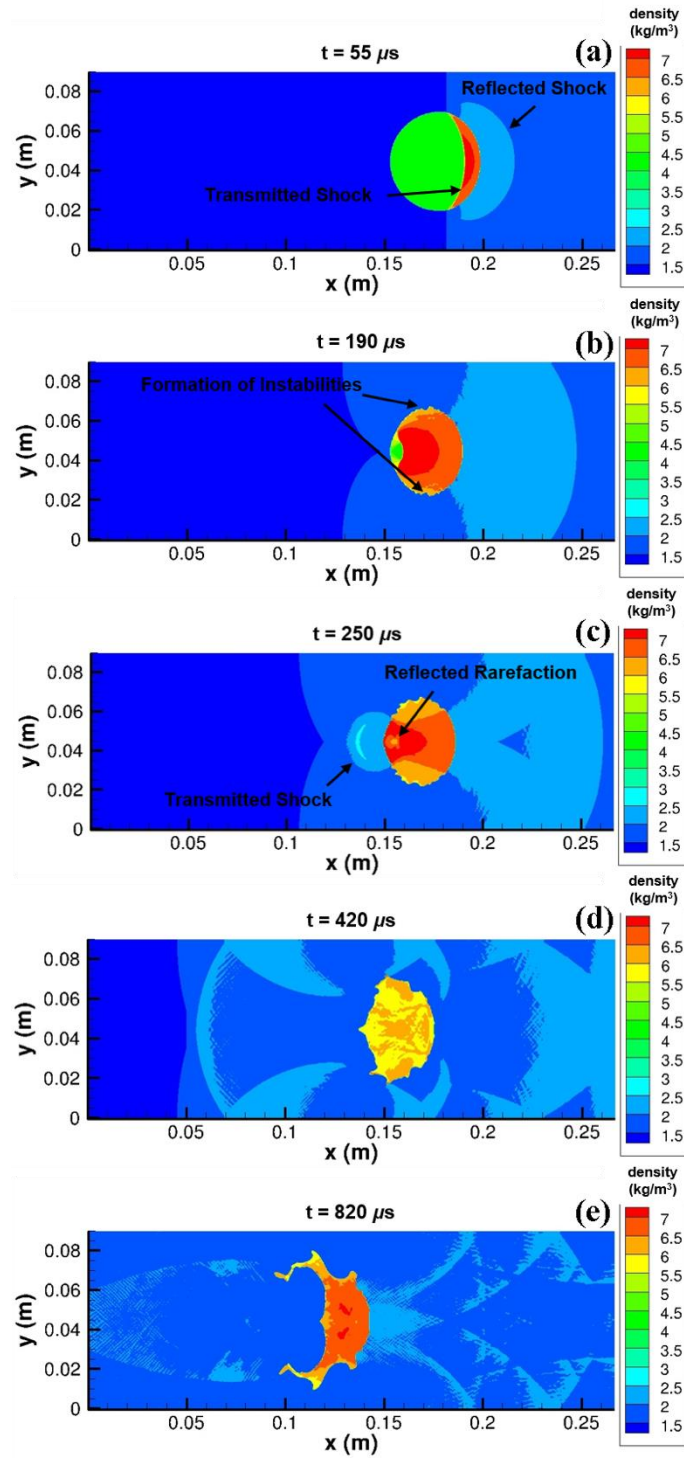
Figure 4.35. The evolution of the interface in shock-bubble interaction. (a) $t = 55\ \mu s$, (b) $190\ \mu s$, (c) $250\ \mu s$, (d) $420\ \mu s$, and (e) $820\ \mu s$. The passage of the shock wave results in a formation of the RMI at the interface.

The shock processes the R22 bubble in a light-to-heavy interaction, so that the initial interaction of the shock and the interface ($t = 55 \, \mu s$ in figure 4.35) results in a shock refraction leading to a reflected shock back into the air and a transmitted shock into the R22 bubble. The compression of the R22 bubble by the transmitted shock is also visible in figure 4.35, and results from the increased density and pressure in its post-shocked state. By $t = 190 \, \mu s$, the transmitted shock has reached the apex of the R22 bubble, and the subsequent passage of the shock from the heavy (R22) to light (air) medium results in a reflected rarefaction wave back in to the bubble, and a transmitted shock wave into the air. This wave pattern is observed in the solution at $t = 250 \, \mu s$.

The interaction of the shock wave with a misaligned density interface in the form of the R22 bubble, leads to the development of RMI due to the deposition of baroclinic vorticity at the site of the shock-interface interaction. The early 'seeds' of instability formation can be observed in figure 4.35, at the poles of the bubble ($t = 190 \, \mu s$) followed by growth and elongation of the bubble. Note that the poles represent the sites of maximum initial misalignment between the pressure gradient represented by the shock and the density gradient between the bubble and shocked air, and are hence the locations of maximum deposited baroclinic vorticity. Instability growth rates at these sites would thus be maximum. The evolution of the interface to later times ($t = 420 \, \mu s$ and $t = 820 \, \mu s$) demonstrates the effect of the deposited vortical structures on the interface where the 'wings' of the elongated bubble tend to roll up toward the centerline of the domain ($y = 44.5 \, mm$). The shock bubble problem investigated here demonstrates the robustness of the numerical methods implemented in IMPACT, in handling interfacial instabilities such as

RMI. In the next section, we study the RMI quantitatively and compare the results obtained from IMPACT with analytical models.

4.3 Richtmyer-Meshkov Instability

The single-mode RMI is investigated in this section using IMPACT. The problem setup is shown in figure 4.36, and involves a rectangular domain of dimensions $L_x \times L_y$ with an interface represented by $x = x_0 + h_0^- \cos(2\pi y/\lambda)$ where x_0 is the location of the unperturbed interface, h_0^- is the amplitude of the sinusoidal perturbation before shock impact, and λ is the perturbation wavelength.
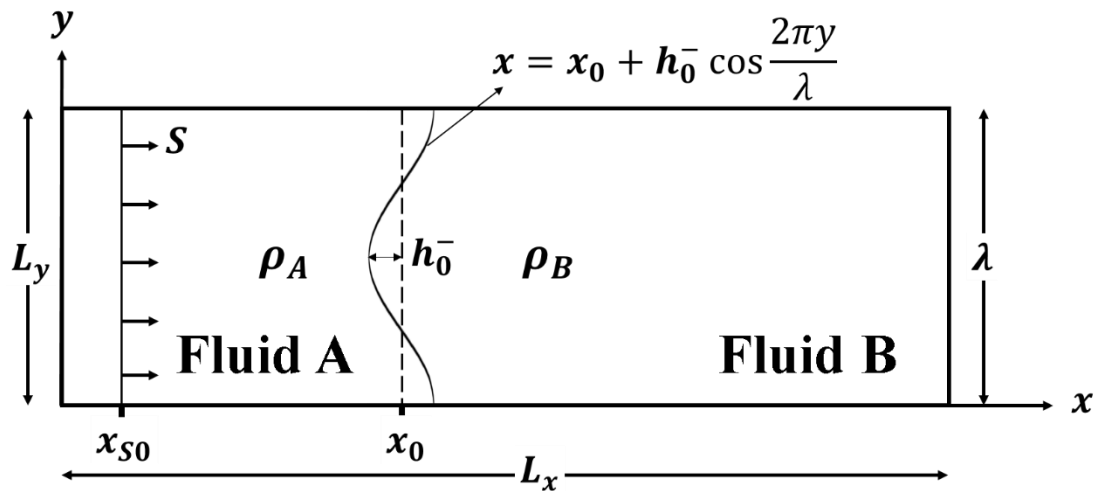
Figure 4.36. Problem setup for the RMI simulations. The interface between Fluids A and B is defined as a single-mode perturbation represented by a cosine wave.

In figure 4.36, the domain is occupied by Fluids A and B where Fluid A supports a planar shock wave traveling toward the interface with speed S. The density contrast between the two fluids is characterized by the pre-shock Atwood number $At^- = (\rho_B - \rho_A)/(\rho_B + \rho_A)$ where $At^- < 0$ indicates a heavy-to-light (or slow/fast) interaction and vice versa. The

amplitude of the perturbation is scaled by the wavenumber to define the nondimensional parameter kh_0^- where $k = 2\pi/\lambda$ is the perturbation wavenumber. The shock Mach number is defined as $Ma_S = S/a_A$, where a_A is the speed of sound in fluid A in its unshocked state.

The IMPACT simulations reported in this section were performed with air and SF_6 as the two fluids separated by the initial interface, and are labeled as Fluid A ($\gamma_A = 1.4$) and Fluid B ($\gamma_B = 1.093$) respectively. We use $\rho_A = 0.5\ kg/m^3$ and $\rho_B = 2.5\ kg/m^3$ to obtain $At^- = \frac{2}{3}$. The initial interface perturbation is characterized by the pre-shock amplitude $h_0^- = 0.056\ m$, and the perturbation wavelength $\lambda = 1\ m$ so that $kh_0^- = 0.35$. A planar shock with $Ma_S = 1.2$ is initially located at $x_{S0} = 0.4\ m$, while the interface is positioned at $x_0 = 0.5\ m$. The initial condition for the problem is detailed below:

$$\boldsymbol{W}_{A,post} = (\rho, u, v, P)_{A,post} = (0.67\ kg/m^3 , 161.68\ m/s , 0, 1.5 \times 10^5\ Pa),$$

$$\boldsymbol{W}_{A,pre} = (\rho, u, v, P)_{A,pre} = (0.5\ kg/m^3 , 0, 0, 10^5\ Pa),$$

$$\boldsymbol{W}_B = (\rho, u, v, P)_B = (2.5\ kg/m^3 , 0, 0, 10^5\ Pa).$$

The simulation domain had dimensions $L_x = 12\ m$ and $L_y = 1\ m$, with a mesh distribution of 1200 and 100 cells in the x and y directions respectively. The RMI simulations were performed with $CFL = 0.3$, and run to a final time of $t = 0.077866\ s$. The left and right boundaries were treated as outflow surfaces to allow for the egress of waves without acoustic feedback in to the domain, while the top and bottom boundaries were defined using periodic boundary conditions. We use the GFM approach of Sambasivan and UdayKumar [32] to obtain the solution.

Upon passage of the shock through the interface, the interface is accelerated to a velocity Δv and is compressed to a post-shock amplitude h_0^+ with a compression factor $\chi = h_0^+/h_0^-$. Under the influence of the deposited baroclinic vorticity, the perturbation amplitude grows in time with a growth rate dh/dt. In table 4.2, we compare the results from IMPACT with those predictions from the Rankine-Hugoniot relations applied to the RM situation [92, 93], and with analytical models for the RM linear growth rate [15, 16]. Table 4.2 shows excellent agreement between model predictions and measured quantities from the IMPACT simulation during the linear stage of RMI growth.

Table 4.2. A comparison of the results from theoretical models and IMPACT.

parameter	Theory	IMPACT
Δv (m/s)	106.58 ([92], [93])	107.22
At^+	0.696 ([92], [93])	0.697
h_0^+ (m)	0.0464 ([16])	0.0466
χ	0.832 ([16])	0.836
$dh/dt \equiv V_{RM}$ (m/s)	21.605 ([15])	21.870

We also validate IMPACT by comparing predictions of the interface evolution during the nonlinear phase of RMI with models based on potential flow theory. In figure 4.37, we plot density and LS contours at different nondimensional times kV_0t, where V_0 is the initial growth rate that accounts for finite-amplitude effects and is given by $V_0 = V_{RM}/\left[1 + (kh_0^-/3)^{4/3}\right]$ [94]. As seen in the figure, as the perturbation waveform enters

the nonlinear phase $kV_0t \gtrsim 1$, a distinct spike (penetration of heavier fluid to lighter fluid) and bubble (penetration of lighter fluid to heavier fluid) are visible. Figure 4.38 is a plot of bubble and spike amplitudes versus time, where the amplitudes have been normalized by the post-shock initial amplitude h_0^+. Since the density ratio employed in this problem $>>1$, spike and bubble growth is asymmetric as observed in figure 4.38 with spikes outpacing bubble growth [95-97]. The bubble and spike amplitudes in figure 4.38 are computed with reference to the location of an unperturbed interface (dashed line in figure 4.37), which was obtained from corresponding 1D simulations. For late-time growth and mixing in the RMI, see [97, 98].
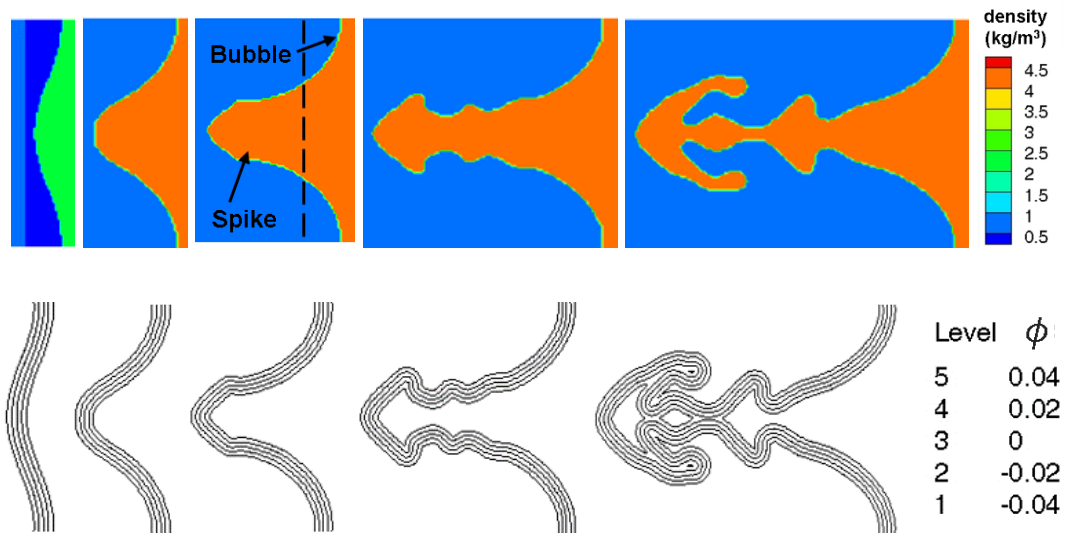
Figure 4.37. Density and LS contours in the RM problem. Interface evolution has been plotted for: $kV_0t = 0, 1, 2, 5, 10$ (from left to right). The spike and bubble are labeled. The location of the unperturbed interface is indicated by the dashed line.
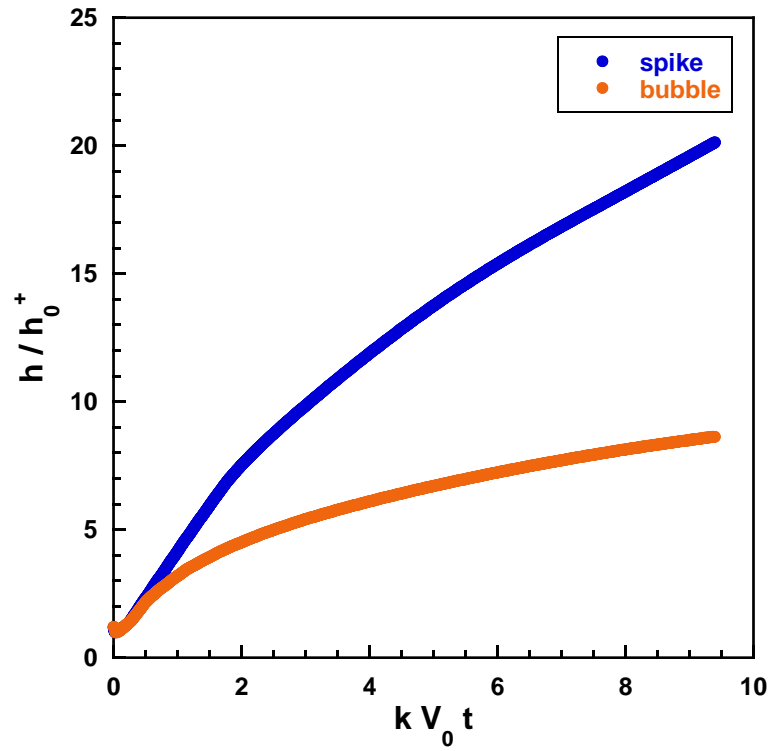
Figure 4.38. Time evolution of spike and bubble amplitudes from 2D simulations using IMPACT.

In figure 4.39 we plot the time evolution of the bubble and spike growth rates from our simulations $(V_{sp} = dh_{sp}/dt$ and $V_{bu} = dh_{bu}/dt)$, and compare the results with the nonlinear analytical model of [94]. As seen in this figure, the simulation results for bubble and spike growth rates are in excellent agreement with [94].
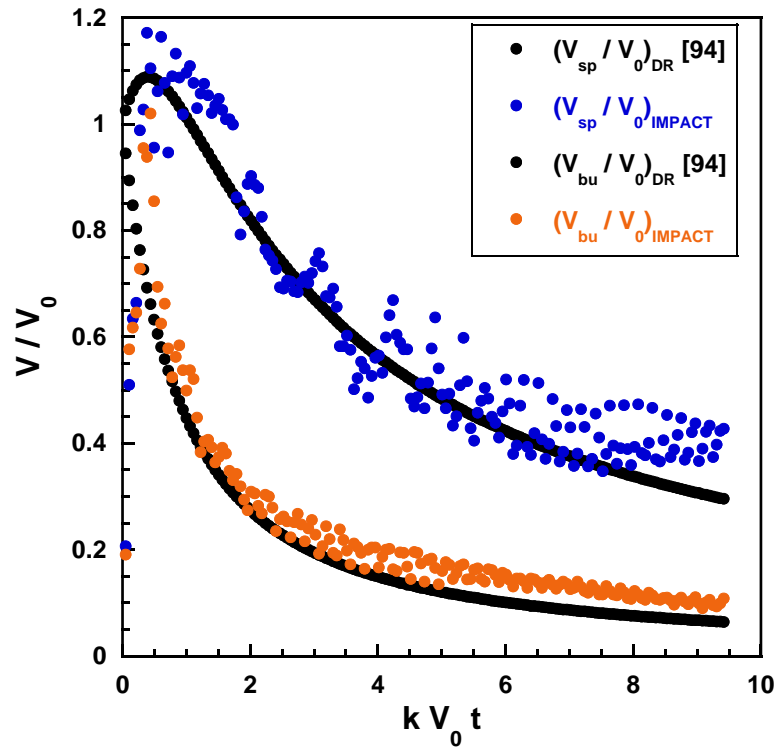
Figure 4.39. Time evolution of spike and bubble velocities. Results from IMPACT are compared with the nonlinear model of [94].

4.4 Surface tension effects on interface evolution

In §3.5, we discussed the implementation of surface tension using the GFM by modifying the interfacial boundary conditions [27], or by manipulating the exact or approximate Riemann solver for MMRP-based GFMs. In this section, we summarize results from both approaches and compare our outcomes with the analytical models in the literature for standard test cases.

4.4.1. Sod shock tube problem with prescribed pressure jump [84]: The problem statement is similar to § *4.1.1,* but with a specified pressure jump $\Delta p = 0.2$ applied to the initial discontinuity. Thus, this 1D case serves to validate the modifications to the GFM or the

multi-medium Riemann solver, implemented to handle the pressure jump associated with surface tension, without the complicating effects of interface topology encountered in multi-dimensional problems. The simulations were performed with a mesh of 200 cells and $CFL = 0.2$ to a final time of $t = 0.25$ to match the parameters used for problem *4.1.1*.

The effect of including surface tension in the Sod shock tube problem is first discussed by plotting the evolution of the contact discontinuity in the exact solutions in figure 4.40. As shown in the pressure profile, the exact multi-medium Riemann solver (discussed in §3.5) retains the prescribed pressure jump to the end of the simulation, with $p_{*L} = 0.43$, while $p_{*R} = 0.23$. Plots of the density (figure 4.40(a)) and velocity profiles (figure 4.40(b)) reveal higher interface velocity and shock speed in the absence of surface tension.
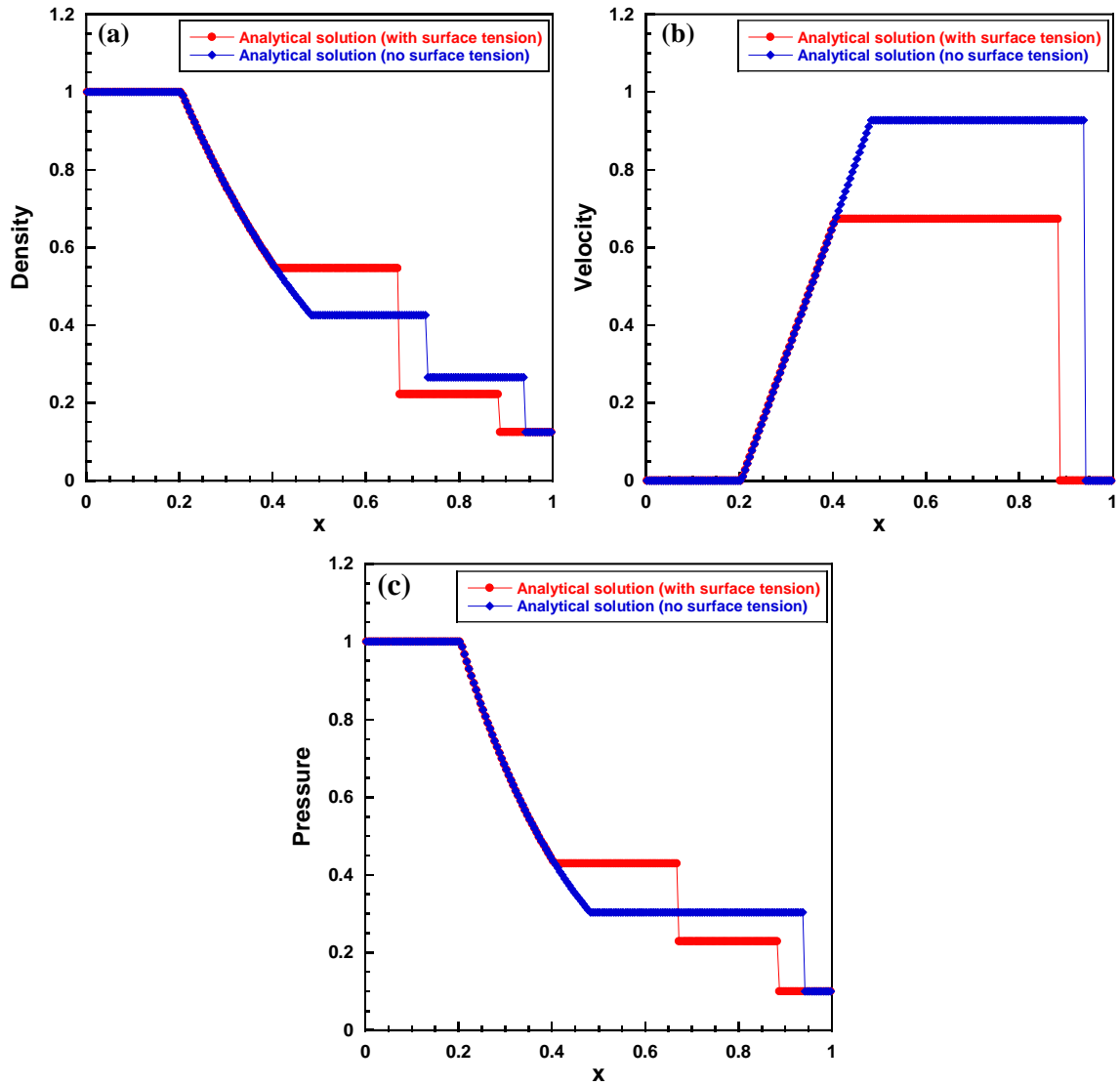
Figure 4.40. Exact solution of the Sod shock tube problem with and without pressure jump at the contact discontinuity. (a) Density, (b) velocity, and (c) pressure profiles at $t = 0.25$.

Figures 4.41 (a) – (c) show the distributions of density, velocity, and pressure at $t = 0.25$, from the different versions of the GFM implemented in IMPACT. Results from the linearized Riemann solver (LRS) [84] obtained by linearization of the MMRP at the interface are also included in the figures. The LRS is a powerful alternative to eqs. (3.12)-

(3.14) in obtaining a solution to the MMRP, since it eliminates the high computational costs associated with exact solvers [41]. However, the LRS can result in inaccurate values for strong shock-interface interactions or for problems with high density ratios across the interface [84] [84]. As seen in figure 4.41, all versions of the GFM implemented in IMPACT successfully capture the flow behavior resulting from the prescribed pressure jump $\Delta p = 0.2$ at the contact discontinuity. Furthermore, the numerical predictions for the wave speeds are in very good agreement with the results from the exact solvers and serves to validate the surface tension implementation in IMPACT through the GFM.
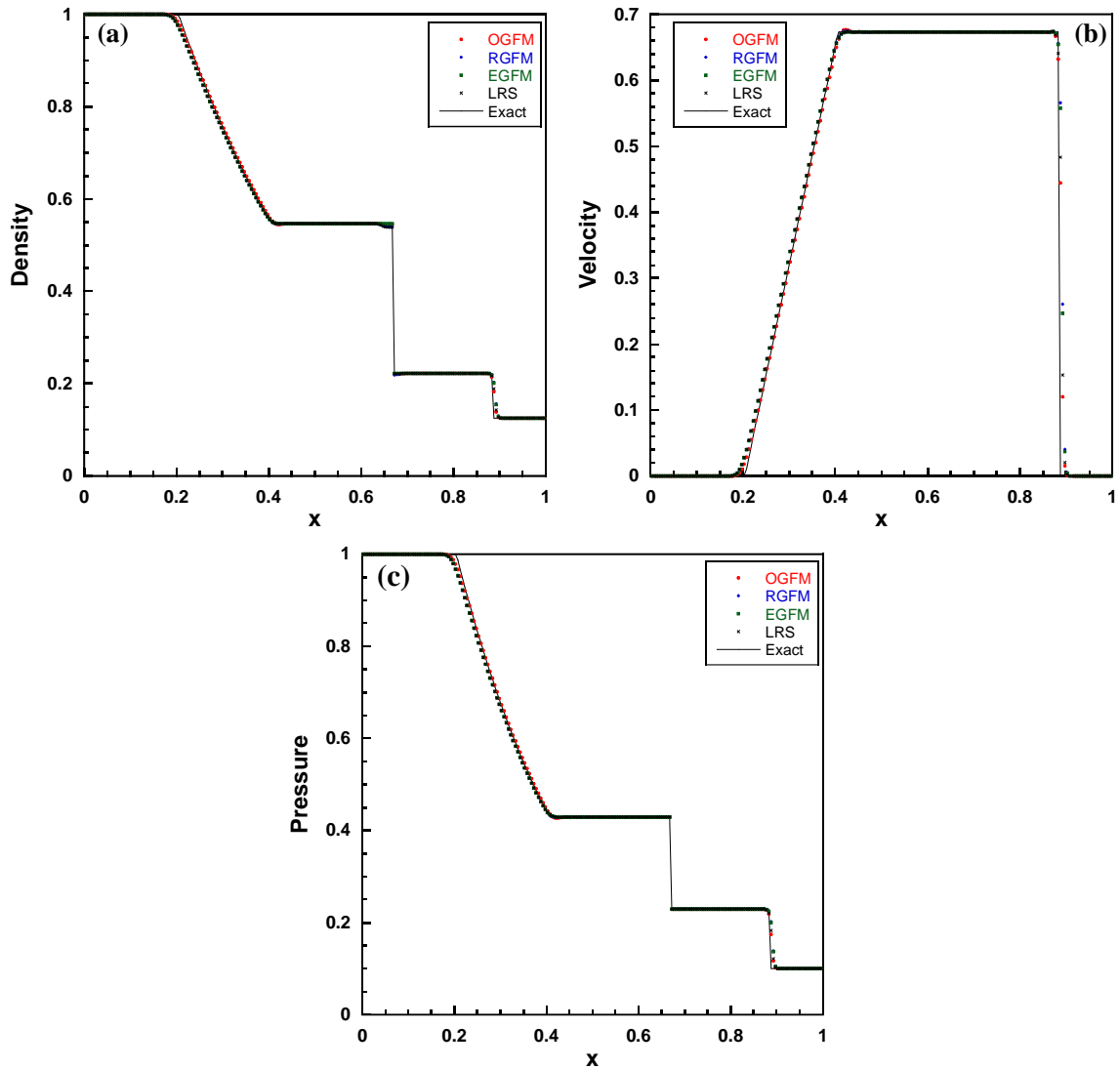
Figure 4.41. (a) Density, (b) velocity, and (c) pressure distributions for problem *4.4.1*. The prescribed pressure jump $\Delta p = 0.2$ is applied to the contact discontinuity, and solved using different versions of the GFM.

In figure 4.42, we plot details of the density and pressure profiles near the interface. The EGFM removes overheating from the interface, while all other versions of the GFM exhibit overheating errors in both the density and pressure solutions. This demonstrates the capabilities of the EGFM in simulating shock-interface problems with surface tension.
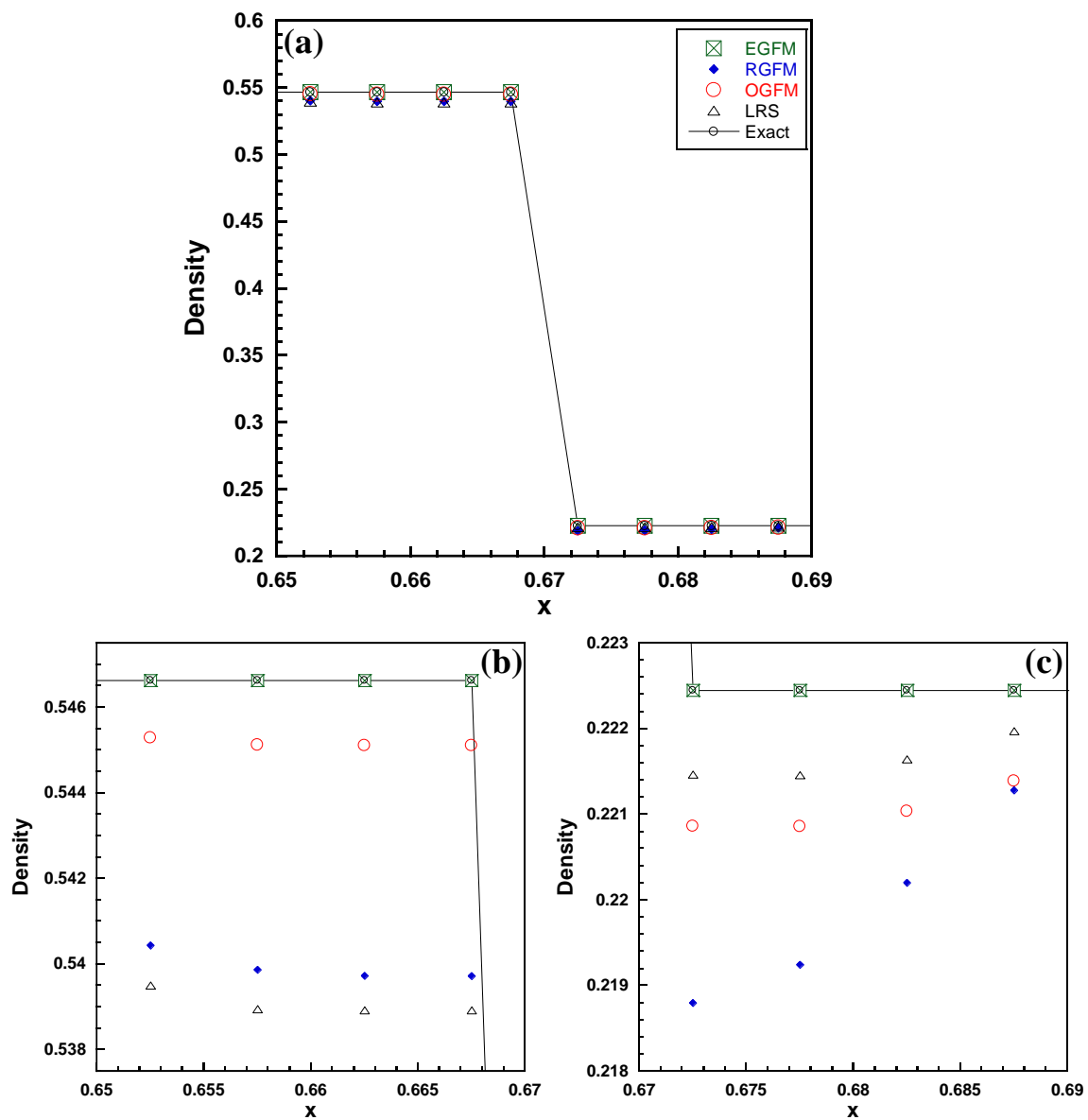
Figure 4.42. (a) Density profile near the interface. Density values to the (b) left and (c) right of the interface. The EGFM values are in excellent agreement with the exact solver.
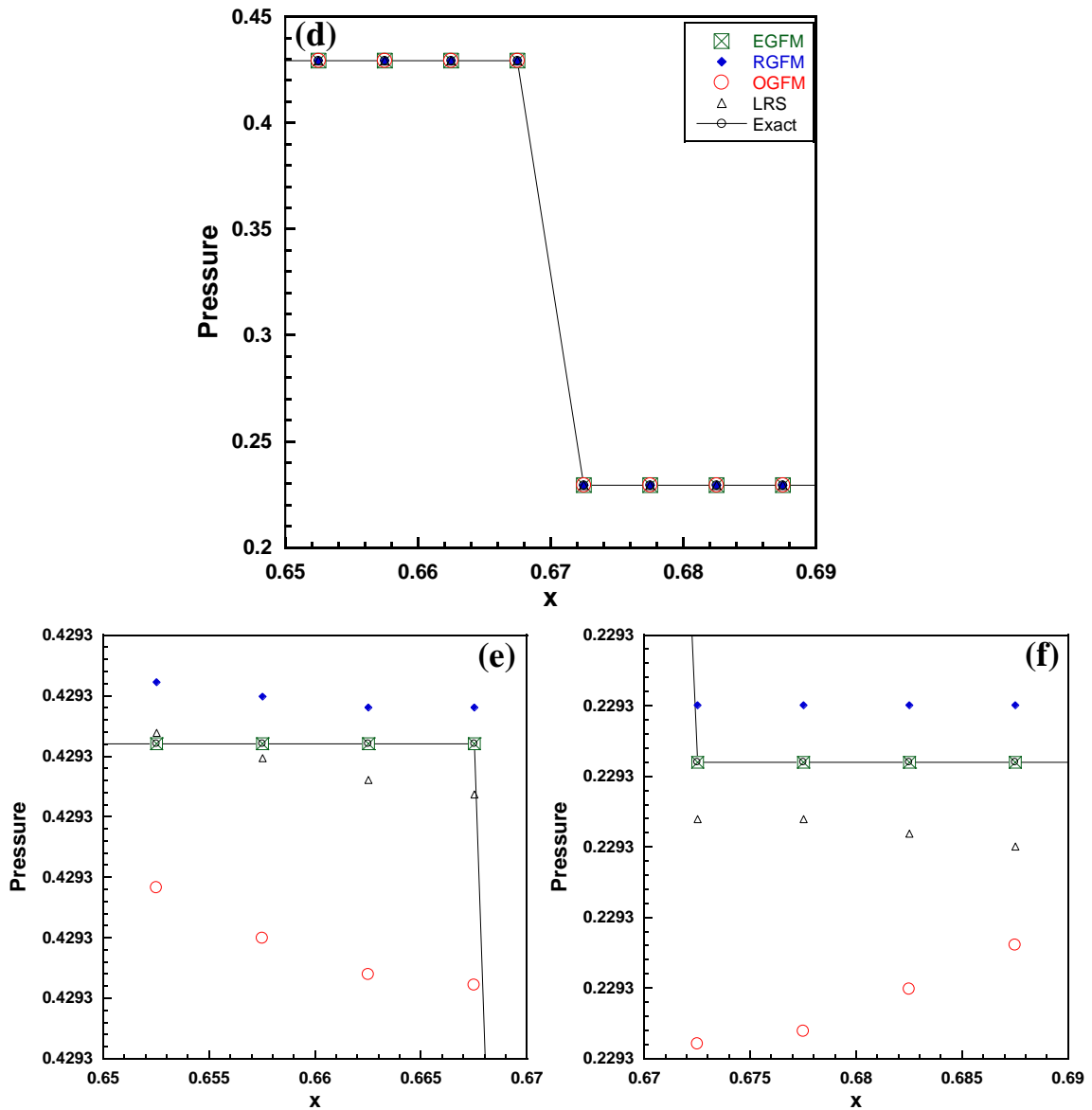
Figure 4.42 (continued). (d) Pressure profile near the interface. Pressure values to the (e) left and (f) right of the interface. The EGFM values are in excellent agreement with the exact solver.

4.4.2. Oscillating drop [31, 86]. This is a standard test problem for evaluating surface tension effects on the evolution of interfaces. A square domain of dimensions 4×4 is filled with air ($\gamma_a = 1.4$) and with a water ($\gamma_w = 4$ and $p_{\infty w} = 1$) droplet at the center of the domain. The gas-water contact is a closed elliptical interface represented by:

$$\left(\frac{x-2}{a}\right)^2 + \left(\frac{y-2}{b}\right)^2 = 1$$

where $a = 1.25$ and $b = 0.8$. The fluids are initially at rest with the following densities

and pressures:

$$W_a = (\rho_a, p_a) = (1, 1),$$

$$W_w = (\rho_w, p_w) = (5, 1).$$

Note that since $a > b$, the interface curvature at the left and right poles of the drop is

initially greater than at the top and bottom poles, resulting in a surface tension-regulated

oscillation of the drop in time. The resulting period of oscillation is given by analytical

relations [99] as follows:

$$T = 2\pi \sqrt{\frac{(\rho_a + \rho_w)r^3}{6\sigma}} \qquad\qquad (4.1)$$

where r is the equivalent circular radius and is equal to $\sqrt{ab}$, and σ is the surface tension

coefficient. In our simulations, we use $\sigma = 0.72$ resulting in a period $T = 7.4$. The

IMPACT simulations were performed using a mesh with 100 cells in each direction, while

setting $CFL = 0.4$. The modified version of the GFM [27, 66] was invoked to apply the

boundary conditions at the interface including the pressure jump due to surface tension.

Outflow boundary conditions were applied on all four boundaries, while the simulations

were run to a final time of $t = 9.44$. Following [86], the period of oscillation is deduced in

the IMPACT simulations from the global kinetic energy defined as $\frac{1}{2}\iint \rho(u^2 + v^2)\, dx\, dy$

in figure 4.43. In figure 4.44, density contours from the simulations are plotted at intervals

of $T/8$.
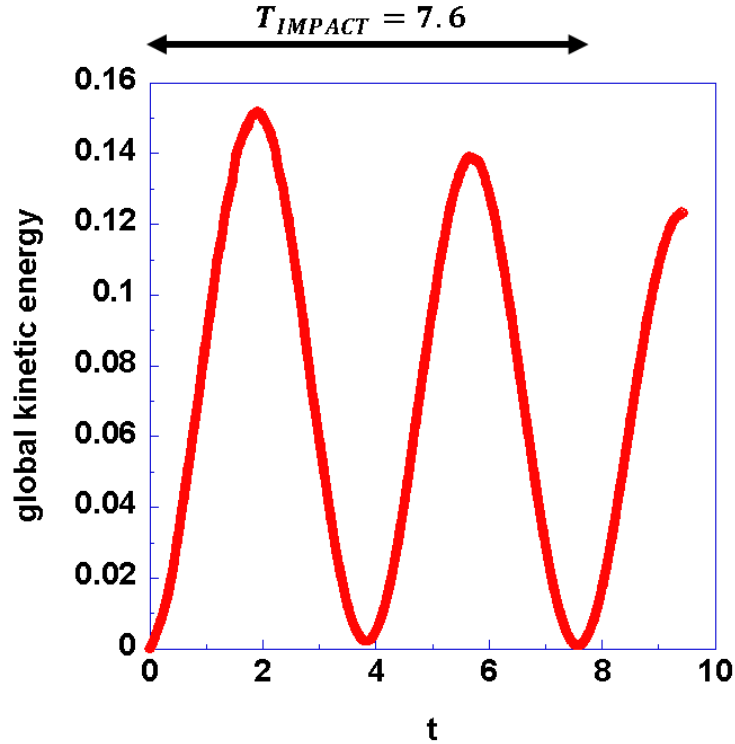
Figure 4.43. Global kinetic energy vs. time. The drop's period of oscillations from
IMPACT is 7.6.

From figure 4.43, the global kinetic energy oscillates in accordance with the droplet shape

(see figure 4.44). Furthermore, the global kinetic energy peaks decrease in time owing to

numerical dissipation in the simulations [31, 86]. The time period of oscillation estimated

from the global k.e. oscillations in figure 4.43 is $T_{IMPACT} = 7.6$, and within 2.7% of eq.

(4.1).
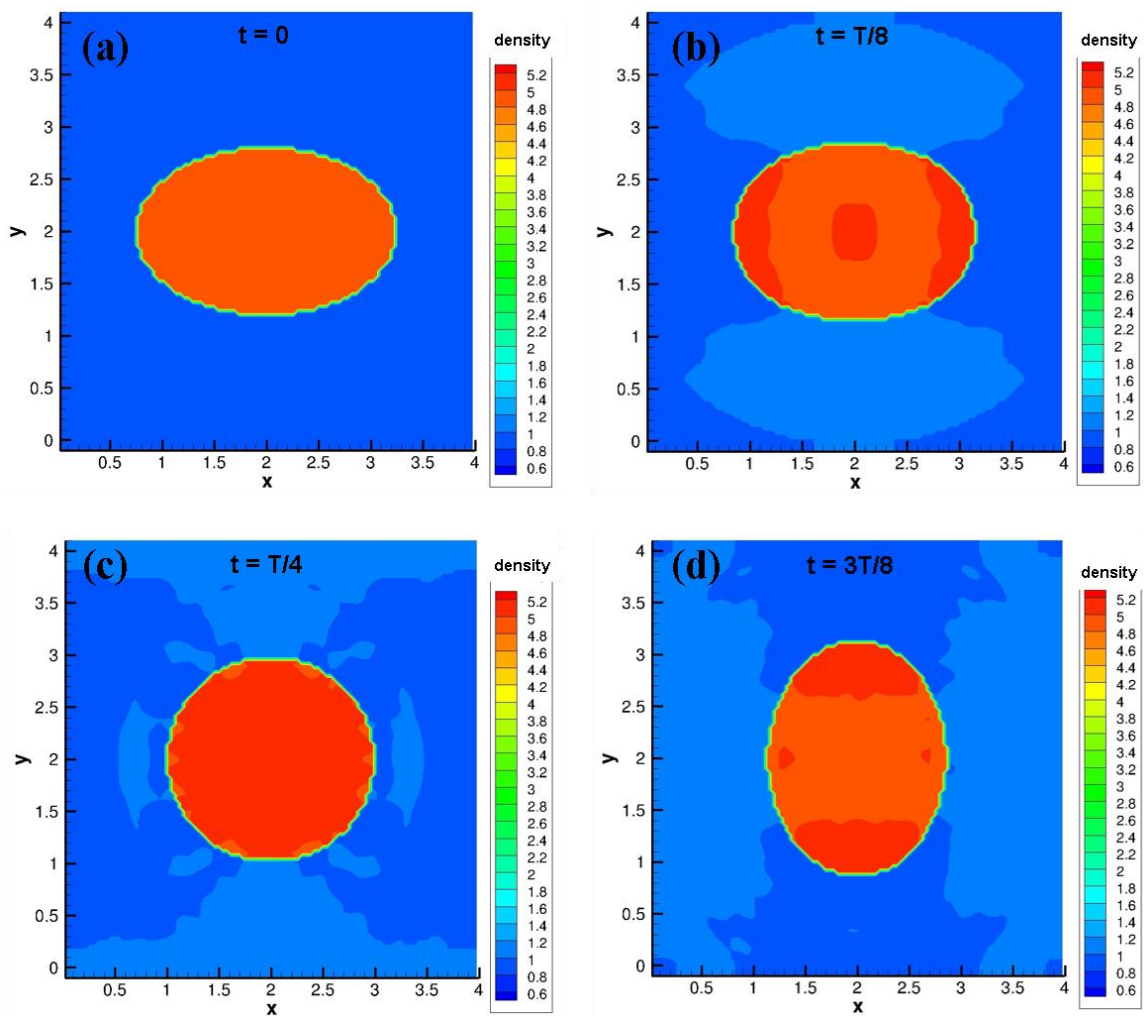
Figure 4.44. Interface evolution in the oscillating drop problem: (a) $t = 0$, (b) $t = T/8$, (c) $t = T/4$, (d) $t = 3T/8$.
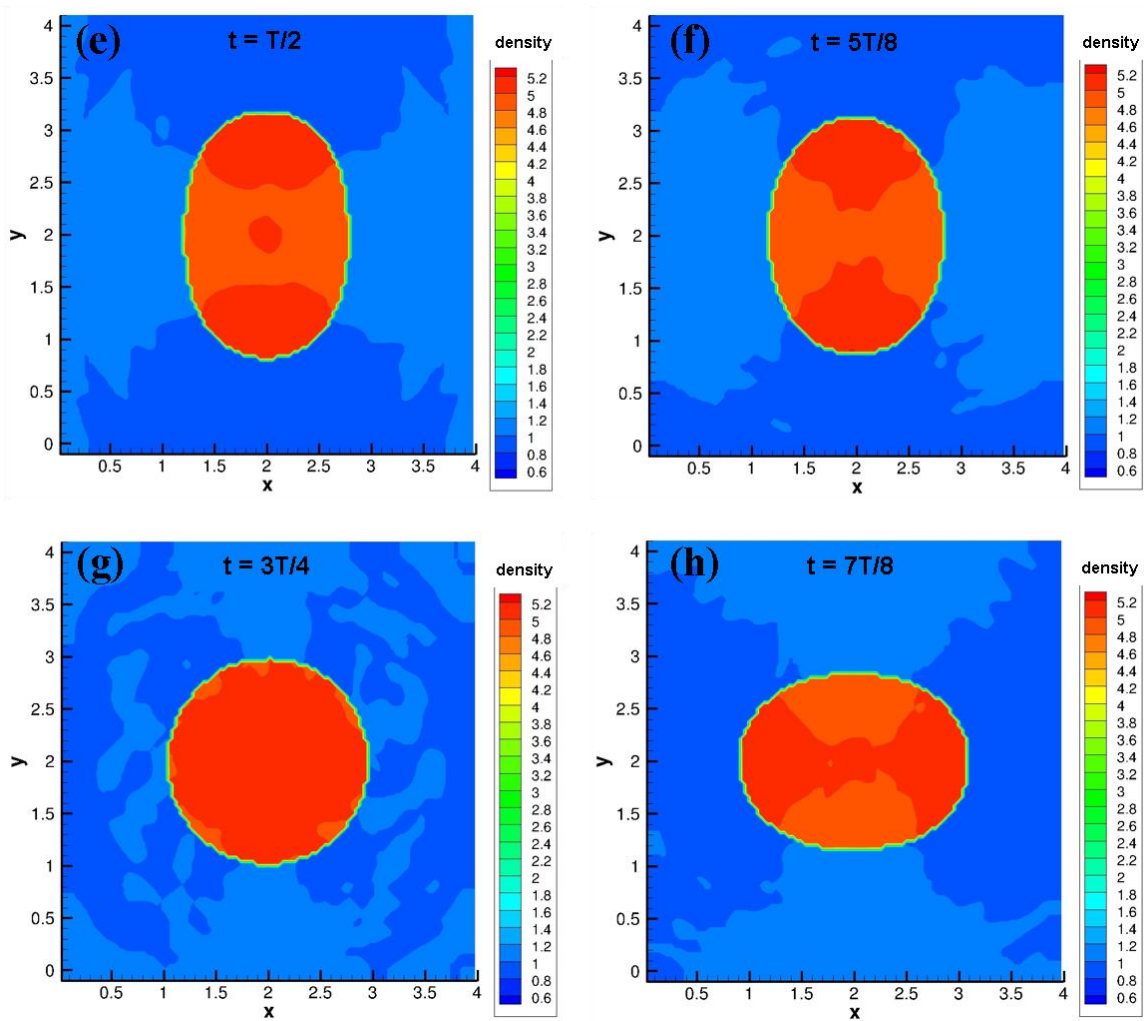
Figure 4.44 (continued). Interface evolution in the oscillating drop problem: (e) $t = T/2$, (f) $t = 5T/8$, (g) $t = 3T/4$, (h) $t = 7T/8$.
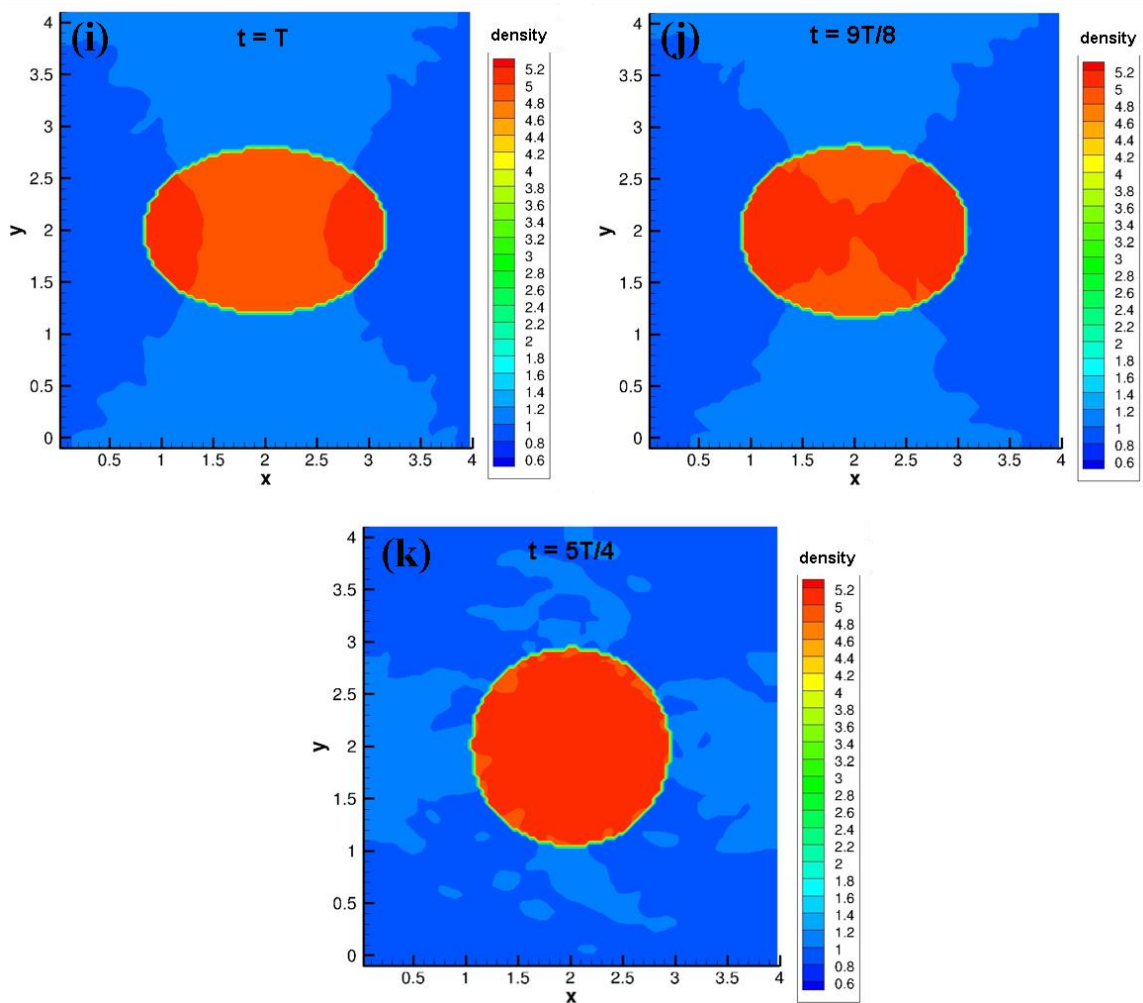
Figure 4.44 (continued). Interface evolution in the oscillating drop problem: (i) $t = T$, (j) $t = 9T/8$, (k) $t = 5T/4$.

Figure 4.44 demonstrates the evolution of the interface through density contours at different times. At $t = 0$, the simulation is initialized with a horizontal ellipse, ensuring surface tension forces are at their maximum(minimum) at the horizontal (vertical) poles owing to the highest (lowest) curvature at those points. This results in a larger pressure jump across the interface at the horizontal poles, that restores the ellipse to a circular form by $t = T/4$. At this time, surface tension forces are uniformly distributed around the circle,

while the kinetic energy is at its highest leading the drop to be stretched in the vertical direction. By $t = T/2$, the drop achieves a vertical ellipse with the maximum curvature at the north and south poles, forcing the ellipse to return to its circular shape by $t = 3T/4$ and eventually to the initial horizontal ellipse by $t = T$. This test problem demonstrates the robustness of the implemented LS capability to accurately capture the interface shape and the curvature to a high-order for surface tension calculations.

4.4.3. Shock-bubble interaction (light → heavy) under surface tension effects. The problem definition is similar to § *4.2.3,* but with surface tension imposed at the interface through modifying the boundary conditions in the OGFM. Simulations were performed with $\sigma = 100 \ N/m$ and $\sigma = 300 \ N/m$, and the results compared with problem *4.2.3* in figure 4.45. Under the effect of surface tension, both the primary (RM) and secondary (Kelvin-Helmholtz) instabilities at the density interface are significantly damped. As a result, when surface tension is included, the shocked bubble exhibits oscillatory behavior about a mean shape. Note that for $\sigma = 300 \ N/m$, the bubble undergoes significantly less deformation, maintaining its circular shape.
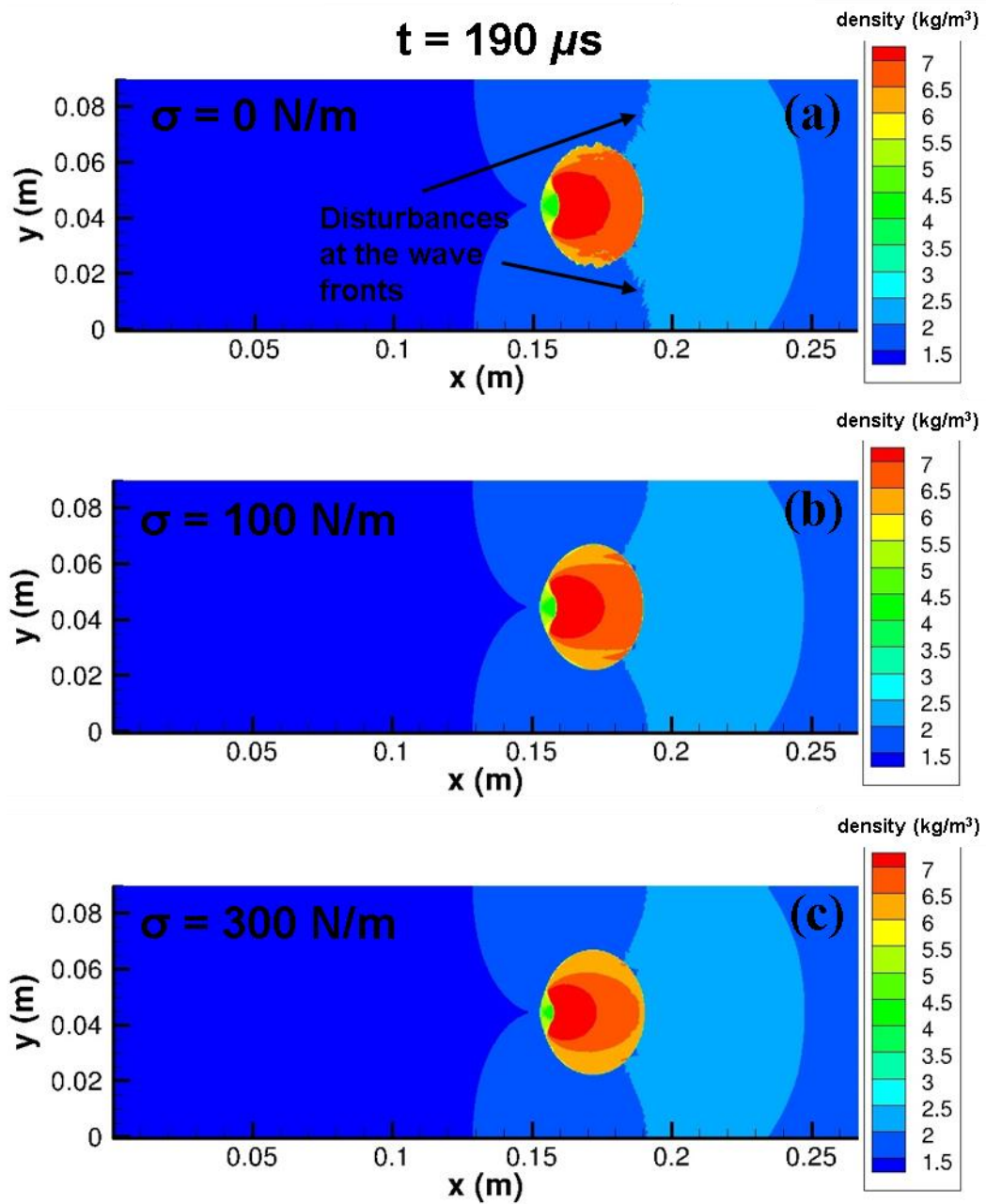
Figure 4.45. Shock-bubble interaction at $t = 190 \; \mu s$ with and without surface tension: (a) $\sigma = 0$, (b) $\sigma = 100 \; N/m$, (c) $\sigma = 300 \; N/m$. Surface tension suppresses instabilities at the interface and results in smooth wave fronts.

Figure 4.45 (continued). Shock-bubble interaction at $t = 250\ \mu s$ with and without surface tension: (d) $\sigma = 0$, (e) $\sigma = 100\ N/m$, (f) $\sigma = 300\ N/m$. Surface tension suppresses instabilities at the interface and results in smooth wave fronts.
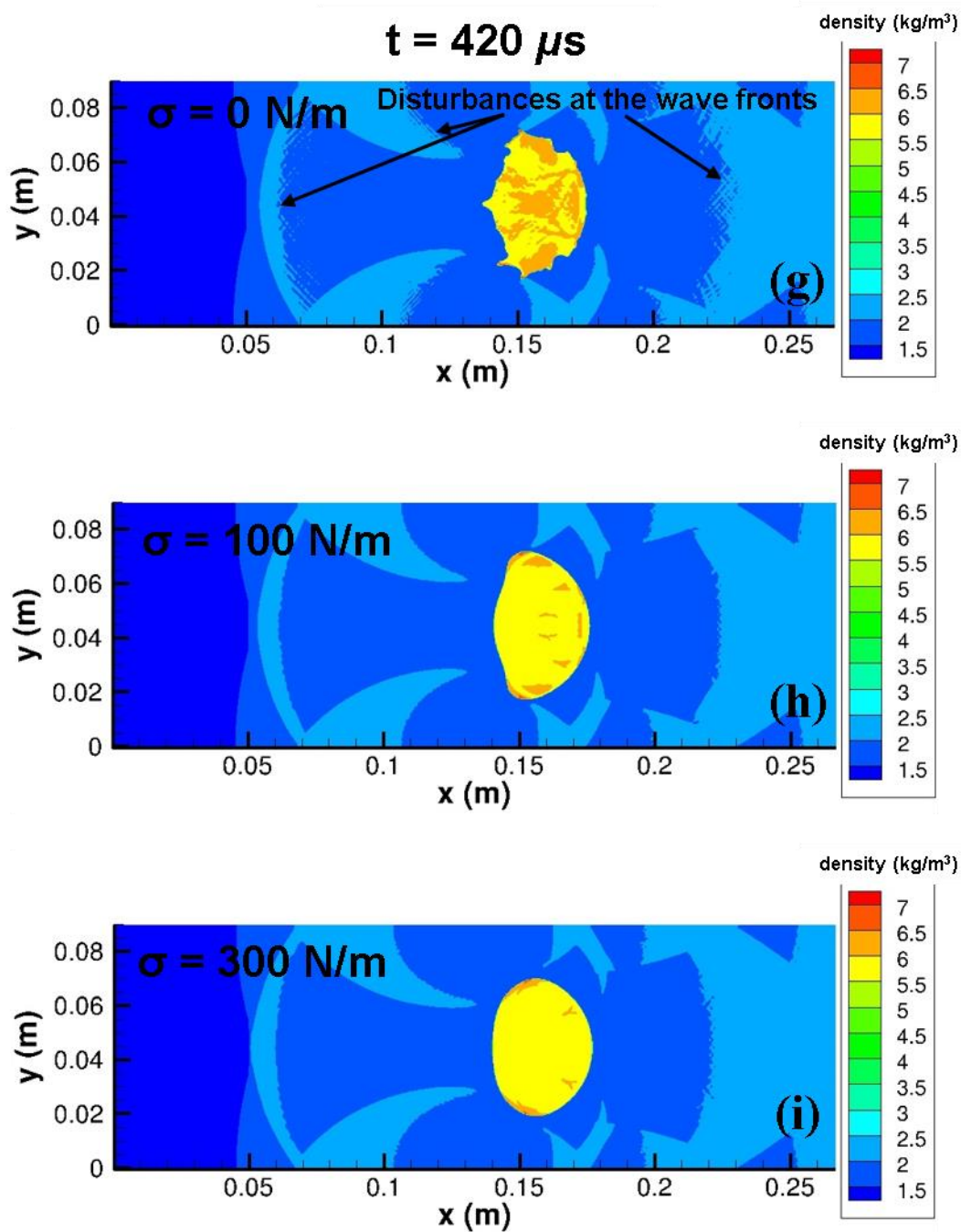
Figure 4.45 (continued). Shock-bubble interaction at $t = 420\ \mu s$ with and without surface tension: (g) $\sigma = 0$, (h) $\sigma = 100\ N/m$, (i) $\sigma = 300\ N/m$. Surface tension suppresses instabilities at the interface and results in smooth wave fronts.
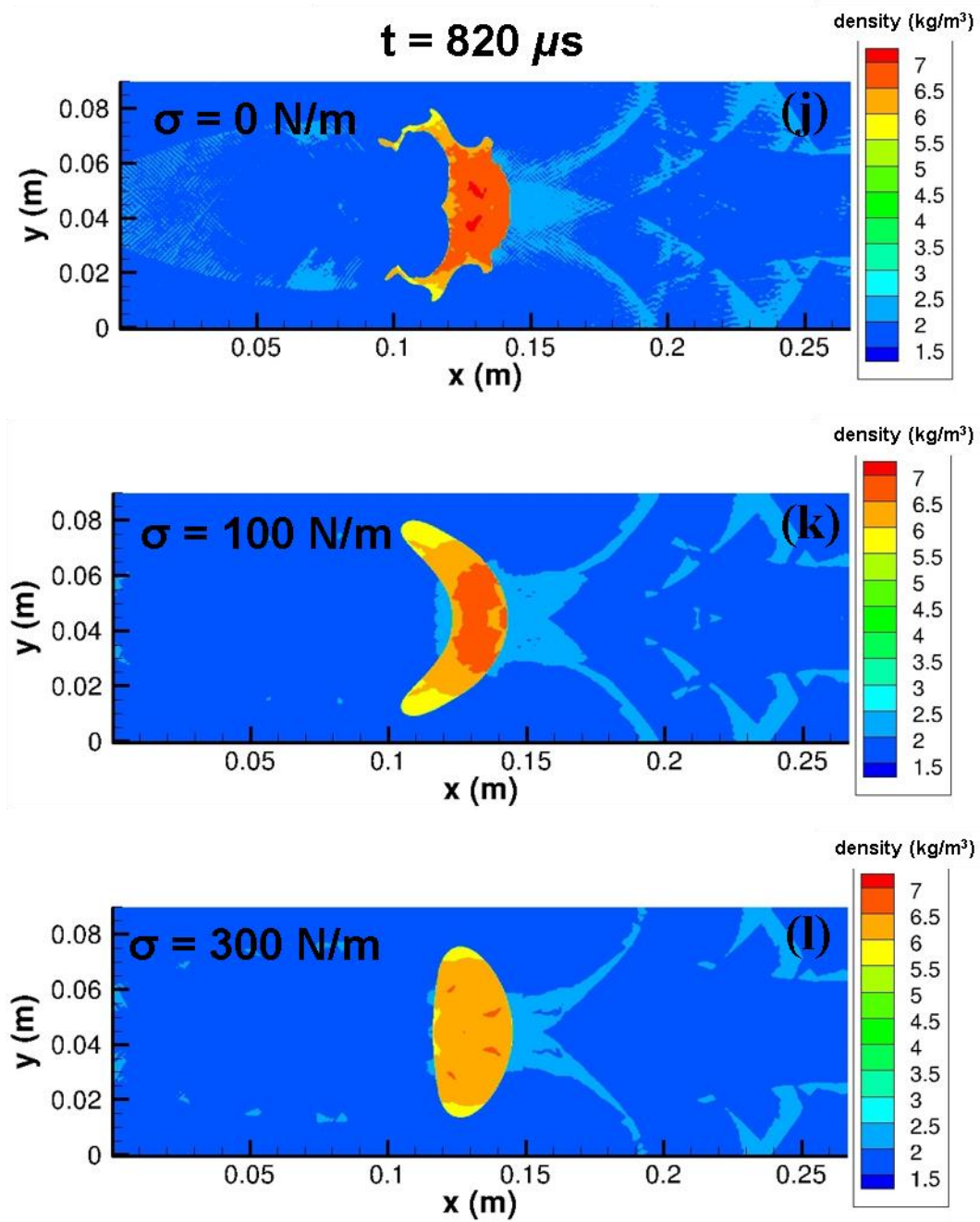
Figure 4.45 (continued). Shock-bubble interaction at $t = 820 \ \mu s$ with and without surface tension: (j) $\sigma = 0$, (k) $\sigma = 100 \ N/m$, (l) $\sigma = 300 \ N/m$. Surface tension suppresses instabilities at the interface and results in smooth wave fronts.

As the shape of the shocked bubble is modified by surface tension, the appearance of reflected and transmitted waves are also affected. In figure 4.45, when $\sigma = 0$ the wave fronts contain fine-scale features that correspond to undulations in the bubble shape. As the surface tension is increased ($\sigma = 100 \ N/m$ - $300 \ N/m$), the bubble shape becomes less corrugated, while the reflected and transmitted waves also appear smoother.

4.4.4. Richtmyer-Meshkov instability under the effect of surface tension. The problem configuration follows §4.3, with surface tension effects included at the interface. Surface tension is handled numerically using the GFM approach of [32] described in §3.5, combined with the exact multi-medium Riemann solver given in eqs. (3.12)-(3.14). In this section, the effect of surface tension on the linear growth of RMI is described using results from IMPACT simulations. In the linear regime, surface tension stabilizes RMI as predicted by the model of [19], and results in an oscillatory behavior of the interface about its mean (unperturbed) position.

The analytical model by Mikaelian [19] applies to a single-mode RMI, and predicts the time dependence of the amplitude of a perturbed interface with imposed surface tension:

$$\frac{h(t)}{h_0^+} = cos \ \omega t + \frac{\Delta v k A t^+}{\omega} sin \ \omega t \ . \tag{4.2}$$

In eq. (4.2), ω is the angular frequency of surface tension-driven oscillations and given by

$$\omega = \sqrt{\frac{k^3 \sigma}{\rho_A^+ + \rho_B^+}} \tag{4.3}$$

where ρ_A^+ and ρ_B^+ are the post-shock values of densities on either side of the interface (see figure 4.36). From eq. (4.2), the maximum perturbation amplitude [19] is obtained as:

$$h_{max} = h_0^+ \sqrt{1 + \left(\frac{kAt^+\Delta v}{\omega}\right)^2}. \tag{4.4}$$

Using equations (4.3) – (4.4), a lower limit for the surface tension can be estimated so that $kh_{max} \leq 1$ in our simulations, thereby ensuring the perturbation amplitudes in the IMPACT simulations stayed within the linear regime. Using $\rho_A^+ = 0.737 \ kg/m^3$ and $\rho_B^+ = 4.109 \ kg/m^3$ from §4.3, and the post-shock values from table 4.2, we estimate for the parameters of the problem, the RMI will remain in the linear regime for $\sigma \gtrsim \sigma_{crit} = 400 \ N/m$. Thus, for $\sigma \gtrsim \sigma_{crit}$ results from the IMPACT simulations can be compared with the model equations (4.2)-(4.4).

The evolution of the interface for $\sigma = 400 \ N/m$ is shown in figure 4.46, and exhibits an oscillatory behavior in contrast to § 4.3. The corresponding amplitude evolution (peak-to-peak) is shown in figure 4.47. Following an initial compression of the pre-shock amplitude h_0^- to h_0^+ visible in figure 4.47, an oscillatory behavior is established. The period of oscillation, and peak amplitudes are in good agreement with eqs. (4.3)-(4.4). However, a gradual decay in the maximum amplitude is observed and attributed to numerical diffusion. When the mesh resolution is doubled to 200 cells/λ, the loss in amplitude is mitigated as observed in figure 4.47.
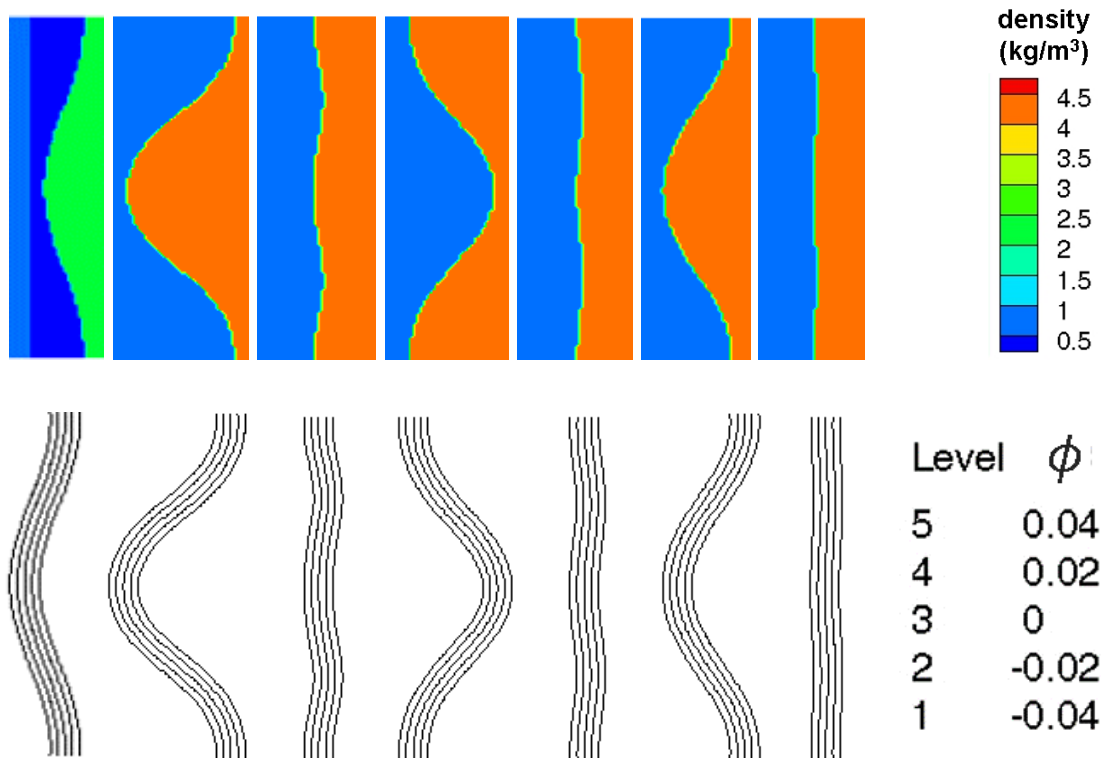
Figure 4.46. Density and LS contours for the RM problem with surface tension $\sigma = 400 \ N/m$. Interface evolution has been plotted for times corresponding to: $h(t) = h_0^-, h_{max}, 0, -h_{max}, 0, h_{max}, 0$ (from left to right). In contrast to §4.3, the RMI growth is stabilized, and the amplitude oscillates under the effect of surface tension.
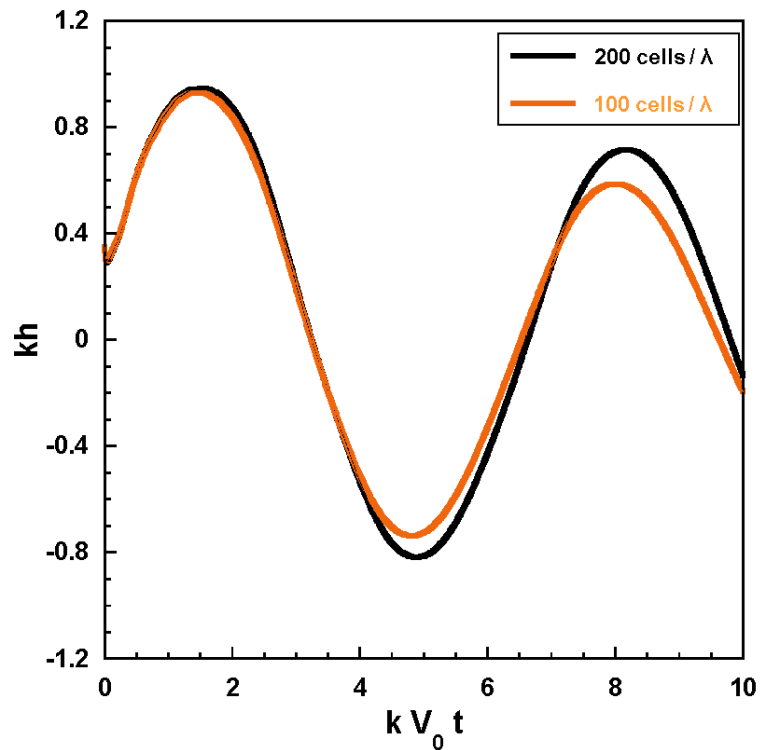
Figure 4.47. The plot of amplitude versus time for problem *4.4.4* with $\sigma = 400 \ N/m$.

The above simulations were repeated for a range of values of the surface tension, and the results are reported in figure 4.48. In particular, as the surface tension coefficient is increased systematically ($\sigma = 1145, 2035, 3180,$ and $4579 \ N/m$), lower peak saturation amplitudes and shorter periods of oscillation are observed. Once again, some attenuation of the peak amplitude h_{max} is observed due to numerical dissipation, and mitigated at higher mesh resolutions. In figure 4.49, the period of oscillation and the peak saturation amplitudes from the IMPACT simulations are compared with the analytical model of [19]. The simulation results are in close agreement with the model of [19] over a wide range of surface tension coefficients.
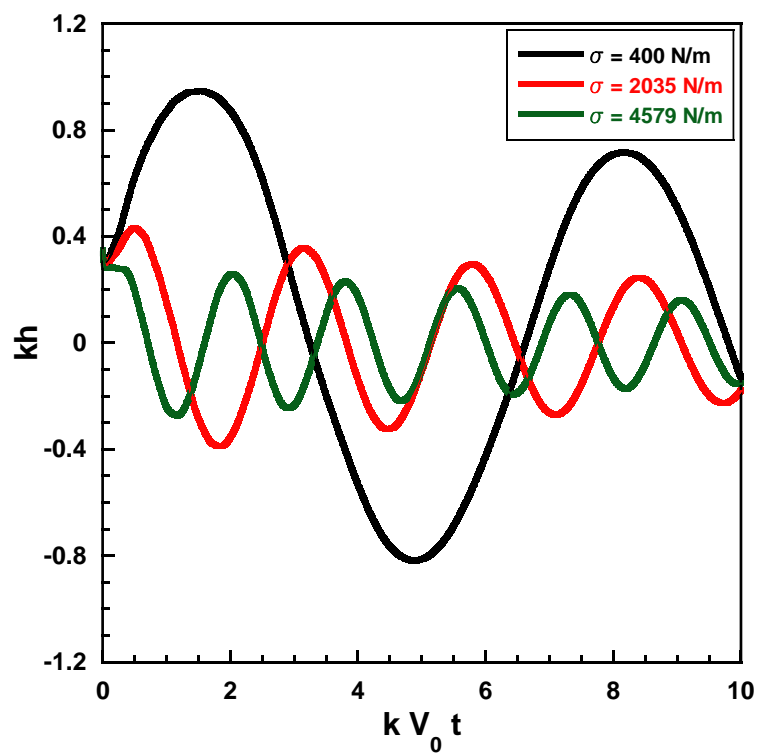
Figure 4.48. Time evolution of the RMI perturbation amplitude corresponding to different values of surface tension.
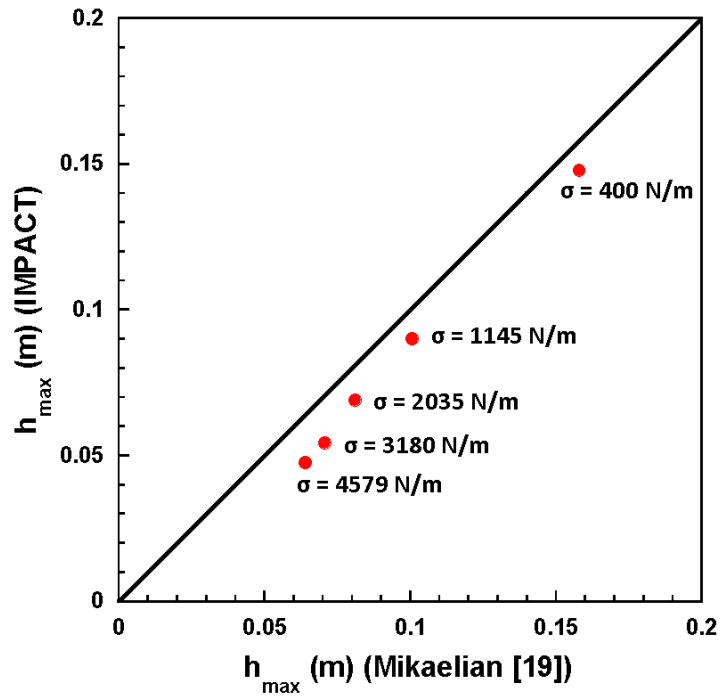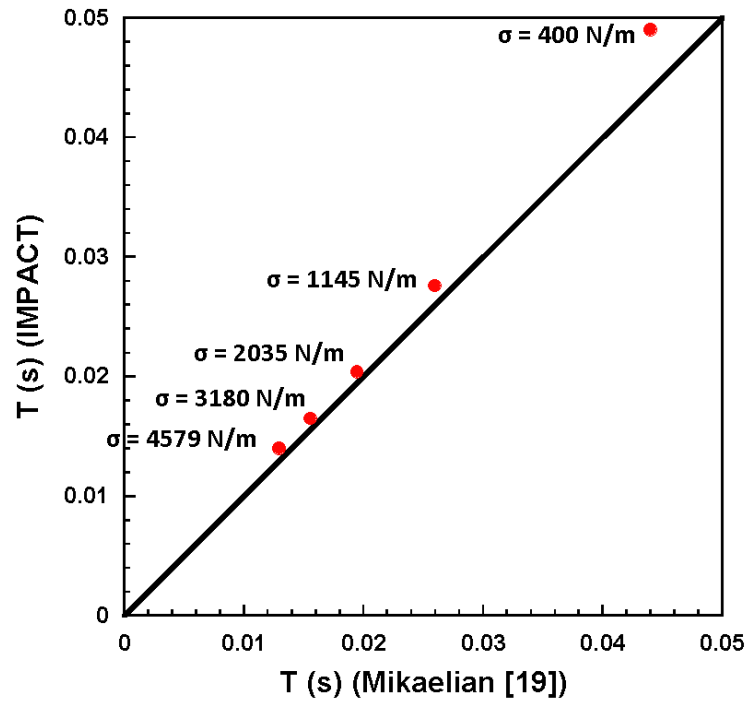
Figure 4.49. A comparison of the oscillation period and maximum amplitudes obtained from IMPACT simulations with the analytical model of Mikaelian [19].

CHAPTER 5: SUMMARY AND CONCLUSIONS

In this dissertation, we presented novel numerical methods developed to simulate complex multi-phase flows with interfaces, shock-interface interactions, interfacial instabilities, and transport properties such as surface tension. In particular, a modification of the widely used Ghost Fluid Method has been proposed to address overheating numerical errors that have been associated with the class of GFM approaches. The proposed algorithm is referred as the Efficient Ghost Fluid Method (EGFM), and is based on the GFM theorem by applying isentropic/shock relations to the cells near the interface. The EGFM was further extended to handle shock-interface interactions where both the shock and the interface were treated sharply. The EGFM has been implemented in a new shock physics Eulerian code, IMPACT, that was developed as part of this dissertation.

IMPACT solves the fully compressible Navier-Stokes/Euler equations and is capable of handling a wide range of physics including surface tension effects, shocks, multiple equations of state and phase change. These capabilities can be applied in the simulation of a broad range of engineering problems such as atomization of liquids and fuels, droplet combustion, cavitation in pumps and turbines, shock wave therapy, and material ejection. IMPACT employs highly accurate, robust, and cutting-edge numerical techniques: The Roe solver [41, 43] is used along with Harten-Hyman [44] entropy fix to solve Riemann problems at cell boundaries and determine intercell fluxes. A fifth-order WENO scheme [46, 47, 55] is used for spatial discretization and coupled with a TVD-RK [55] third-order time stepping. Interface tracking is accomplished using the LS method, in which interface normals and curvatures are calculated to high-order accuracy [53] resulting in precise

computations of surface tension forces at the interface without recourse to so-called interface surgical approaches. In addition to the EGFM approach proposed here, IMPACT also provides users with the option of choosing from OGFM, PGFM and RGFM approaches, and multiple equations of state including gamma-law, stiff gas etc.

The EGFM approach was demonstrated to consistently remove overheating errors in several standard and demanding 1D problems. The 1D problems included various single- as well as multi-component Riemann problems, such as shock tube problems, shock impedance matching problems, and problems with colliding shock waves, and various shock-interface interactions such as light-to-heavy, heavy-to-light, gas-gas and gas-water interactions. The simulations demonstrated highly accurate results from the EGFM in comparison with the OGFM and RGFM, where overheating and spurious numerical reflections were completely eliminated in all cases. The numerical methods in IMPACT were also validated for 2D problems including underwater explosion of an air bubble, a strong shock impacting on an air cavity, shock-bubble interaction, and RMI (an extension of the EGFM to 2D and corresponding implementation in the 2D version of IMPACT is planned).

The RMI 2D test problem demonstrated the capabilities of IMPACT to simulate shock-driven interfacial instabilities. The results from IMPACT indicate excellent agreement with analytical models for linear [15] and nonlinear [94] growth rates. The implementation of the level set method, surface tension effects, and multi-medium Riemann solvers were validated with multiple test problems in 2D. These included a shock tube problem with a prescribed pressure jump (as would be applied by surface tension on a curved interface), where the performance of different GFMs in applying the pressure jump interfacial

boundary condition was examined. The results from IMPACT, and the EGFM in particular showed very good agreement with the results from [84]. Among the different versions of the GFM, we found the EGFM performed the best in maintaining the density and pressure jumps across the contact discontinuity.

The surface tension implementation in IMPACT was also validated with 2D oscillating drop test problem, shock-bubble interaction with surface tension and single-mode RMI with surface tension. In contrast to classical RMI, analytical models [19] predict the linear stage of RMI growth rate is stabilized under surface tension effects. Simulations were carefully designed to ensure interface perturbation amplitude remained in the linear regime $(kh(t) \leq 1)$, by determining from the model of [19] the required surface tension σ threshold. Under such conditions, the IMPACT simulations demonstrated an oscillatory behavior for the RMI interface amplitude, with the period of oscillations (T) and peak amplitude (h_{max}) in agreement with the model of [19].

In this work, a novel numerical method, the EGFM has been developed to simulate shock-physics problems with surface tension. The proposed approach has been evaluated for several 1D problems, and has been shown to completely remove overheating errors. The applicability of this approach to 2D problems is a question of research that will be addressed in future works. These innovations have been implemented in a 2D shock physics code, IMPACT. With this framework, additional physics can be implemented in IMPACT, including evaporation, viscosity, material strength, vacuum, chemical reaction, etc. Similarly, numerical capabilities such as adaptive mesh refinement (AMR), local mesh refinement (LMR), WENO class B [48] methods, parallelization through Message Passing Interface (MPI) are being implemented.

REFERENCES

1. Attal, N. and P. Ramaprabhu, *Numerical investigation of a single-mode chemically reacting Richtmyer-Meshkov instability.* Shock Waves, 2015. **25**(4): p. 307-328.

2. Attal, N.O., *Interfacial instabilities in reacting flows.* 2016, Ann Arbor, MI: ProQuest LLC.

3. Varshochi, H., N. Attal, and P. Ramaprabhu, *Shock-Induced Mixing With Chemical Reactions Using the FLASH Code.* 2014(46216): p. V01AT07A007.

4. Ramaprabhu, P., N. Attal, and H. Varshochi, *Combustion Processes in Interfacial Instabilities*, in *Developments in Combustion Technology.* 2016, InTech.

5. Varshochi, H., *The turbulent reacting Richtmyer-Meshkov instability : a new canonical problem in non-premixed combustion.* 2016, Ann Arbor: ProQuest LLC.

6. Attal, N., et al., *Development and validation of a chemical reaction solver coupled to the FLASH code for combustion applications.* Computers & Fluids, 2015. **107**: p. 59-76.

7. Wang, Y., et al., *Simulating cavitating liquid jets using a compressible and equilibrium two-phase flow solver.* International Journal of Multiphase Flow, 2014. **63**: p. 52-67.

8. Movahed, P., et al., *Cavitation-induced damage of soft materials by focused ultrasound bursts: A fracture-based bubble dynamics model.* The Journal of the Acoustical Society of America, 2016. **140**(2): p. 1374-1386.

9. Movahed, P., et al., *Ultrasound-Induced Bubble Clusters in Tissue-Mimicking Agar Phantoms.* Ultrasound in Medicine & Biology, 2017. **43**(10): p. 2318-2328.

10. Karkhanis, V. and P. Ramaprabhu, *Ejecta velocities in twice-shocked liquid metals under extreme conditions: A hydrodynamic approach.* Matter and Radiation at Extremes, 2019. **4**(4): p. 044402.

11. Karkhanis, V., et al., *A numerical study of bubble and spike velocities in shock-driven liquid metals.* Journal of Applied Physics, 2018. **123**(2): p. 025902.

12. Karkhanis, V., et al., *Ejecta Production from Second Shock: Numerical Simulations and Experiments.* Journal of Dynamic Behavior of Materials, 2017. **3**(2): p. 265-279.

13. Rayleigh, L., *Investigation of the character of the equilibrium of an incompressible heavy fluid of variable density.* Proceedings of the London Mathematical Society, 1883. **14**.

14. Taylor, G.I., *The instability of liquid surfaces when accelerated in a direction perpendicular to their planes. I.* 1950. **201**(1065): p. 192-196.

15. Richtmyer, R.D., *Taylor instability in shock acceleration of compressible fluids.* Communications on Pure and Applied Mathematics, 1960. **13**(2): p. 297-319.

16. Meshkov, E.E., *Instability of the interface of two gases accelerated by a shock wave.* Fluid Dynamics, 1969. **4**(5): p. 101-104.

17. Mikaelian, K.O., *Effect of viscosity on Rayleigh-Taylor and Richtmyer-Meshkov instabilities.* Physical Review E, 1993. **47**(1): p. 375-383.

18. Liu, T.G., B. Khoo, and W.F. Xie, *The modified Ghost Fluid Method as applied to extreme fluid-structure interaction in the presence of cavitation.* Vol. 1. 2006.

19.   Mikaelian, K.O., *Rayleigh-Taylor and Richtmyer-Meshkov instabilities in multilayer fluids with surface tension.* Physical Review A, 1990. **42**(12): p. 7211-7225.

20.   Garrick, D.P., W.A. Hagen, and J.D. Regele, *An interface capturing scheme for modeling atomization in compressible flows.* Journal of Computational Physics, 2017. **344**: p. 260-280.

21.   Takayama, K. and D. Igra, *INVESTIGATION OF AERODYNAMIC BREAKUP OF A CYLINDRICAL WATER DROPLET.* 2001. **11**(2): p. 20.

22.   Lee, J., K.-C. Lin, and D. Eklund, *Challenges in Fuel Injection for High-Speed Propulsion Systems.* AIAA Journal, 2015. **53**(6): p. 1405-1423.

23.   Meng, J.C. and T. Colonius, *Numerical simulations of the early stages of high-speed droplet breakup.* Shock Waves, 2015. **25**(4): p. 399-414.

24.   Osher, S. and J.A. Sethian, *Fronts propagating with curvature-dependent speed: Algorithms based on Hamilton-Jacobi formulations.* Journal of Computational Physics, 1988. **79**(1): p. 12-49.

25.   Osher, S. and R. P. Fedkiw, *The Level Set Methods and Dynamic Implicit Surfaces*. Vol. 57. 2004. xiv+273.

26.   Fedkiw, R.P., et al., *A Non-oscillatory Eulerian Approach to Interfaces in Multimaterial Flows (the Ghost Fluid Method).* Journal of Computational Physics, 1999. **152**(2): p. 457-492.

27.   Caiden, R., R.P. Fedkiw, and C. Anderson, *A Numerical Method for Two-Phase Flow Consisting of Separate Compressible and Incompressible Regions.* Journal of Computational Physics, 2001. **166**(1): p. 1-27.

28.   Kang, M., R.P. Fedkiw, and X.-D. Liu, *A Boundary Condition Capturing Method for Multiphase Incompressible Flow.* Journal of Scientific Computing, 2000. **15**(3): p. 323-360.

29.   Hu, X.Y., N.A. Adams, and G. Iaccarino, *On the HLLC Riemann solver for interface interaction in compressible multi-fluid flow.* Journal of Computational Physics, 2009. **228**(17): p. 6572-6589.

30.   Shukla, R.K., C. Pantano, and J.B. Freund, *An interface capturing method for the simulation of multi-phase compressible flows.* Journal of Computational Physics, 2010. **229**(19): p. 7411-7439.

31.   Shukla, R.K., *Nonlinear preconditioning for efficient and accurate interface capturing in simulation of multicomponent compressible flows.* Journal of Computational Physics, 2014. **276**: p. 508-540.

32.   Sambasivan, S.K. and H.S. UdayKumar, *Ghost Fluid Method for Strong Shock Interactions Part 1: Fluid-Fluid Interfaces.* AIAA Journal, 2009. **47**(12): p. 2907-2922.

33.   Sambasivan, S.K. and H.S. UdayKumar, *Ghost Fluid Method for Strong Shock Interactions Part 2: Immersed Solid Boundaries.* AIAA Journal, 2009. **47**(12): p. 2923-2937.

34.   Nourgaliev, R.R., T.N. Dinh, and T.G. Theofanous, *The Characteristics-Based Matching (CBM) Method for Compressible Flow With Moving Boundaries and Interfaces.* Journal of Fluids Engineering, 2004. **126**(4): p. 586-604.

35. Fedkiw, R.P., A. Marquina, and B. Merriman, *An Isobaric Fix for the Overheating Problem in Multimaterial Compressible Flows.* Journal of Computational Physics, 1999. **148**(2): p. 545-578.

36. Liu, T.G., B.C. Khoo, and K.S. Yeo, *Ghost fluid method for strong shock impacting on material interface.* Journal of Computational Physics, 2003. **190**(2): p. 651-681.

37. Hu, X.Y. and B.C. Khoo, *An interface interaction method for compressible multifluids.* Journal of Computational Physics, 2004. **198**(1): p. 35-64.

38. Wang, C., T. Liu, and B. Khoo, *A Real Ghost Fluid Method for the Simulation of Multimedium Compressible Flow.* SIAM Journal on Scientific Computing, 2006. **28**(1): p. 278-302.

39. Xu, L., C. Feng, and T. Liu, *Practical Techniques in Ghost Fluid Method for Compressible Multi-Medium Flows.* Communications in Computational Physics, 2016. **20**(3): p. 619-659.

40. Xu, L. and T. Liu, *Accuracies and conservation errors of various ghost fluid methods for multi-medium Riemann problem.* Journal of Computational Physics, 2011. **230**(12): p. 4975-4990.

41. Toro, E.F., *Riemann solvers and numerical methods for fluid dynamics: a practical introduction.* 2013: Springer Science & Business Media.

42. Godunov, S., K. and I. Bohachevsky, *Finite difference method for numerical computation of discontinuous solutions of the equations of fluid dynamics.* 1959. **47(89)**(3): p. 271-306.

43. Roe, P.L., *Approximate Riemann solvers, parameter vectors, and difference schemes.* Journal of Computational Physics, 1981. **43**(2): p. 357-372.

44. Harten, A. and J.M. Hyman, *Self adjusting grid methods for one-dimensional hyperbolic conservation laws.* Journal of Computational Physics, 1983. **50**(2): p. 235-269.

45. Liu, X.-D., S. Osher, and T.J.J.o.c.p. Chan, *Weighted essentially non-oscillatory schemes.* 1994. **115**(1): p. 200-212.

46. Jiang, G.-S. and C.-W. Shu, *Efficient Implementation of Weighted ENO Schemes.* Journal of Computational Physics, 1996. **126**(1): p. 202-228.

47. Shu, C.-W., *High Order Weighted Essentially Nonoscillatory Schemes for Convection Dominated Problems.* SIAM Review, 2009. **51**(1): p. 82-126.

48. Zhang, R., M. Zhang, and C.-W. Shu, *On the Order of Accuracy and Numerical Performance of Two Classes of Finite Volume WENO Schemes.* Communications in Computational Physics, 2011. **9**(3): p. 807-827.

49. Sussman, M., P. Smereka, and S. Osher, *A Level Set Approach for Computing Solutions to Incompressible Two-Phase Flow.* Journal of Computational Physics, 1994. **114**(1): p. 146-159.

50. Jiang, G. and D. Peng, *Weighted ENO Schemes for Hamilton--Jacobi Equations.* SIAM Journal on Scientific Computing, 2000. **21**(6): p. 2126-2143.

51. Peng, D., et al., *A PDE-Based Fast Local Level Set Method.* Journal of Computational Physics, 1999. **155**(2): p. 410-438.

52. Gibou, F., R. Fedkiw, and S. Osher, *A review of level-set methods and some recent applications.* Journal of Computational Physics, 2018. **353**: p. 82-109.

53. du Chéné, A., C. Min, and F. Gibou, *Second-Order Accurate Computation of Curvatures in a Level Set Framework Using Novel High-Order Reinitialization Schemes.* Journal of Scientific Computing, 2008. **35**(2): p. 114-131.

54. Russo, G. and P. Smereka, *A Remark on Computing Distance Functions.* Journal of Computational Physics, 2000. **163**(1): p. 51-67.

55. Shu, C.-W. and S. Osher, *Efficient implementation of essentially non-oscillatory shock-capturing schemes.* Journal of Computational Physics, 1988. **77**(2): p. 439-471.

56. Harvie, D.J.E., M.R. Davidson, and M. Rudman, *An analysis of parasitic current generation in Volume of Fluid simulations.* Applied Mathematical Modelling, 2006. **30**(10): p. 1056-1066.

57. Abgrall, R. and S. Karni, *Computations of Compressible Multifluids.* Journal of Computational Physics, 2001. **169**(2): p. 594-623.

58. Shyue, K.-M., *An Efficient Shock-Capturing Algorithm for Compressible Multicomponent Problems.* Journal of Computational Physics, 1998. **142**(1): p. 208-242.

59. Mulder, W., S. Osher, and J.A. Sethian, *Computing interface motion in compressible gas dynamics.* Journal of Computational Physics, 1992. **100**(2): p. 209-228.

60. Fedkiw, R.P., T. Aslam, and S. Xu, *The Ghost Fluid Method for Deflagration and Detonation Discontinuities.* Journal of Computational Physics, 1999. **154**(2): p. 393-427.

61. Liu, X.-D., R.P. Fedkiw, and M. Kang, *A Boundary Condition Capturing Method for Poisson's Equation on Irregular Domains.* Journal of Computational Physics, 2000. **160**(1): p. 151-178.

62. Aanjaneya, M., S. Patkar, and R. Fedkiw, *A monolithic mass tracking formulation for bubbles in incompressible flow.* Journal of Computational Physics, 2013. **247**: p. 17-61.

63. Nguyen, D.Q., R.P. Fedkiw, and M. Kang, *A Boundary Condition Capturing Method for Incompressible Flame Discontinuities.* Journal of Computational Physics, 2001. **172**(1): p. 71-98.

64. Gibou, F., et al., *A level set based sharp interface method for the multiphase incompressible Navier–Stokes equations with phase change.* Journal of Computational Physics, 2007. **222**(2): p. 536-555.

65. Merkle, C. and C. Rohde, *The sharp-interface approach for fluids with phase change: Riemann problems and ghost fluid techniques.* ESAIM: Mathematical Modelling and Numerical Analysis, 2007. **41**(6): p. 1089-1123.

66. Fedkiw, R.P., *Coupling an Eulerian Fluid Calculation to a Lagrangian Solid Calculation with the Ghost Fluid Method.* Journal of Computational Physics, 2002. **175**(1): p. 200-224.

67. Terashima, H. and G. Tryggvason, *A front-tracking/ghost-fluid method for fluid interfaces in compressible flows.* Journal of Computational Physics, 2009. **228**(11): p. 4012-4037.

68.   Terashima, H. and G. Tryggvason, *A front-tracking method with projected interface conditions for compressible multi-fluid flows.* Computers & Fluids, 2010. **39**(10): p. 1804-1814.

69.   Bo, W., et al., *A Robust Front Tracking Method: Verification and Application to Simulation of the Primary Breakup of a Liquid Jet.* SIAM Journal on Scientific Computing, 2011. **33**(4): p. 1505-1524.

70.   Gibou, F., et al., *A Level Set Approach for the Numerical Simulation of Dendritic Growth.* Journal of Scientific Computing, 2003. **19**(1): p. 183-199.

71.   Gibou, F. and R. Fedkiw, *A fourth order accurate discretization for the Laplace and heat equations on arbitrary domains, with applications to the Stefan problem.* Journal of Computational Physics, 2005. **202**(2): p. 577-601.

72.   Desjardins, O., V. Moureau, and H. Pitsch, *An accurate conservative level set/ghost fluid method for simulating turbulent atomization.* Journal of Computational Physics, 2008. **227**(18): p. 8395-8416.

73.   Koren, B., et al., *Riemann-Problem and Level-Set Approaches for Homentropic Two-Fluid Flow Computations.* Journal of Computational Physics, 2002. **181**(2): p. 654-674.

74.   Arienti, M., et al., *A level set approach to Eulerian–Lagrangian coupling.* Journal of Computational Physics, 2003. **185**(1): p. 213-251.

75.   Grétarsson, J.T., N. Kwatra, and R. Fedkiw, *Numerically stable fluid–structure interactions between compressible flow and solid structures.* Journal of Computational Physics, 2011. **230**(8): p. 3062-3084.

76.   Nguyen, D., F. Gibou, and R. Fedkiw. *A fully conservative ghost fluid method and stiff detonation waves*. in *12th Int. Detonation Symposium, San Diego, CA*. 2002.

77.   Liu, T.G., B.C. Khoo, and K.S. Yeo, *The simulation of compressible multi-medium flow. I. A new methodology with test applications to 1D gas–gas and gas–water cases.* Computers & Fluids, 2001. **30**(3): p. 291-314.

78.   Liu, T.G., B.C. Khoo, and K.S. Yeo, *The simulation of compressible multi-medium flow: II. Applications to 2D underwater shock refraction.* Computers & Fluids, 2001. **30**(3): p. 315-337.

79.   Liu, T.G., B.C. Khoo, and C.W. Wang, *The ghost fluid method for compressible gas–water simulation.* Journal of Computational Physics, 2005. **204**(1): p. 193-221.

80.   Liu, T.G. and B.C. Khoo, *The accuracy of the modified ghost fluid method for gas–gas Riemann problem.* Applied Numerical Mathematics, 2007. **57**(5): p. 721-733.

81.   Hu, X., B. Khoo, and N. Adams. *A smoothed interface interaction method for compressible flow*. in *The 25th International Symposium on Shock Waves, Bangalore, July*. 2005.

82.   Sambasivan, S.K. and H.S. UdayKumar, *Sharp interface simulations with Local Mesh Refinement for multi-material dynamics in strongly shocked flows.* Computers & Fluids, 2010. **39**(9): p. 1456-1479.

83.   Das, P. and H.S. Udaykumar, *A sharp-interface method for the simulation of shock-induced vaporization of droplets.* Journal of Computational Physics, 2020. **405**: p. 109005.

84.   Fechter, S., F. Jaegle, and V. Schleper, *Exact and approximate Riemann solvers at phase boundaries.* Computers & Fluids, 2013. **75**: p. 112-126.

85.   Jaegle, F., C. Rohde, and C. Zeiler. *A multiscale method for compressible liquid-vapor flow with surface tension*. in *ESAIM: Proceedings*. 2012. EDP Sciences.

86.   Garrick, D.P., M. Owkes, and J.D. Regele, *A finite-volume HLLC-based scheme for compressible interfacial flows with surface tension*. Journal of Computational Physics, 2017. **339**: p. 46-67.

87.   Aslam, T.D., *A partial differential equation approach to multidimensional extrapolation*. Journal of Computational Physics, 2004. **193**(1): p. 349-355.

88.   Sod, G.A., *A survey of several finite difference methods for systems of nonlinear hyperbolic conservation laws*. Journal of Computational Physics, 1978. **27**(1): p. 1-31.

89.   Chen, H. and S.M. Liang, *Flow visualization of shock/water column interactions*. Shock Waves, 2008. **17**(5): p. 309-321.

90.   Nourgaliev, R., N. Dinh, and T. Theofanous. *Direct numerical simulation of compressible multiphase flows: interaction of shock waves with dispersed multimaterial media*. in *In: CD-ROM Proceedings of the 5th International Conference on Multiphase Flow, ICMF04*. 2004. Citeseer.

91.   LeVeque, R.J. and K.-M. Shyue, *One-Dimensional Front Tracking Based on High Resolution Wave Propagation Methods*. SIAM Journal on Scientific Computing, 1995. **16**(2): p. 348-377.

92.   Mikaelian, K.O., *Freeze-out and the effect of compressibility in the Richtmyer–Meshkov instability*. Physics of Fluids, 1994. **6**(1): p. 356-368.

93.   R. Courant, K.O.F., *Supersonic Flow and Shock Waves*. Applied Mathematical Sciences. 1976: Springer-Verlag New York.

94.   Dimonte, G. and P. Ramaprabhu, *Simulations and model of the nonlinear Richtmyer–Meshkov instability*. Physics of Fluids, 2010. **22**(1): p. 014104.

95.   Dimonte, G. and M. Schneider, *Density ratio dependence of Rayleigh–Taylor mixing for sustained and impulsive acceleration histories*. Physics of Fluids, 2000. **12**(2): p. 304-321.

96.   Alon, U., et al., *Power Laws and Similarity of Rayleigh-Taylor and Richtmyer-Meshkov Mixing Fronts at All Density Ratios*. Physical Review Letters, 1995. **74**(4): p. 534-537.

97.   Thornber, B., et al., *Late-time growth rate, mixing, and anisotropy in the multimode narrowband Richtmyer–Meshkov instability: The θ-group collaboration*. Physics of Fluids, 2017. **29**(10): p. 105107.

98.   Thornber, B., et al., *Turbulent transport and mixing in the multimode narrowband Richtmyer-Meshkov instability*. Physics of Fluids, 2019. **31**(9): p. 096105.

99.   Rayleigh, L., *On The Instability Of Jets*. Proceedings of the London Mathematical Society, 1878. **s1-10**(1): p. 4-13.

APPENDIX: ERROR AND CONVERGENCE ANALYSIS

In this appendix, an error and convergence analysis are performed for the EGFM based on the shock tube in problem *4.1.4*. The L1 error norm $(L_1 = \sum_{i=1}^{M} |f(x_i) - f_i|/M)$ is computed globally for the OGFM, RGFM and EGFM results. Tables A1, A2, and A3 summarize the convergence of the global L1 error norm and the corresponding orders of convergence based on the density, velocity, and pressure fields. Note that the same numerical methods were used for all of the simulations in tables A1-A3. As shown in the tables, the L1 error norm is consistently smaller for the EGFM, indicating the EGFM results in more accurate solutions locally (near interfaces) and globally. However, we observe the EGFM does not enhance the order of convergence, and all of the versions used are approximately first order (this behavior is also likely influenced/dominated by other aspects of the numerical discretization).

Table A1. The density L1 norm error and the order of convergence for different GFMs.

	OGFM		RGFM		EGFM	
dx	Error	Order	Error	Order	Error	Order
1/100	0.23378		0.14732		0.10440	
1/200	0.12939	0.85	0.10627	0.47	0.05761	0.86
1/400	0.07728	0.74	0.04114	1.37	0.02991	0.95
1/800	0.03181	1.28	0.02780	0.57	0.01574	0.93
1/1600	0.01492	1.09	0.01133	1.30	0.00864	0.87

Table A2. The velocity L1 norm error and the order of convergence for different GFMs.

	OGFM		RGFM		EGFM	
dx	Error	Order	Error	Order	Error	Order
1/100	0.24295		0.26763		0.20513	
1/200	0.13878	0.81	0.13739	0.96	0.10822	0.92
1/400	0.06865	1.02	0.07019	0.97	0.05522	0.97
1/800	0.03590	0.94	0.03600	0.96	0.02865	0.95
1/1600	0.01698	1.08	0.01898	0.92	0.01529	0.91

Table A3. The pressure L1 norm error and the order of convergence for different GFMs.

	OGFM		RGFM		EGFM	
dx	Error	Order	Error	Order	Error	Order
1/100	1.94546		1.82989		1.42746	
1/200	1.09953	0.82	0.94046	0.96	0.74962	0.93
1/400	0.54318	1.02	0.48031	0.97	0.38211	0.97
1/800	0.28247	0.94	0.24680	0.96	0.19909	0.94
1/1600	0.13403	1.08	0.13061	0.92	0.10665	0.90